Master's thesis

NTNU
Norwegian University of Science and Technology
Faculty of Natural Sciences
Department of Physics

Mathias Signebøen

High-energy-neutrino production in high-redshift blazars

Master's thesis in Physics
Supervisor: Prof. Foteini Oikonomou
May 2024

NTNU
Norwegian University of
Science and Technology

Mathias Signebøen

High-energy-neutrino production in high-redshift blazars

Master's thesis in Physics
Supervisor: Prof. Foteini Oikonomou
May 2024

Norwegian University of Science and Technology
Faculty of Natural Sciences
Department of Physics

NTNU
Norwegian University of
Science and Technology

Abstract

The discovery of an astrophysical neutrino flux by the IceCube Neutrino Observatory motivates the search for strong proton accelerators that can produce neutrinos through interactions between high-energy protons and photons. Blazars, being some of the most luminous sources of radiation in the Universe, could be the answer. Attempting to establish a connection between blazars and astrophysical neutrinos, this thesis makes a theoretical prediction of the neutrino fluxes of a selection of blazars. This is done by making leptohadronic models of the 19 blazars studied in Ghisellini et al. (G11). These blazars are among the most powerful in the Universe in terms of jet power and accretion disk luminosity, potentially making them strong neutrino emitters. The leptonic model is based on the leptonic model in G11 but with the addition of an injected proton spectrum. The proton spectrum luminosity is set at a level where its contribution to the energy flux is subdominant. Updated Fermi-LAT data are also considered when evaluating the quality of the model. The predicted neutrino flux is compared to the flux sensitivity of IceCube, along with the predicted future flux sensitivities of IceCube-Gen2 and KM3NeT/ARCA. It is found that out of the 19 blazars studied, the three named 4C+01.02, TXS 0322+222 and PKS 0458-02 produce neutrino fluxes that may be detectable within the first 15 years of IceCube-Gen2. For the model in this thesis, the neutrino fluxes peak at energies larger than 1 PeV.

Sammendrag

Oppdagelsen av en astrofysisk nøytrinofluks av IceCube Neutrino Observatory motiverer jakten på sterke protonakseleratorer som kan produsere nøytrinoer gjennom vekselvirkninger mellom høyenergiske protoner og fotoner. Blåsarer, i kraft av å være noen av universets mest lyssterke strålekilder, kan være svaret. I et forsøk på å finne en sammenheng mellom blåsarer og astrofysiske nøytrinoer, lager denne oppgaven en teoretisk prognose for nøytrinofluksene til et utvalg blåsarer. Dette gjøres ved å lage leptohadroniske modeller av de 19 blåsarene som ble analysert i Ghisellini et al. (G11). Disse blåsarene er blant de kraftigste i universet når det kommer til jetstrålenes effekt og tilvekstskivenes luminositet. Dette kan potensielt gjøre dem til kraftige nøytrinokilder. Den leptoniske modellen tar utgangspunkt i den leptoniske modellen til G11 men med tilføyelsen av et injisert protonspektrum. Protonspekterets luminositet bestemmes slik at protonenes bidrag til den totale energifluksen ikke påvirker samsvaret med dataene fra G11. Oppdatert data fra Fermi-LAT, tas i betraktning når modellens kvalitet vurderes. Nøytrinofluksens prognose sammenliknes med flukssensitiviteten til IceCube-observatoriet, samt de framtidige antatte flukssensitivitetene til IceCube-Gen2 og KM3NeT/ARCA.
En kommer fram til at av de 19 blåsarene analysert her, er det de tre ved navn 4C+01.02, TXS 0322+222 og PKS 0458-02 som produserer nøytrinoflukser som kan være sterke nok til å kunne oppfattes i løpet av IceCube-Gen2s første 15 år. For modellen i denne oppgaven når nøytrinofluksen toppen for energier høyere enn 1 PeV.

Acknowledgements

Firstly, I want to thank my supervisor, Professor Foteini Oikonomou, for suggesting the topic of the thesis. Learning more about Active Galactic Nuclei and working on multi-messenger modelling of blazars has been a rewarding experience. Her guidance and help throughout the work with this thesis, along with her extensive knowledge of the topic, has been invaluable.
I also want to thank PhD Candidate Egor Podlesnyi for his help with the leptohadronic computational packages used to complete this thesis. I am a novice in this area, so the help is much appreciated.
For his help with calculating the error for the 4FGL bands, I want to thank PhD Candidate Maksat Satybaldiev.
Additionally, I want to thank my comrades in Δp. My time with them has truly made my time at NTNU unforgettable. The memories and friends I made in Δp are things I hold dearly.
Furthermore, I want to thank my good friend Elías Örn Frímannsson, student of physics and astronomy at UiO. Our discussions have been a great motivation for me.
Moreover, I want to thank my family for their support and for nourishing my interest in astrophysics from a young age. I especially want to thank my grandfather, Roar Signebøen, who was very supportive of me studying at NTNU but sadly passed away before I could graduate.
Lastly, I want to thank my loving girlfriend May Helen Wold Bjerkeli for her patience and understanding. When working on large projects I have a tendency to neglect everything around me, so I greatly appreciate her being patient with me and tolerating this.

Contents

List of Figures

List of Tables

1 Introduction

Active Galactic Nuclei (AGN) are extremely bright central regions of galaxies that emit radiation across the whole electromagnetic spectrum, from radio to gamma-rays (e.g Padovani et al. 2017). The IceCube Neutrino Observatory has detected high-energy astrophysical neutrinos, but the source of them is still an open question (e.g. Ahlers and Halzen 2018; Troitsky 2021). AGN are a potential candidate given their ability to accelerate protons to relativistic energies. The connection between gamma-ray emitting AGN and high-energy astrophysical neutrinos has been explored by various authors (e.g. Nellen, Mannheim, and Biermann 1993; Mannheim 1993; Kelner and Aharonian 2008; Cerruti et al. 2015; Tavecchio and Ghisellini 2015; Resconi et al. 2017; Zech, Cerruti, and Mazin 2017; Cerruti et al. 2018; Gao et al. 2018; Keivani et al. 2018; Murase, Oikonomou, and Petropoulou 2018; Righi, Tavecchio, and Inoue 2018; Oikonomou et al. 2019; Zhang et al. 2020; Rodrigues et al. 2023).

This chapter consists of a brief history of AGN, a description of blazars and their properties, an overview of telescopes used to observe AGN, and finally a project description. Chapter 2 reviews theoretical background concepts relevant to the project. Chapter 3 outlines the model setup, choice of sources, and assumptions, and describes the software used for numerical simulations. Chapter 4 consists of a presentation of the results and a discussion. Chapter 5 is the conclusion.

1.1 History

The brightest AGN are quasars, short for "quasi-stellar radio source". Originally thought to be stars within our own Galaxy, Schmidt (1963) found that one of these light sources had an unexpectedly large redshift. They concluded that the most likely explanation was that the source of the redshift was the expansion of the Universe, implying that the source is extragalactic. This in turn meant that the luminosity of the object was very large. Indeed, AGN have luminosities comparable to entire galaxies (e.g. Ghisellini 2013). Such large luminosities require a mass of more than a million solar masses in a volume the size of our Solar System (Lynden-Bell 1969). Salpeter (1964) and Lynden-Bell (1969) showed that a black hole accreting matter can release enough energy to explain the quasar luminosities. Close to a black hole's event horizon, general relativistic effects are important. Einstein's field equations (Einstein 1915) were solved for a non-rotating spherical object in Schwarzschild (1916). However, conservation of angular momentum means that any physically realistic black hole that accretes matter must also rotate. The solution for a rotating object was found in Kerr (1963). Using the metric from Kerr (1963), Blandford and Znajek (1977) showed that the rotational energy of a black hole can be extracted through electromagnetic interactions between the black hole and the accreted matter.

1.2 Blazars

Urry and Padovani (1995) describe a unification scheme for AGN where the different categories of AGN are interpreted as the same type of object, but with different orientations

with respect to the observer. Doppler shifts cause the spectral energy distribution (SED) of the AGN to look different depending on the viewing angle and orientation, as shown in Figure 1.1. Blazars are characterised by a small angle between the bulk motion of particles in the jet and the viewing angle, causing the observed energy flux to be boosted with respect to the energy flux in the comoving frame of the jet. Since the observed energy flux of an object is inversely proportional to its distance squared, a Doppler boost of the energy flux enables one to detect objects that are further away, i.e. at higher redshifts.

A blazar consists of a supermassive black hole in the center, with masses between a million and several billion solar masses; an accretion disk; an X-ray corona close to the disk; a dust torus several parsecs from the black hole; a Broad-Line region, consisting of gas that re-emits a portion of the disk radiation in the form of emission lines broadened by Doppler shifts; a Narrow-line Region, similar to the Broad-Line Region but at a larger distance and with less broadening of the emission lines; and jets of relativistic matter, responsible for most of the emitted radiation (e.g. Ghisellini 2013). The SED of blazars are characterised by two humps, one in the low-energy radio range, and one in the high-energy gamma-ray range.

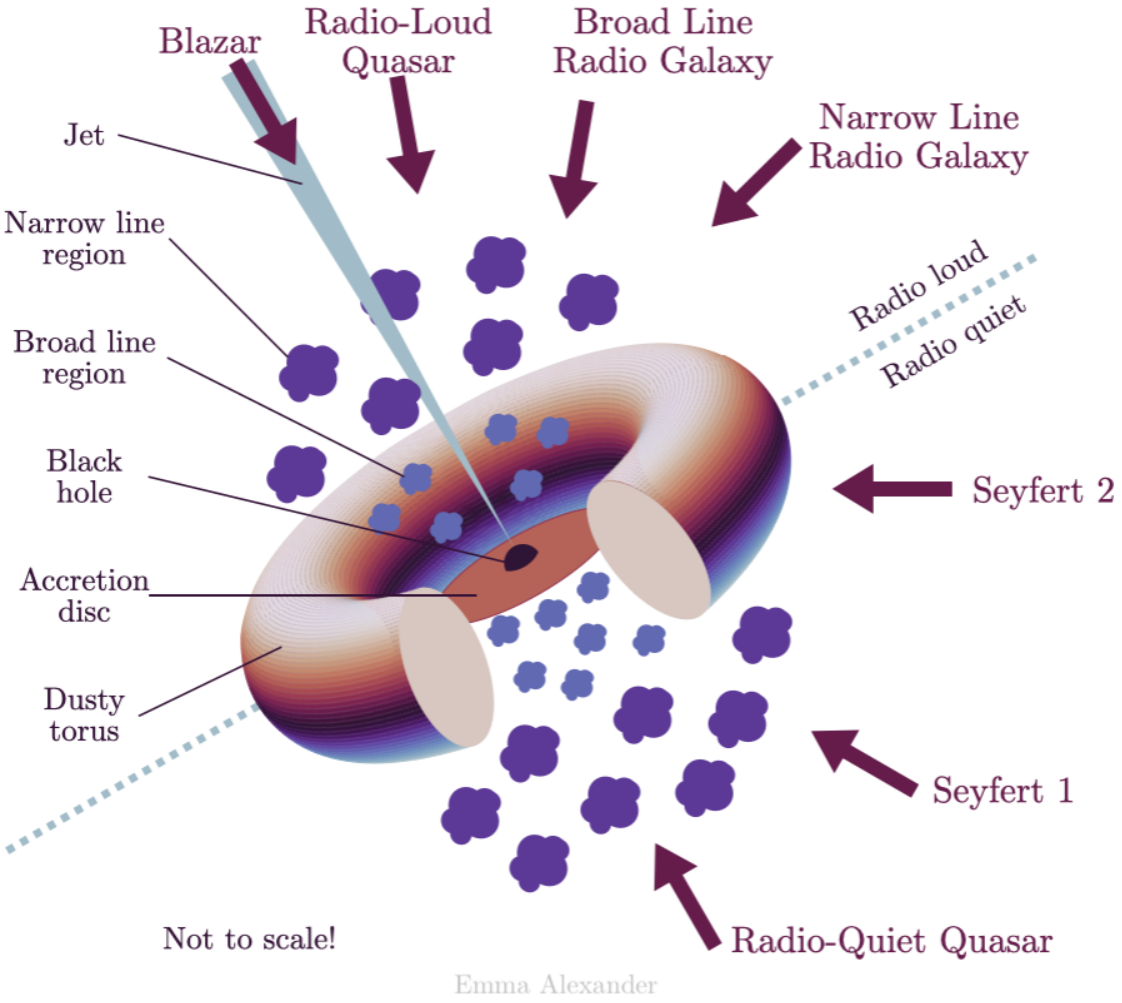

Figure 1.1: Unified model of AGN. Figure retrieved from `https://commons.wikimedia.org/wiki/File:Emmaalexander_unified_agn.png`. The figure is a schematic of a typical AGN. Different categories of AGN are interpreted as the same type of object but with different orientations with respect to the observer. This type of unified scheme for AGN is discussed in Urry and Padovani (1995).

1.3 Observing AGN

AGN emit radiation across the electromagnetic spectrum. Observing them thus requires telescopes that operate in different wavelength ranges. If AGN are also sources of high-energy neutrinos, then neutrino observatories are needed to detect this neutrino flux.

1.3.1 X-ray, UV and gamma-ray observations

The Fermi satellite's Large Area Telescope (LAT) has detected thousands of AGN since its launch in 2008 (Ajello et al. 2022). Fermi-LAT[1] observes light in the gamma-ray range. Being the only space-based gamma-ray observatory, it can detect and observe distant

[1] `https://fermi.gsfc.nasa.gov/science/instruments/table1-1.html`

gamma-ray sources, like blazars, without the interference of the atmosphere.
The Swift[2] satellite studies gamma-ray bursts (GRBs) through multi-wavelength observations. Its connection to GRBs makes it suitable for the study of sources with high gamma-ray fluxes, like blazars. It has the instruments UV/Optical Telescope(UVOT), which observes in the optical and UV range; X-ray Telescope (XRT), which observes in the soft X-rays; and the Burst Alert Telescope (BAT), which observes in the hard X-rays. Data from these telescopes put constraints on theoretical models of AGN.

1.3.2 IceCube Neutrino Observatory

Neutrinos have no electric charge and very low mass. As a result, neutrinos can traverse the Universe with no deflection from magnetic fields and very little absorption by intermediate matter, making them a valuable astronomical messenger (Ahlers and Halzen 2018). However, these properties make them very difficult to detect.

The IceCube Neutrino Observatory[3] consists of a cubic kilometer of ice filled with thousands of digital optical modules, see Figure 1.2. When high-energy neutrinos pass through the ice, a portion of them interact with nucleons in the ice and produce leptons through the charged current weak interaction (Ahlers and Halzen 2018). The speed of light in ice is slightly lower than in a vacuum. When the produced high-energy leptons move faster than the speed of light of in ice, they emit Cherenkov radiation. These Cherenkov photons are then observed by the digital optical modules. From these signals, the detector can determine the direction, energy and flavour of the neutrinos (see e.g. Ahlers and Halzen 2018). Secondary charged particles resulting from the neutral current weak interaction are detected in a similar way. Because of its location at the South Pole, IceCube has an asymmetry between the northern and southern hemispheres in its sensitivity to astrophysical neutrino fluxes. To supplement IceCube, the KM3NeT/ARCA detector is currently being built in the Mediterranean Sea (see e.g. Muller, Heijboer, and Eeden 2023).

[2] https://swift.gsfc.nasa.gov/about_swift/
[3] https://icecube.wisc.edu/about-us/facts/

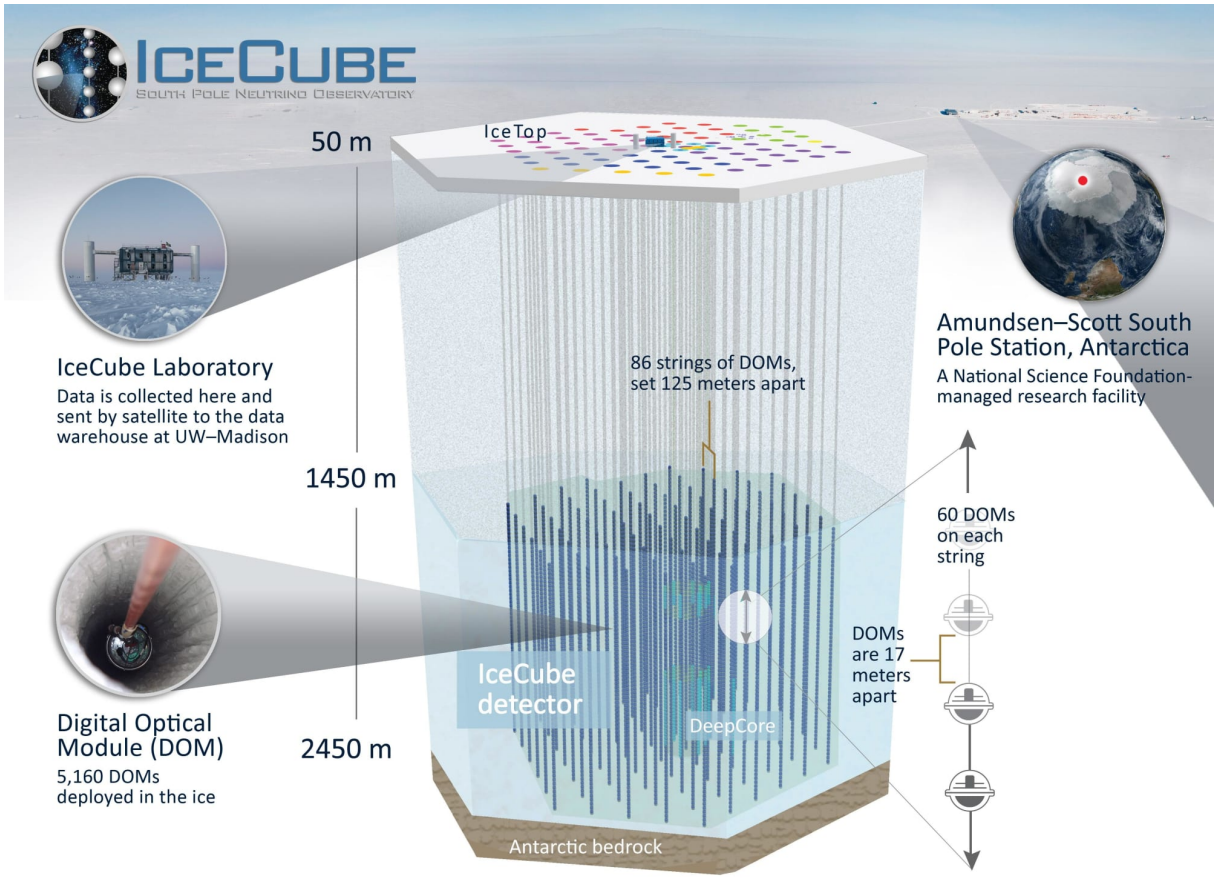

Figure 1.2: A schematic of the IceCube detector. Figure retrieved from `https://res.cloudinary.com/icecube/images/q_auto/v1653683283/gal_MnOrenewal_icecube_detector_9996b6adb/gal_MnOrenewal_icecube_detector_9996b6adb.jpg?_i=AA`.

1.4 Project description

The project in this thesis involves leptohadronic modelling of the high-redshift blazars in Ghisellini et al. (G11), in order to make theoretical predictions of the high-energy neutrino flux from these sources. The model in G11 is a purely leptonic one. However, the observation of high-energy astrophysical neutrinos by IceCube motivates the search for high-energy neutrino emitters. To explore if the blazars in G11 are possible candidates, a leptohadronic model is needed. This project does not involve any analysis of observational data. The data points are taken from the G11 paper, along with data from the HEASARC[4] archive. The results are summarized in plots of the spectral energy distributions (SEDs) of the modelled blazars.

[4] `https://heasarc.gsfc.nasa.gov/db-perl/W3Browse/w3table.pl?tablehead=name%3Dfermilac&Action=More+Options`

2 Theoretical background concepts

In this work, the radiation from the jet is assumed to be emitted primarily from a single radiation zone. The radiation zone is modelled as a spherical blob located at a distance $R_{\rm diss}$ from the black hole. Relativistic protons and electrons in the blob, with Lorentz factors γ_e and γ_b respectively, are also moving with a bulk velocity characterised by the Lorentz factor Γ. Special relativistic effects cause the emitted radiation to be blueshifted. The observed $\nu F(\nu)$ energy flux is therefore given by $\nu F(\nu) = \delta^4[\nu F(\nu)]'$, where $[\nu F(\nu)]'$ is the energy flux in the comoving frame of the blob and $\delta = [\Gamma(1 - \beta\cos\theta)]^{-1}$ is the Doppler factor. For blazars, the viewing angle θ is small, causing the Doppler factor δ to be large.
In this chapter, the main interactions between the particles in the blob and the magnetic field and different photon fields are described. This chapter draws heavily from Chapter 8 in Ghisellini (2013) and Chapters 6, 7 and 9 in Dermer and Menon (2009), along with Ghisellini and Tavecchio (2009).

2.1 Photon fields in Active Galactic Nuclei

The photon fields in AGN consist of radiation from the accretion disk, X-ray corona, broad-line region (BLR), and the dust torus. In this work, these photon fields are modelled as in Ghisellini and Tavecchio (2009). Due to special relativistic effects, photon fields moving towards the radiation zone are boosted proportional to Γ^2, while those moving away from the radiation zone are correspondingly deboosted. Thus, the contribution to the external photon field from the accretion disk and corona is negligible compared to the contribution from the BLR and the torus, provided $R_{\rm diss} > R_{\rm disk}$ where $R_{\rm disk}$ is the size of the accretion disk and $R_{\rm diss}$ is the distance from the black hole to the blob. The Schwarzschild radius for a black hole is given by

$$R_S = \frac{2GM}{c^2} = 2.95 \cdot 10^{14}\,\mathrm{cm}\left(\frac{M}{10^9 M_\odot}\right), \tag{2.1}$$

where M is the mass, G is Newton's gravitational constant, c is the speed of light and $M_\odot$ is the solar mass.

2.1.1 Accretion disk

The accretion disk consists of matter orbiting around the black hole. The radiated energy is generated by the accretion process, where infalling material has its gravitational potential energy converted to kinetic energy as it falls inward towards the black hole. In classical physics, the luminosity of this process is given by

$$L = \frac{d}{dt}E_g = \frac{d}{dt}\int_\infty^R \frac{-GMm}{r^2}dr = \frac{d}{dt}\frac{GMm}{R} = \frac{GM\dot{m}}{R}, \tag{2.2}$$

where M is the black hole mass and $\dot{m}$ is the accretion rate. As pointed out in e.g. Armitage (2022), a fraction of this energy will cross over the event horizon. Thus, the luminosity can be described by $L = \eta\dot{m}c^2$, where η is the radiative efficiency. The variable η depends on the accretion mode, which itself depends on the angular momentum of

the black hole. The accretion mode is described by the dimensionless spin parameter $0 \leq a < 1$, which is defined as $a = cJ/GM^2$, where M is the mass and J is the angular momentum (Armitage 2022). It can be shown that $\eta(a = 0) = 5.7\%$ and $\eta(a \to 1) = 42\%$ (Armitage 2022). The luminosity is limited by the Eddington luminosity

$$L_{Edd} = \frac{4\pi cGM}{\kappa}, \tag{2.3}$$

where κ is the opacity of the gas in the accretion disk. For Thomson scattering of hydrogen gas, the opacity is given by $\kappa = \sigma_T/m_H$, where σ_T is the Thomson scattering cross-section and m_H is the mass of the hydrogen atom. The corresponding Eddington luminosity is given by

$$L_{Edd} \approx 1.26 \cdot 10^{38} (M/M_\odot)\,\mathrm{erg\,s^{-1}} \tag{2.4}$$

The matter in the accretion disk orbits the black hole at different radii. Equation 2.2 then suggests that the radiated energy is a function of radial distance from the black hole. Indeed, this is what is shown in Shakura and Sunyaev (1976). Equation (3.3) in their article states that the energy emission is $\propto [1 - (R_0/R)^{1/2}]$ (Shakura and Sunyaev 1976), where R_0 is the innermost radius of the disk. Ghisellini (2013) models the disk spectrum as a collection of thin rings all emitting black-body radiation, with the temperature profile given by

$$T = \left[\frac{3R_\mathrm{S}L_\mathrm{disk}}{16\pi\eta\sigma_\mathrm{MB}R^3}\right]^{1/4}\left[1 - \left(\frac{3R_\mathrm{S}}{R}\right)^{1/2}\right]^{1/4}, \tag{2.5}$$

where R_S is the Schwarzschild radius, σ_MB is the Maxwell-Boltzmann constant, and η is the radiative efficiency.

2.1.2 X-ray corona

The corona's nature is unclear, but it is likely reflected accretion disk radiation. Observations of the X-ray spectrum of AGN show a power law flux in the range $0.1 - 200\,\mathrm{keV}$ with an exponential cutoff (Ghisellini 2013)

$$F_X(\nu) \propto \nu^{-\alpha_X} e^{-\nu/\nu_c}, \tag{2.6}$$

where $\alpha_X \sim 0.7 - 0.9$ and $h\nu_c \in [40, 300]\,\mathrm{keV}$ are typical values. Consequently the spectrum from the corona looks flat in a $\nu F(\nu)$ plot until it falls exponentially for energies $\sim 100\,\mathrm{keV}$.

One expects the corona to be close to the black hole because of the high variability of the X-ray flux, and because its luminosity is comparable to the disk luminosity. According to Equation 2.2, the gravitational energy released is proportional to R^{-1}. Therefore, if the corona draws its power from gravitational potential energy, it must be close to the black hole.

2.1.3 Broad-line region and narrow-line region

The emission line regions surrounding AGN can be put into two categories, the broad-line region (BLR) and the narrow-line region (NLR). The Lyman α line and the [OIII] line in Figure 2.1 are examples of broad-line and narrow-lines respectively. We do not know what the emission regions are. However, the presence of the different emission lines allows

one to identify the material composition of the region. Furthermore, the broadening of the broad emission lines is too large to be due to thermal broadening, so there must be some bulk motion of the material in the BLR. The broad-lines have full width at half maximum (FWHM) $\Delta\lambda \sim (10^{-2} - 10^{-1})\lambda_0$, while the narrow-lines have FWHM $\Delta\lambda \sim 10^{-3}\lambda_0$ (Ghisellini 2013). The FWHM of an emission line is found by measuring its width where the intensity is half the value of the intensity at the peak. The velocity corresponding to this Doppler shift is then given by $v/c = \Delta\lambda/\lambda_0$. The BLR is located at a distance

$$R_{BLR} = 10^{17}\,\mathrm{cm}\left(\frac{L_d}{10^{45}\,\mathrm{erg\,s^{-1}}}\right)^{1/2}, \tag{2.7}$$

where L_d is the disk luminosity. The NLR, however, is at a distance of around 100 pc. Using a similar expression for the comoving energy density from NLR photons as in Equation 2.13 and comparing with the contribution from the BLR photons, one finds

$$\frac{U'_{\mathrm{NLR}}}{U'_{\mathrm{BLR}}} \sim \left(\frac{R_{\mathrm{BLR}}}{100\,\mathrm{pc}}\right)^2 \sim 10^{-7}\left(\frac{L_d}{10^{45}\,\mathrm{erg\,s^{-1}}}\right), \tag{2.8}$$

where primed quantities denote the comoving frame of the blob. Hence, the NLR photons' contribution to the energy density in the blazar blob is negligible compared to that of the BLR, provided that R_{diss} is not much larger than R_{BLR}.

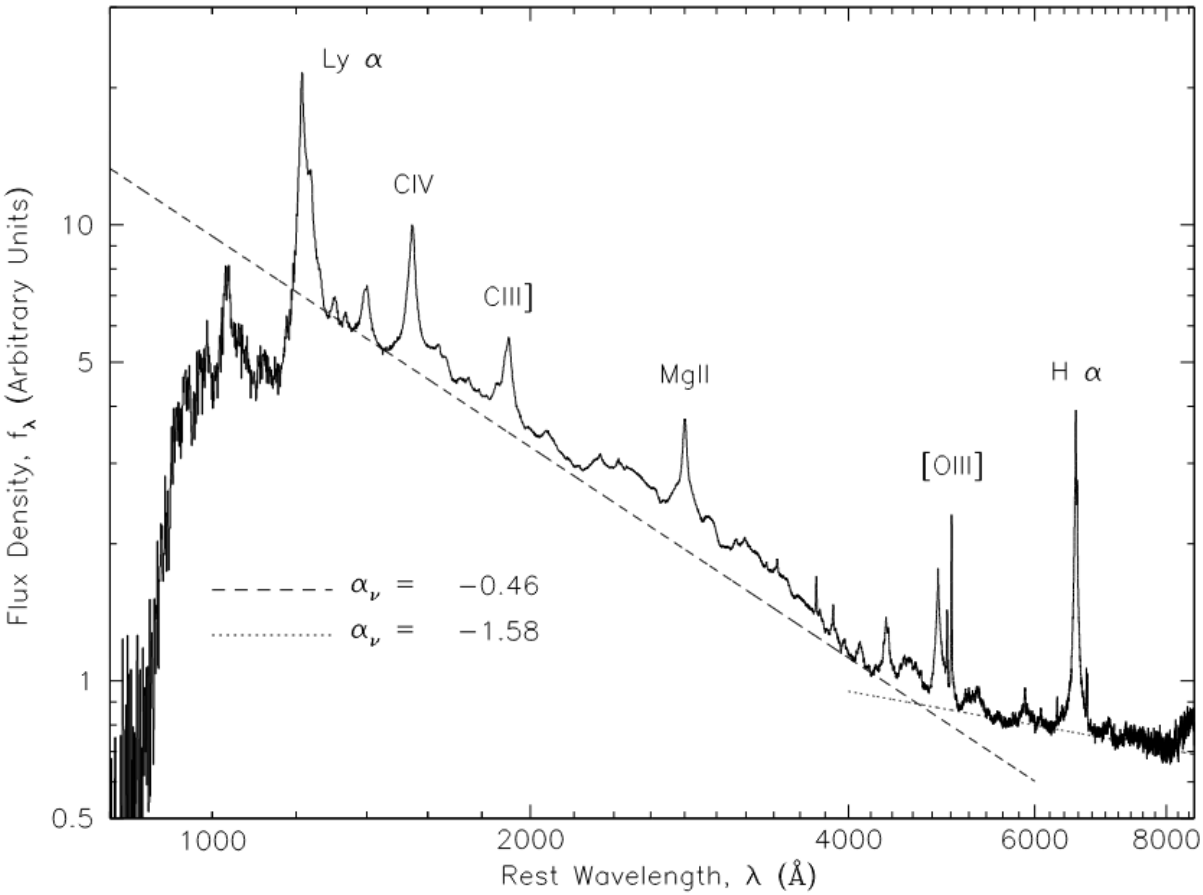

Figure 2.1: Composite quasar spectrum from the Sloan Digital Sky Survey. Figure retrieved from Vanden Berk et al. (2001). Several prominent emission lines can be seen, including the broad Lyman α line.

2.1.4 Dust torus

Some of the light from the accretion disk is absorbed by a dust torus surrounding the black hole, and re-emitted in the infrared. The torus is located at a distance

$$R_{\rm IR} = 2.5 \cdot 10^{18}\,{\rm cm}\,\left(\frac{L_d}{10^{45}\,{\rm erg\,s^{-1}}}\right)^{1/2}, \tag{2.9}$$

where L_d is the disk luminosity. The torus model used in this work is the same as in G11. This model is an approximation. It has been suggested, e.g. by Burtscher et al. (2013), that the relationship between $R_{\rm IR}$ and L_d in reality is more complex than in Equation 2.9. The energy density of the torus photons is given by

$$U'_{\rm IR} \sim \frac{f_{\rm IR} L_{\rm d} \Gamma^2}{4\pi R_{\rm IR}^2 c}, \tag{2.10}$$

where $f_{\rm IR}$ is the torus covering factor and $R_{\rm IR}$ is the torus radius. Comparing $U'_{\rm BLR}$, given by Equation 2.13, with $U'_{\rm IR}$, given by Equation 2.10, and inserting Equations 2.7 and 2.9, one finds that

$$\frac{U'_{\rm IR}}{U'_{\rm BLR}} \sim \frac{f_{\rm IR}}{f_{\rm BLR}} \left(\frac{R_{\rm BLR}}{R_{\rm IR}}\right)^2 \sim 10^{-2}. \tag{2.11}$$

Consequently, the contribution to the comoving external photon energy density is dominated by the BLR photons, while the torus photons are subdominant, provided that $R_{\rm diss} < R_{\rm BLR}$.

2.1.5 CMB photons

For the sources in this sample, the contribution to the external photon field from the Cosmic Microwave Background (CMB) is negligible in the radiation zone. Following Ghisellini and Tavecchio (2009),

$$U'_{\rm CMB} = a T_0^4 \Gamma^2 (1+z)^4; \tag{2.12}$$

where $a = 7.65 \times 10^{-15}\,{\rm erg\,cm^{-3}\,K^{-4}}$ is the radiation constant $4\sigma/c$, where σ is the Stefan-Boltzmann constant; and $T_0 = 2.7\,{\rm K}$ is the CMB temperature at $z = 0$. Meanwhile, the energy density of the BLR photons is given by (Ghisellini and Tavecchio 2009)

$$U'_{\rm BLR} \sim \frac{17\Gamma^2}{12} \frac{f_{\rm BLR} L_{\rm d}}{4\pi R_{\rm BLR}^2 c}, \tag{2.13}$$

where $f_{\rm BLR}$ is the BLR covering factor and $L_{\rm d}$ is the accretion disk luminosity. Comparing the two, one finds that

$$\frac{U'_{\rm CMB}}{U'_{\rm BLR}} \sim \frac{12 a T_0^4 \Gamma^2 (1+z)^4 \cdot 4\pi R_{\rm BLR}^2 c}{17\Gamma^2 f_{\rm BLR} L_{\rm d}} \tag{2.14}$$

$$\Rightarrow \frac{U'_{\rm CMB}}{U'_{\rm BLR}} \sim 10^{-9} \cdot \left(\frac{1+z}{3}\right)^4 \left(\frac{R_{\rm BLR}}{10^{17}\,{\rm cm}}\right)^2 \left(\frac{0.1}{f_{\rm BLR}}\right) \left(\frac{10^{45}\,{\rm erg\,s^{-1}}}{L_{\rm d}}\right). \tag{2.15}$$

Thus, one can conclude that the contribution from the CMB to the energy density in the jet is negligible.

2.1.6 Extragalactic Background Light

The Extragalactic Background Light (EBL) is the light from all galaxies in the Universe. This provides a background photon density that can interact with the gamma-ray emissions of AGN to create electron-positron pairs through gamma-gamma pair production. This process is described in Section 2.4.2. Interactions with the EBL effectively absorb TeV photons from AGN, hindering observations significantly (Cerruti 2020). Naturally, the absorption effect increases with distance. For high-redshift blazars, it is thus expected to be significant. The attenuation of gamma-ray spectra of high-redshift blazars has been modelled by e.g. Gilmore et al. (2009). They showed that the effects of this absorption are negligible for gamma-rays below 10 GeV. Figures 6 and 7 in their paper do show that absorption becomes significant above 10 GeV, with the opacity reaching $\tau \approx 1$ around 20 GeV for redshifts $z \geq 2$.

2.2 Leptonic processes

The main contribution to the SEDs of the blazars in the sample is expected to come from leptonic processes. The leptons are primarily electrons accelerated to energies in the MeV to GeV range, along with electron-positron pairs produced by $\gamma\gamma$ interactions. The leptonic processes considered here are synchrotron radiation resulting from the interaction between the leptons in the jet and the magnetic field, and the inverse-Compton scattering of the leptons off of the external photon field.

2.2.1 Synchrotron radiation

When relativistic charged particles are accelerated by a magnetic field, they emit synchrotron radiation. Synchrotron radiation from relativistic leptons in the jet is believed to be the cause of the low-frequency hump in the blazar SED. In Chapter 7.2 of Dermer and Menon (2009), they show that the peak observed synchrotron frequency from an electron is

$$\nu_s \cong \frac{eB}{2\pi m_e c}\gamma^2 = 2.79 \times 10^{10}\,\mathrm{Hz}\left(\frac{B}{1\,\mathrm{G}}\right)\left(\frac{\gamma}{10^2}\right)^2 \tag{2.16}$$

$$\Rightarrow \nu_s' = 1.86 \cdot 10^{11}\,\mathrm{Hz}\left(\frac{B}{1\,\mathrm{G}}\right)\left(\frac{\gamma}{10^2}\right)^2\left(\frac{\delta}{20}\right)\left(\frac{3}{z+1}\right). \tag{2.17}$$

For the sources in this sample, the magnetic field strengths are $\sim 1\,\mathrm{G}$, while the electron spectra have break energies $\gamma \sim 10^2$ and maximum energies $\gamma \sim 10^3$. This corresponds to strong observed synchrotron radiation in the frequencies $\nu \in [10^{11}, 10^{13}]\,\mathrm{Hz}$. This again corresponds to photon energies, given by $h\nu$, in the range $[10^{-4}, 10^{-2}]\,\mathrm{eV}$.

We can estimate the cooling timescale of the synchrotron process by $t_{\mathrm{cool}} = |E/\dot{E}|$. The energy loss rate for a charged particle in a magnetic field averaged over the pitch angles is given by (Dermer and Menon 2009, p. 120)

$$-\left(\frac{dE}{dt}\right)_{\mathrm{syn}} = \frac{4}{9}\left(\frac{Q^2}{mc^2}\right)^2 cB^2\beta^2\gamma^2, \tag{2.18}$$

where Q is the electric charge, B is the magnetic field strength, m is the particle mass, γ is the Lorentz factor of the particle and $\beta = v/c$ is its dimensionless speed. Since

$E \propto m$ and $\dot{E} \propto m^{-2}$, one sees that $t_{\rm cool} \propto m^3$. One can estimate the escape time of the particles $t_{\rm esc}$ by the light crossing time $t_{\rm cross} = R_{\rm blob}/c$. By comparing $t_{\rm cross}$ to $t_{\rm cool}$, one can determine if the synchrotron process contributes significantly to cooling the particle spectrum. For the electron, we can estimate $t_{\rm cool}$ by

$$t_{\rm syn} = \frac{\gamma m_e c^2}{|\dot{E}|} = \frac{9}{4}\frac{m_e c}{B^2\beta^2\gamma}\left(\frac{m_e c^2}{e^2}\right)^2 \simeq \frac{24.6}{\gamma}\,{\rm yr}\left(\frac{1}{\beta}\right)^2\left(\frac{1\,{\rm G}}{B}\right)^2. \tag{2.19}$$

Comparing this with the light crossing time

$$t_{\rm cross} = \frac{R_{\rm blob}}{c} \simeq 3.34\cdot 10^5\,{\rm s}\left(\frac{R_{\rm blob}}{10^{16}\,{\rm cm}}\right), \tag{2.20}$$

one sees that $t_{\rm syn} < t_{\rm cross}$ when $\gamma \sim 300$,

$$\frac{t_{\rm syn}}{t_{\rm cross}} = \frac{9}{4}\frac{m_e c^2}{B^2\beta^2\gamma R_{\rm blob}}\left(\frac{m_e c^2}{e^2}\right)^2 \simeq 0.696\left(\frac{300}{\gamma}\right)\left(\frac{\cdot 10^{16}\,{\rm cm}}{R_{\rm blob}}\right)\left(\frac{1}{\beta}\right)^2\left(\frac{1\,{\rm G}}{B}\right)^2. \tag{2.21}$$

Therefore, the electrons are expected to undergo synchrotron cooling within one light crossing time.

Synchrotron self-absorption

A portion of the emitted synchrotron photons are re-absorbed by the electrons in a process called synchrotron self-absorption (SSA). The synchrotron radiation flux is inversely proportional to the synchrotron self-absorption coefficient $\kappa_\nu^{\rm SSA}$. Following the derivation in Section 7.8 in Dermer and Menon (2009), it can be shown that $\kappa_\nu^{\rm SSA} \propto \nu^{-2}$. This implies that the SSA process causes the lower energy part of the synchrotron spectrum to be suppressed.
The absorption coefficient $\kappa_\nu^{\rm SSA}$ also depends on the shape of the electron spectrum, along with the Einstein coefficients. The latter have to be calculated using the quantum theory of radiation, which is beyond the scope of this chapter. The quantum theory of radiation describes the absorption and emission of a photon by an electron as an interaction between two quantum systems. See Chapter 16 in Hemmer (2005) for details.

2.2.2 Inverse-Compton scattering

Compton scattering is the process in which a charged particle scatters off of a photon. When these particles are in motion and have a higher energy than the photon, they can transfer some of their energy to the photon. This process is called inverse-Compton scattering (IC) and is the main source of gamma-ray photons in leptonic blazar models.

Following Chapter 6 in Dermer and Menon (2009), we consider the Compton scattering of a photon in the electron rest frame. The scattered photon, with dimensionless energy $\epsilon_s = h\nu_s/m_e c^2$; will make an angle χ with the direction of the incident photon, with energy $\epsilon = h\nu/m_e c^2$. After the scattering, the electron will move with a Lorentz factor γ_e, and the angle between its trajectory and that of the incident photon will be θ_e. Energy conservation requires that $1 + \epsilon = \epsilon_s + \gamma_e$, while momentum conservation requires that

$\epsilon = \epsilon_s \cos\chi + \beta_e\gamma_e \cos\theta_e$ and $\epsilon_s \sin\chi = \beta_e\gamma_e \sin\theta_e$ in the x and y directions respectively. From here, it can be shown that

$$\epsilon_s = \frac{\epsilon}{1 + \epsilon(1 - \cos\chi)}. \tag{2.22}$$

Then one can transform this expression to the blob rest frame, and thereby get an angle dependent expression for the energy gained by the scattered photon per collision.

The total Compton scattering cross-section σ is calculated in Chapter 11 of Jauch and Rohrlich (1976) and is given by

$$\sigma(\epsilon) = 2\pi r_0^2 \left[\frac{1+\epsilon}{\epsilon^3} \left(\frac{2\epsilon(1+\epsilon)}{1+2\epsilon} - \ln(1+2\epsilon) \right) + \frac{\ln(1+2\epsilon)}{2\epsilon} - \frac{1+3\epsilon}{(1+2\epsilon)^2} \right], \tag{2.23}$$

where $r_0 = e^2/m_e c^2$ is the classical electron radius. The asymptotes are given by (Dermer and Menon 2009, p. 73)

$$\sigma(\epsilon) \to \begin{cases} \frac{8\pi r_0^2}{3} \left[1 - 2\epsilon + \frac{26}{5}\epsilon^2 + O(\epsilon^3)\right] & \text{for } \epsilon \ll 1, \\ \frac{\pi r_0^2}{\epsilon} \left[\ln(2\epsilon) + 1/2 + O(\epsilon^{-1})\right] & \text{for } \epsilon \gg 1, \end{cases} \tag{2.24}$$

where $\epsilon \ll 1$ and $\epsilon \gg 1$ define the Thomson and Klein-Nishina scattering regimes respectively. Since

$$\lim_{\epsilon\to\infty} \sigma(\epsilon) \propto \lim_{\epsilon\to\infty} \frac{\ln(2\epsilon)}{\epsilon} = \lim_{\epsilon\to\infty} \frac{1}{\epsilon} = 0,$$

one expects the highest energy Compton scatterings to be suppressed. This is expressed through a suppression at the higher end of the gamma-ray spectrum in the blazar SED.

For Thomson scattering of relativistic charged particles on an isotropic photon field, the energy loss rate is given by (Dermer and Menon 2009, p. 82)

$$-\left(\frac{dE}{dt}\right)_T = mc^2 \left(\frac{m_e}{m}\right)^3 Z^2 \frac{4}{3} c\sigma_T u_T \gamma^2, \tag{2.25}$$

for a particle with mass m and charge Ze, with Lorentz factor γ. Here, $\sigma_T = 8\pi r_0^2/3$ is the Thomson cross-section, while $u_T = \int_0^{1/\gamma} d\epsilon\, \epsilon n_{\rm ph}(\epsilon)$ is the energy density of the target photons. The upper limit $1/\gamma$ ensures that $\epsilon \ll 1$, since we are dealing with relativistic particles with $\gamma \gg 1$. Similar to the synchrotron process, $\dot{E} \propto m^{-2}$, and one can conclude that electron IC dominates the blazar spectrum while proton IC is subdominant.

External Compton scattering

The energy released in the inverse-Compton process depends on the energy density of the source photons. In Tavecchio and Ghisellini (2008), the observed photon frequency from Thomson scattering of a monochromatic photon field is estimated to be

$$\nu_C \simeq (3/4)\delta\nu_0'\gamma^2. \tag{2.26}$$

One can approximate the BLR photon field as monochromatic with frequency ν_0 in the observing frame. In Figure 2.1, it can be seen that the most prominent emission line is the Lyman α line. Thus one can use $\nu_0 = 2.5 \cdot 10^{15}$ Hz as the frequency of the monochromatic

BLR field as an approximation. The blob comoving frequency is given by $\nu_0' \simeq 2\Gamma\nu_0$ (Tavecchio and Ghisellini 2008), such that the full expression for ν_C becomes

$$\nu_C \simeq \frac{3\delta\Gamma}{8}\nu_0\gamma^2 = 1.13 \cdot 10^{21}\,\mathrm{Hz}\left(\frac{\delta}{20}\right)\left(\frac{\Gamma}{15}\right)\left(\frac{\nu_0}{10^{15}\,\mathrm{Hz}}\right)\left(\frac{\gamma}{10^2}\right)^2. \tag{2.27}$$

Following the same argument as in Section 2.2.1, one expects external Compton (EC) radiation in the range $\nu \in [10^{21}, 10^{23}]$ Hz, corresponding to photon energies $h\nu \in [10^6, 10^8]$ eV. Thus, this process can explain the observed gamma-ray peak in the blazar SED.

Synchrotron self-Compton

For the synchrotron self-Compton (SSC) process, the seed photons are the synchrotron photons discussed in Section 2.2.1. For a broken power law distribution of electrons, electrons at the break energy $\gamma_b m_e c^2$ emit the dominant synchrotron power. In Tavecchio, Maraschi, and Ghisellini (1998), the synchrotron frequency averaged over the spectral shape for an electron with break energy is reported to be

$$\nu_s = 3.7 \cdot 10^6\,\mathrm{Hz}\,\gamma_b^2\left(\frac{B}{1\,\mathrm{G}}\right)\frac{\delta}{1+z}. \tag{2.28}$$

Inserting γ_b and $\nu_s = \delta\nu_s'$ from Equation 2.28 into Equation 2.26, one finds

$$\nu_{SSC} = 3.7 \cdot 10^6\,\mathrm{Hz}\,\frac{3}{4}\left(\frac{B}{1\,\mathrm{G}}\right)\frac{\delta}{1+z}\gamma_b^4 \simeq 1.5 \cdot 10^{17}\,\mathrm{Hz}\left(\frac{B}{1\,\mathrm{G}}\right)\left(\frac{\gamma_b}{300}\right)^4\left(\frac{\delta}{20}\right)\left(\frac{3}{1+z}\right). \tag{2.29}$$

This corresponds to an energy $h\nu_{SSC} \sim 0.1\,\mathrm{keV}$. Thus one can expect the SSC process to produce X-ray photons in our model.

2.3 Photohadronic processes

Hadronic processes, in particular the photopion process, are responsible for neutrino production in blazars.
The protons produce radiation through the synchrotron and IC processes described in Section 2.2, although their contribution to the overall blazar SED is subdominant. More relevant is the production of electron-positron pairs through the Bethe-Heitler process, along with the secondary leptons from the photopion process; since radiation from leptons contributes significantly to the blazar SED.

Proton-proton interactions are also a potential source of high-energy neutrinos. However, in Cerruti (2020) it is stated that the contribution from proton-proton interactions in blazar jets is usually subdominant. There is not much gas in the jet of an AGN that can act as seed protons for the interaction. Gas clouds in the vicinity of AGN are usually found in the equatorial plane of the disk, which is perpendicular to and outside the jet. Consequently, proton-proton interactions are neglected in the following model.

2.3.1 Bethe-Heitler pair production

Bethe-Heitler pair production is the process (Cerruti 2020)

$$p + \gamma \to p + e^- + e^+, \tag{2.30}$$

in which relativistic protons scatter off of photons in the jet. According to Petropoulou and Mastichiadis (2014), the threshold energy for Bethe-Heitler pair production on synchrotron photons with frequency ν_s is

$$\gamma_{p,\phi e}^{(\mathrm{th})} \simeq 8.0 \cdot 10^4 \left(\frac{3}{1+z}\right)\left(\frac{\delta}{20}\right)\left(\frac{10^{16}\,\mathrm{Hz}}{\nu_s}\right). \tag{2.31}$$

For reactions near the threshold energy, the inelasticity of this process is (Dermer and Menon 2009, p. 203)

$$K_{\phi e} \simeq \frac{m_e}{m_p}. \tag{2.32}$$

The produced pairs have an average energy $\gamma_e m_e c^2$. Equation 2.32 then implies that

$$2\gamma_e m_e c^2 = K_{\phi e}\gamma_{p,\phi e}^{(\mathrm{th})} m_p c^2 \simeq \frac{m_e}{m_p}\gamma_{p,\phi e}^{(\mathrm{th})} m_p c^2 \Rightarrow \gamma_e \simeq \frac{\gamma_{p,\phi e}^{(\mathrm{th})}}{2} \tag{2.33}$$

$$\Rightarrow \gamma_e \simeq 4.0 \cdot 10^4 \left(\frac{3}{1+z}\right)\left(\frac{\delta}{20}\right)\left(\frac{10^{16}\,\mathrm{Hz}}{\nu_s}\right). \tag{2.34}$$

These secondary electrons and positrons produce radiation as described in Section 2.2. Since the Bethe-Heitler process is capable of producing leptons with higher energy than the primary electrons, these pairs can produce radiation at higher energies than the primary electrons. As explained in Section 2.2.2, radiation from inverse-Compton scattering is suppressed in the Klein-Nishina regime. However, since the synchrotron process does not suffer from this suppression, these secondary leptons can produce synchrotron radiation beyond the GeV range if they have sufficiently large Lorentz factors.

2.3.2 Photopion production

Photopion production is the process in which interactions between photons and protons produce neutral and charged pions (Cerruti 2020),

$$p + \gamma \to p + \pi^0 \tag{2.35}$$

$$p + \gamma \to n + \pi^+ \tag{2.36}$$

$$p + \gamma \to p + \pi^+ + \pi^-. \tag{2.37}$$

Atoyan and Dermer (2003) approximate the photopion cross-section as a sum of the single-pion production channel, given by Equations 2.35 and 2.36; and the multi-pion production channel, given by Equation 2.37. The single-pion production channel is itself a sum of the Δ^+ resonance channel and the direct production channel (Dermer and Menon 2009, p. 193). The threshold photon energy for the photopion process in the rest frame of the proton is $E_{\mathrm{th}} \simeq 150\,\mathrm{MeV}$, and the multipion channel starts to dominate for energies $> 500\,\mathrm{MeV}$ (Atoyan and Dermer 2003). This behaviour can also be observed in Figure 2.2. One can then approximate the cross-section as a step function where (Dermer and Menon 2009, p. 193)

$$\sigma_{\phi\pi}(E) = \begin{cases} 340\,\mu\mathrm{b}, & E_{\mathrm{th}} = 150\,\mathrm{MeV} \le E \le 500\,\mathrm{MeV}, \\ 120\,\mu\mathrm{b}, & E > 500\,\mathrm{MeV}, \end{cases} \tag{2.38}$$

with inelasticity (Dermer and Menon 2009, p. 193)

$$K_{\phi\pi}(E) = \begin{cases} 0.2, & 150\,\mathrm{MeV} \leq E \leq 500\,\mathrm{MeV}, \\ 0.6, & E > 500\,\mathrm{MeV}. \end{cases} \tag{2.39}$$

It can be shown that (Dermer and Menon 2009, p. 203)

$$\frac{K_{\phi\pi}\sigma_{\phi\pi}}{K_{\phi e}\sigma_{\phi e}} \approx 100, \tag{2.40}$$

suggesting that the photopion contribution to proton cooling dominates the contribution from Bethe-Heitler pair production. However, the high threshold energy for the photopion process means that it only dominates for the highest energy protons.

The produced pions are unstable and decay to photons, leptons, and neutrinos (Cerruti 2020);

$$\pi^0 \to 2\gamma \tag{2.41}$$
$$\pi^+ \to \mu^+ + \nu_\mu \to e^+ + \nu_e + \bar{\nu}_\mu + \nu_\mu \tag{2.42}$$
$$\pi^- \to \mu^- + \bar{\nu}_\mu \to e^- + \bar{\nu}_e + \nu_\mu + \bar{\nu}_\mu. \tag{2.43}$$

For the single-pion channel, branching ratios of 2.35 and 2.36 are approximately equal (Dermer and Menon 2009, p. 193). Combined with Equations 2.41 and 2.42, one sees that for every 2 gamma-rays, 3 neutrinos are produced. Furthermore, these gamma-rays carry on average 1/2 of the energy of the parent pion, while the neutrinos carry on average 1/4 (Ahlers and Halzen 2018). From here, Ahlers and Halzen (2018) show that for the single-pion channel, the production rate of pionic gamma-rays and the production rate of neutrinos are related by

$$\frac{1}{3}\sum_\alpha E_\nu^2 Q_{\nu_\alpha}(E_\nu) \simeq \frac{1}{4}[E_\gamma^2 Q_\gamma(E_\gamma)]_{E_\gamma = 2E_\nu}, \tag{2.44}$$

where the sum over α is the sum over the neutrino flavours. For the multipion channel, one assumes that the branching ratios are equal for the π^0, π^+ and π^- (Dermer and Menon 2009, p. 193). It also follows from the above that on average for the single-pion channel, $0.2 \cdot 1/4 = 0.05$ of the proton energy is transfered to the neutrinos; while for the multipion channel, $0.6 \cdot 1/4 = 0.15$ is transfered. From this, it follows that the lowest energy neutrinos produced in this process have an energy $\approx 47\,\mathrm{MeV}$ in the proton rest frame.
Similar to the Bethe-Heitler pairs, the secondary leptons from the photopion process also emit radiation as described in Section 2.2.

2.4 Relativistic particles in AGN jets

The relativistic particles in the jet consist of two main populations, the protons and the electrons. Primary electrons and protons are injected into the blob as described below. The hadronic processes described in Section 2.3, along with the gamma-gamma pair production described below, produce secondary leptons.

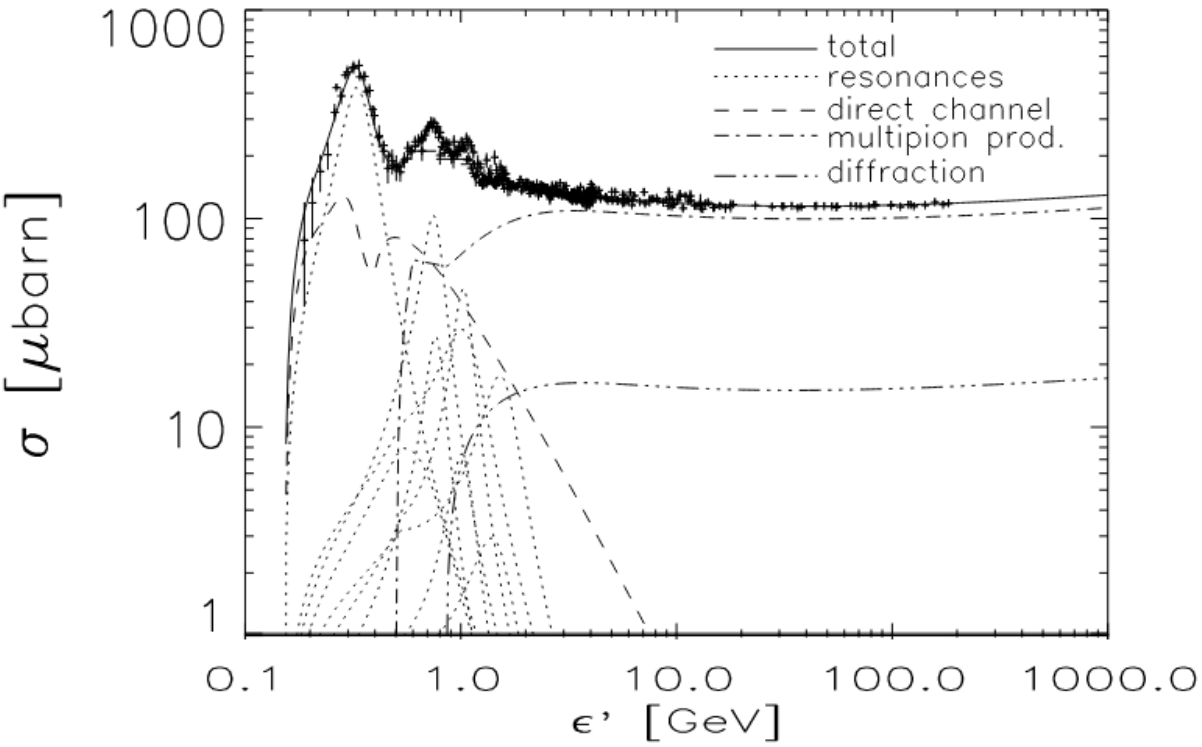

Figure 2.2: Total photopion cross-section as a function of photon energy in the rest frame of the proton. Figure retrieved from Mucke et al. (2000). One sees that the direct production and resonance channels dominate the cross-section for lower energies, while the multipion channel sets in around 0.5 GeV.

2.4.1 Proton spectrum

The proton spectrum follows a simple E^{-2} power law with an exponential cutoff. This spectral shape is derived for nonrelativistic shock acceleration in chapter 13 of Dermer and Menon (2009). The cutoff energy is chosen to be the energy at which the acceleration timescale equals the escape time. The proton acceleration timescale is given by

$$t_{\mathrm{acc}} = \eta \frac{E_p}{ceB}, \tag{2.45}$$

where $\eta \geq 1$ is a parametrisation of the acceleration efficiency. If one sets the escape time equal to the crossing time given by Equation 2.20, and sets this equal to t_{acc}, then the maximum proton energy is given by

$$\gamma_{p,\mathrm{max}} = \frac{E_p}{m_p c^2} = 3.19 \cdot 10^9 \left(\frac{1}{\eta}\right) \left(\frac{B}{1\,\mathrm{G}}\right) \left(\frac{R_{\mathrm{blob}}}{10^{16}\,\mathrm{cm}}\right). \tag{2.46}$$

The proton spectrum luminosity determines the strength of the neutrino flux. However, the introduction of protons also results in more high-energy photons. Observations in the X-ray and gamma-ray bands therefore provide constraints on the proton luminosity, thereby putting constraints on the neutrino flux.

Proton cooling timescales

Considering that the proton mass is three orders of magnitude larger than the electron mass, $\frac{m_p}{m_e} \sim 10^3$, the energy loss rate for the proton synchrotron process is much smaller

than for the electron synchrotron process

$$\frac{\dot{E}_p}{\dot{E}_e} \propto \left(\frac{m_p}{m_e}\right)^{-2} \sim 10^{-6}. \tag{2.47}$$

Furthermore, $t_{\rm cool} \propto m^3$ for the synchrotron process, so

$$\frac{t_{\rm cool,p}}{t_{\rm cool,}e} \propto \left(\frac{m_p}{m_e}\right)^{3} \sim 10^{9}. \tag{2.48}$$

From this one can conclude that contrary to the case for electrons, the cooling of the proton spectrum from synchrotron radiation is negligible.
Cooling from Bethe-Heitler pair production and the photopion process described in Section 2.3 are on the other hand expected to play a more significant role in the cooling of the proton spectrum.

2.4.2 Electron spectrum

Following Ghisellini and Tavecchio (2009), the injected electron spectrum is a broken power law

$$Q(\gamma) = Q_0 \frac{(\gamma/\gamma_b)^{-s_1}}{1 + (\gamma/\gamma_b)^{-s_1+s_2}}. \tag{2.49}$$

Details can be found in Dermer et al. (2009) and Finke, Dermer, and Böttcher (2008). As explained in Section 2.2.1, synchrotron radiation causes the injected spectrum to cool.

Gamma-gamma pair production

Gamma-gamma pair production is the process

$$\gamma + \gamma \rightarrow e^- + e^+. \tag{2.50}$$

Its threshold energy is given by $2m_e \simeq 1\,\mathrm{MeV}$. Energy conservation gives us that the average Lorentz factor of these leptons is

$$\langle \gamma_e \rangle = \frac{\langle E_\gamma \rangle}{m_e c^2}, \tag{2.51}$$

where $\langle E_\gamma \rangle$ is the average energy of the two photons in the interaction. Inserting Equation 2.51 into Equation 2.28, one finds that

$$\nu_s = 9.45 \cdot 10^{15}\,\mathrm{Hz} \left(\frac{E_\gamma}{10^{10}\,\mathrm{eV}}\right)^2 \left(\frac{B}{1\,\mathrm{G}}\right) \left(\frac{\delta}{10}\right) \left(\frac{3}{1+z}\right). \tag{2.52}$$

Thus, gamma-rays can produce electron-positron pairs that themselves can emit synchrotron radiation in the UV/soft X-ray band. This synchrotron radiation can itself function as seed photons for the SSC process described in Section 2.2.1. As an estimate one can insert Equation 2.51 into 2.29 and find

$$\nu_{SSC} \simeq 2.71 \cdot 10^{24}\,\mathrm{Hz} \left(\frac{B}{1\,\mathrm{G}}\right) \left(\frac{E_\gamma}{10^{10}\,\mathrm{eV}}\right)^4 \left(\frac{\delta}{20}\right) \left(\frac{3}{1+z}\right), \tag{2.53}$$

corresponding to gamma-rays in the GeV range.

3 Method

The studied source sample consists of 19 high-redshift blazars. The leptonic and hadronic processes outlined in Chapter 2 are simulated numerically using the AM^3 package by Klinger et al. (2023). The energy densities output by AM^3 are then transformed into $\nu F(\nu)$ fluxes in the observer frame, producing the plots of the spectral energy distributions (SEDs) found in Chapter 4.
This chapter consists of a short description of the source sample, details concerning the AM^3 package and how the simulations were performed, an overview of the input parameters for the model, and a description of how the neutrino detection sensitivity of IceCube is approximated.

3.1 Source sample

The source sample is the same as in G11. These are high-redshift sources detected by the Fermi Large Area Telescope (LAT), with z ranging from 2.051 to 2.661. These blazars were selected in G11 as the "tip of the iceberg" of the blazar population in terms of intrinsic luminosity and external Compton dominance. In addition, G11 concluded that the sources in the sample have accretion disks with luminosity between $1 - 100\,\%$ of the Eddington luminosity (see their Figure 12). Therefore, these are potentially unique environments for neutrino production. Both because they are some of the most powerful blazars in the Universe in terms of jet power, but also in terms of the availability of external photon fields which can act as targets for neutrino production. The SEDs in Chapter 4 are fitted according to the Swift and Fermi-LAT data in G11. The data from the UVOT and XRT instruments are simultaneous, while the gamma-ray data are an average over the first 11 months of the First LAT AGN Catalog (1LAC) (G11). The 1LAC survey is detailed in Abdo et al. (2010). For all of the sources, data from the fourth Fermi Large Area Telescope catalog (4FGL) (Abdollahi et al. 2020), specifically Data Release 4 (Ballet et al. 2024), are used to provide an updated estimate of the gamma-ray fluxes. The source names are listed in Table 3.1, along with their respective 4FGL aliases. In the following, we use the same shorthand names for the sources as in G11.

Name	Alias	4FGL alias
0106+01	4C+01.02	4FGL J0108.6+0134
0157-4614	PMN	4FGL J0157.7-4614
0242+23	B2	4FGL J0245.4+2408
0322+222	TXS	4FGL J0325.7+2225
0420+022	PKS	4FGL J0422.8+0225
0451-28	PKS	4FGL J0453.1-2806
0458-02	PKS	4FGL J0501.2-0158
0601-70	PKS	4FGL J0601.1-7035
0625-5438	PMN	4FGL J0625.8-5441
0907+230	TXS	4FGL J0910.6+2247
0908+416	TXS	4FGL J0912.2+4127
1149-084	PKS	4FGL J1152.3-0839
1343+451	TXS	4FGL J1345.5+4453
1344-1723	PMN	4FGL J1344.2-1723
1537+2754	[WB92]	4FGL J1539.6+2743
1656.3-3302	Swift	4FGL J1656.3-3301
1959-4246	PMN	4FGL J1959.1-4247
2118+188	TXS	4FGL J2121.0+1901
2135-5006	PMN	4FGL J2135.3-5006

Table 3.1: Source names and their respective 4FGL aliases. The first two columns were retrieved from Table 1 in G11.

3.2 Numerical simulations

The numerical simulations were performed using the AM^3 package by Klinger et al. (2023). They describe AM^3 as "an open-source software to self-consistently compute the temporal evolution of energy spectra of photons, electrons, positrons, protons, neutrons, neutrinos and intermediate species" (Klinger et al. 2023). All calculations in AM^3 are done in the comoving frame of the jet. When initializing an AM^3 object, the relevant physics processes are switched on, the magnetic field is set and the injected particle densities are set. The primary particle densities consist of the electron spectrum, the proton spectrum, and the external photon fields. Furthermore, "the particle kinematics are described by a set of coupled integro-differential equations, derived from each species' Boltzmann equation, coupled via collision terms" (Klinger et al. 2023). The Boltzmann equation in question takes the form (Klinger et al. 2023)

$$\partial_t n(E,t) = -\partial_E \dot{E}(E,t) n(E,t) - \alpha(E,t) n(E,t) + Q(E,t), \tag{3.1}$$

where $n(E,t)$ is the differential number density of particles, $\dot{E}(E,t)$ is the cooling term, $\alpha(E,t)$ is the escape term and $Q(E,t)$ is the injection term. Further details are found in Klinger et al. (2023).

Following Ghisellini and Tavecchio (2009), the effects of adiabatic cooling and changes in the magnetic field as a result of expansion of the radiation zone are neglected. However,

the simulation is run for a time $t = 3 \cdot t_{\text{cross}} = 3R_{\text{blob}}/c$, as opposed to $t = t_{\text{cross}}$ in Ghisellini and Tavecchio (2009). Therefore, particle escape has to be included in this model. The escape time is set equal to the light crossing time $t_{\text{esc}} = t_{\text{cross}}$. For the electrons, electron synchrotron radiation, synchrotron self-absorption, synchrotron cooling, electron IC scattering and cooling from IC scattering are all switched on. Synchrotron radiation and IC scattering for the protons are switched on. Proton-proton collisions are switched off, following the reasoning in Section 2.3. The contributions from synchrotron and IC radiation from the secondary muons and pions are assumed to be negligible and thus switched off. Bethe-Heitler pair production, photo-pion production, decay of secondary muons and pions, and gamma-gamma pair production are all switched on. For details concerning how these processes are simulated by AM^3, see Klinger et al. (2023). For details concerning the leptonic and hadronic processes in general, see Chapter 2.

3.3 Input parameters

The fitting parameters from G11 are used. Their model does not include protons, so the hadronic parameters were chosen as described in Section 3.3.2. Some parameters are common for all of the sources. The rest are outlined in Table 3.2. The viewing angle is set to $\theta = 3^\circ$ for all of the sources.

Name	z	$R_{\rm diss}$	M	L'_e	L'_p	L_d	B'	Γ	$\gamma_{\rm e,\,break}$	$\gamma_{\rm e,\,max}$	$s_{e,1}$	$s_{e,2}$	$\gamma_{\rm e,\,min}$
[1]	[2]	[3]	[4]	[5]	[6]	[7]	[8]	[9]	[10]	[11]	[12]	[13]	[14]
0106+01	2.107	900	5.0e9	0.08	0.056	75	1.13	14	300	5.0e3	0	3.1	2.0
0157-4614	2.287	195	5.0e8	0.015	0.045	7.5	1.54	15	200	2.0e3	−1	3.0	5.7
0242+23	2.243	420	2.0e9	0.022	0.033	66	2.13	15	220	2.0e3	0.5	3.1	2.6
0322+222	2.066	450	3.0e9	0.06	0.15	45	2.06	12	150	3.0e3	0.5	3.1	3.7
0420+022	2.277	210	5.0e8	0.02	0.01	52.5	3.79	15	300	2.0e3	−1	3.2	4.9
0451-28	2.56	540	4.0e9	0.24	0.12	120	2.66	10	180	2.0e3	0	2.6	4.1
0458-02	2.291	472	3.5e9	0.07	0.154	37	2.14	10	200	5.0e3	0.8	3.0	4.9
0601-70	2.409	525	3.5e9	0.05	0.1	37	1.83	12.9	190	5.0e3	−1	3.1	2.8
0625-5438	2.051	270	1.0e9	0.03	0.015	42	2.64	15	240	5.0e3	0	4.0	3.9
0907+230	2.661	360	8.0e8	0.05	0.15	8.4	0.36	13	300	1.7e4	0.75	2.8	32.7
0908+416	2.563	180	1.0e9	0.025	0.15	12	1.06	14	150	3.0e3	0	3.1	7.0
1149-084	2.367	720	4.0e9	0.015	0.003	72	1.39	14	300	3.0e3	−1	3.0	1.8
1343+451	2.534	420	2.0e9	0.045	0.099	15	1.09	14	150	5.0e3	−1	2.8	6.5
1344-1723	2.409	330	1.0e9	0.027	0.0162	7.5	0.89	16	1.4e3	8.0e3	−1	2.5	26.2
1537+2754	2.19	120	1.0e9	0.015	0.0105	13.5	4.42	11.5	60	4.0e3	0.5	2.1	12.2
1656-3302	2.4	525	2.5e9	0.07	0.028	124	1.09	15	70	1.0e4	0.75	2.85	2.1
1959-4246	2.174	825	5.5e9	0.024	0.048	66	1.51	12.9	170	5.0e3	0	2.7	1.9
2118+188	2.18	270	1.5e9	0.022	0.0198	18	1.85	14	250	1.0e4	0.5	2.8	4.6
2135-5006	2.181	189	7.0e8	0.023	0.0288	10.5	2.02	14	180	2.0e3	−1	3.2	6.6

Table 3.2: Input parameters used to construct the SEDs. All columns except Col. [6] are the same as in G11. Therefore, the descriptions of the columns are also mostly the same as in G11, while Col. [6] is the result of this work. Col. [1]: source name; Col. [2]: redshift; Col. [3]: dissipation radius in units of 10^{15} cm; Col. [4]: black hole mass in solar masses; Col. [5]: luminosity of the injected electrons in the comoving frame of the blob, in units of $10^{45}\,{\rm erg\,s^{-1}}$; Col. [6]: luminosity of the injected protons in the comoving frame of the blob, in units of $10^{45}\,{\rm erg\,s^{-1}}$; Col. [7]: luminosity of the accretion disk in units of $10^{45}\,{\rm erg\,s^{-1}}$; Col. [8]: magnetic field in the jet in units of Gauss; Col. [9]: bulk Lorentz factor of electrons and protons at $R_{\rm diss}$; Col. [10] and [11]: break and maximum random Lorentz factors of the injected electrons; Col. [12] and [13]: slopes of the injected electron distribution below and above $\gamma_{\rm e,\,break}$; Col. [14]: minimum random Lorentz factor of the injected electrons. Note that in G11 $\gamma_{\rm e,\,min}$ is a derived parameter, while here it is used as an input when defining the injected electron spectrum in AM^3.

3.3.1 Leptonic parameters

The leptonic parameters, i.e. those characterising the injected electron spectrum, are all taken from G11. These are found in Table 3.2.

3.3.2 Hadronic parameters

The proton spectrum is modelled as a $dN/dE \propto E^{-2}$ power-law spectrum, following the reasoning in Section 2.4.1. The minimum proton energy is set to be the rest mass energy. The maximum proton energy is found using Equation 2.46 and setting the parameter $\eta = 1$, i.e. maximum acceleration efficiency. The value for each of the sources is given in Table 3.3. The proton luminosities were optimized by eye and are given in Table 3.2. The introduction of protons is allowed as long as their contribution to the SED is subdominant. The strictest constraints arise from the Swift XRT data. Higher proton luminosity results in more high-energy gamma-rays from photohadronic processes, see Section 2.3. These

gamma-rays, in turn, produce electron-positron pairs that radiate X-rays, as described in Section 2.4.2. The XRT data thus place constraints on the proton luminosity.

Name	$\gamma_{\mathrm{p,\,max}}$
0106+01	2.58e10
0157-4614	8.45e09
0242+23	2.58e10
0322+222	2.58e10
0420+022	1.78e10
0451-28	5.43e10
0458-02	3.74e10
0601-70	2.58e10
0625-5438	1.78e10
0907+230	4.01e09
0908+416	5.82e09
1149-084	2.58e10
1343+451	1.23e10
1344-1723	8.45e09
1537+2754	1.78e10
1656-3302	1.23e10
1959-4246	3.74e10
2118+188	1.23e10
2135-5006	1.23e10

Table 3.3: Maximum Lorentz factor of the injected proton spectrum.

It can be useful to compare the proton luminosity with both the electron luminosity and the Eddington luminosity of the disk. The ratio $L_p/L_e \equiv \xi$ is called the baryon loading factor. The value of ξ for all of the sources is shown in Table 3.4. It has a relatively low value for all of the sources, with ξ ranging from 0.2 to 6.0. The Eddington luminosity of the disk is given by Equation 2.3. The ratio between L_p and L_{Edd} is also shown in Table 3.4. It is evident that the proton luminosity is well below the Eddington luminosity, suggesting that it is set at a physically realistic level.

Name	ξ	$L_p/L_{\rm Edd}$
0106+01	0.7	8.89e−5
0157-4614	3.0	7.14e−4
0242+23	1.5	1.31e−4
0322+222	2.5	3.97e−4
0420+022	0.5	1.59e−4
0451-28	0.5	2.38e−4
0458-02	2.2	3.49e−4
0601-70	2.0	2.27e−4
0625-5438	0.5	1.19e−4
0907+230	3.0	1.49e−3
0908+416	6.0	1.19e−3
1149-084	0.2	5.95e−6
1343+451	2.2	3.93e−4
1344-1723	0.6	1.29e−4
1537+2754	0.7	8.33e−5
1656-3302	0.4	8.89e−5
1959-4246	2.0	6.93e−5
2118+188	0.9	1.05e−4
2135-5006	1.25	3.26e−4

Table 3.4: Baryon loading factor, $\xi = L_p/L_e$; and the ratio between proton luminosity in the jet and Eddington luminosity of the accretion disk, $L_p/L_{\rm Edd}$.

3.3.3 Implementation of external photon fields

The photon fields from the accretion disk, the X-ray corona, the BLR and the IR torus are included in the model. Using the parameters from G11, the gamma-ray peak of the SEDs will have a cutoff at 10^{24} Hz. This corresponds to an energy of around 1 GeV. In Section 2.1.6, it was stated that attenuation of the gamma-ray spectrum is negligible below 10 GeV. Therefore, absorption from the EBL is not included in this model.
For most of the sources in the sample, $R_{diss} < R_{BLR}$, i.e. the radiation zone is located between the black hole and the BLR. The energy density of the BLR photon field in the jet frame, U'_{BLR}, is then given by $17\Gamma^2/12\,U_{BLR}$ (Ghisellini and Tavecchio 2009). For $R_{diss} > R_{BLR}$, Equation 20 in Ghisellini and Tavecchio (2009) is used. For the sources in the sample, $R_{\rm diss} \sim 10^{17}\,{\rm cm} \sim 10^3 R_S\,(10^9 M_\odot/M)$, see Table 3.2. For our model, $R_{\rm disk} \sim 10^2 R_S$, so the condition $R_{\rm diss} > R_{\rm disk}$ is fulfilled. Therefore, as explained in Section 2.1, the energy density from the accretion disk and the X-ray corona in the comoving frame of the blob is negligible for these sources. Consequently, these two fields are not included in the AM^3 simulations as target fields. They are however included in the final SEDs in Chapter 4.

Accretion disk

The accretion disk is modelled as a multi-temperature Shakura-Sunyaev disk, where the temperature depends on the radius as in Equation 2.5. At 50 radii with equal spacing between $R_{\rm in} = 3R_S$ and $R_{\rm out} = 300R_S$, where R_S is the Schwarzschild radius, the black-body spectra from each ring segment are evaluated. The total spectrum is the sum of the

blackbody spectra of each of these ring segments. Its luminosity is given in Table 3.2.

X-ray corona

As in Ghisellini and Tavecchio (2009), the X-ray corona is modeled as a region close to the black hole. Its flux is described by a power law with an exponential cutoff, see Equation 2.6. The parameters in Equation 2.6 are set to $\alpha_X = 1$ and $h\nu_c = 150\,\mathrm{keV}$, following Ghisellini and Tavecchio (2009). Its luminosity is set to $L_X = 0.3 \cdot L_d$ where L_d is the luminosity of the accretion disk. Except for the source named 1149-084, where the luminosity is set to $L_X = 0.03 \cdot L_d$ to give better agreement with the thermal spectrum in G11.

BLR

As in Rodrigues et al. (2023), the BLR is modelled as a thin spherical shell, and the photon spectrum from the BLR is modelled as a Gaussian distribution centered at $h\nu_{\mathrm{Ly}} = 10.2\,\mathrm{eV}$ with half-width $h\Delta\nu = 0.05 \cdot h\nu_{\mathrm{Ly}}$ and luminosity $L_{\mathrm{BLR}} = 0.1 \cdot L_d$. The BLR radius R_{BLR} is determined by the disk luminosity L_d given in Table 3.2 through Equation 2.7. Transformation of the energy density to the comoving frame of the blob follows Ghisellini and Tavecchio (2009) and Rodrigues et al. (2023).

IR Torus

Following Ghisellini and Tavecchio (2009), the photon spectrum from the IR torus is modeled as a blackbody spectrum with a temperature 510 K. Its luminosity is set to $L_{\mathrm{IR}} = 0.5 \cdot L_d$. The IR torus radius R_{IR} is determined by the disk luminosity L_d given by Table 3.2 through Equation 2.9. Transformation of the energy density to the comoving frame of the blob follows Ghisellini and Tavecchio (2009) and Rodrigues et al. (2023).

3.4 4FGL data

The 4FGL data are taken from the HEASARC archive. The data are presented as a power-law fit in the $100\,\mathrm{MeV} - 1\,\mathrm{TeV}$ range, with the form

$$\frac{dN}{dE} = N_0 \left(\frac{E}{E_{\mathrm{pivot}}} \right)^{\alpha}. \tag{3.2}$$

The normalization constant N_0, the pivot energy E_{pivot} and the spectral index α were all retrieved from the HEASARC archive, along with the associated errors σ_{N_0} and σ_α. The aliases used in the 4FGL catalog for all of the sources in this sample are shown in Table 3.1. Propagation of errors gives the error in dN/dE,

$$\sigma\left(\frac{dN}{dE}\right) = N_0 \left(\frac{E}{E_{\mathrm{pivot}}} \right)^{\alpha} \sqrt{\left(\frac{\sigma_{N_0}}{N_0}\right)^2 + \left(\sigma_\alpha \ln\left(\frac{E}{E_{\mathrm{pivot}}}\right)\right)^2}. \tag{3.3}$$

Using this, the plotted 4FGL $\pm 1\sigma$ bands in the $\nu F(\nu)$ plots in Chapter 4 are given by

$$E^2 N_0 \left(\frac{E}{E_{\mathrm{pivot}}} \right)^{\alpha} \pm E^2 \sigma \left(\frac{dN}{dE}\right), \tag{3.4}$$

where $\sigma\left(\frac{dN}{dE}\right)$ is given by Equation 3.3.

3.5 Neutrino detection sensitivity

The detection sensitivity of neutrinos by IceCube is approximated following Aartsen et al. (2020). The theoretical future detection sensitivity is approximated following van Santen (2018). The sensitivity for the different sources is found by reading off the graph for a E^{-2} neutrino spectrum in Figure 3.1. For the theoretical future sensitivity, the graph in Figure 3.2 is used. As seen in Equations 2.42 and 2.43, the flavour ratio of neutrinos at the source is $\nu_e : \nu_\mu : \nu_\tau = 1 : 2 : 0$. However, because of neutrino oscillations, the flavour composition at the detector is $\nu_e : \nu_\mu : \nu_\tau \simeq 1 : 1 : 1$ (Ahlers and Halzen 2018). The flux sensitivity in Figure 3.1 applies to muon neutrinos and antineutrinos only, and the flavour composition at the detector implies that muon neutrinos make up 1/3 of the total neutrino flux. Therefore, the sensitivity represented in the SED plots in Chapter 4 is multiplied by 3 with respect to that in Figure 3.1. The flux sensitivity in Figure 3.1 is only given for neutrinos with energy 1 TeV, but in the plot, it is extended to the interval 1 TeV − 1 PeV. The same procedure is followed for the flux sensitivity in Figure 3.2.

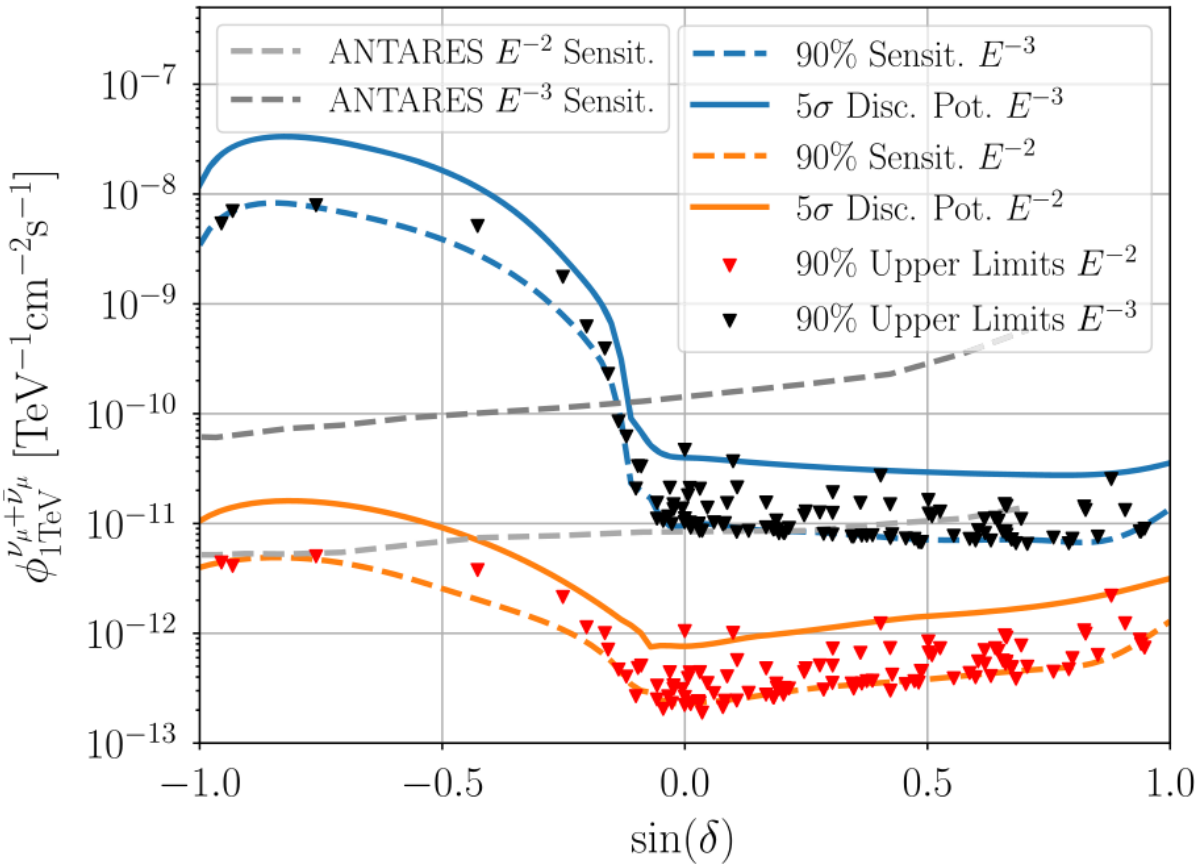

Figure 3.1: "90% confidence level median sensitivity and 5σ discovery potential as a function of source declination for a neutrino source with an E^{-2} and E^{-3} spectrum" (Aartsen et al. 2020). Figure retrieved from Aartsen et al. (2020). The solid orange line shows the 5σ discovery potential for a E^{-2} neutrino spectrum. Note the asymmetry in the flux sensitivity between neutrinos coming from the northern and southern hemispheres.

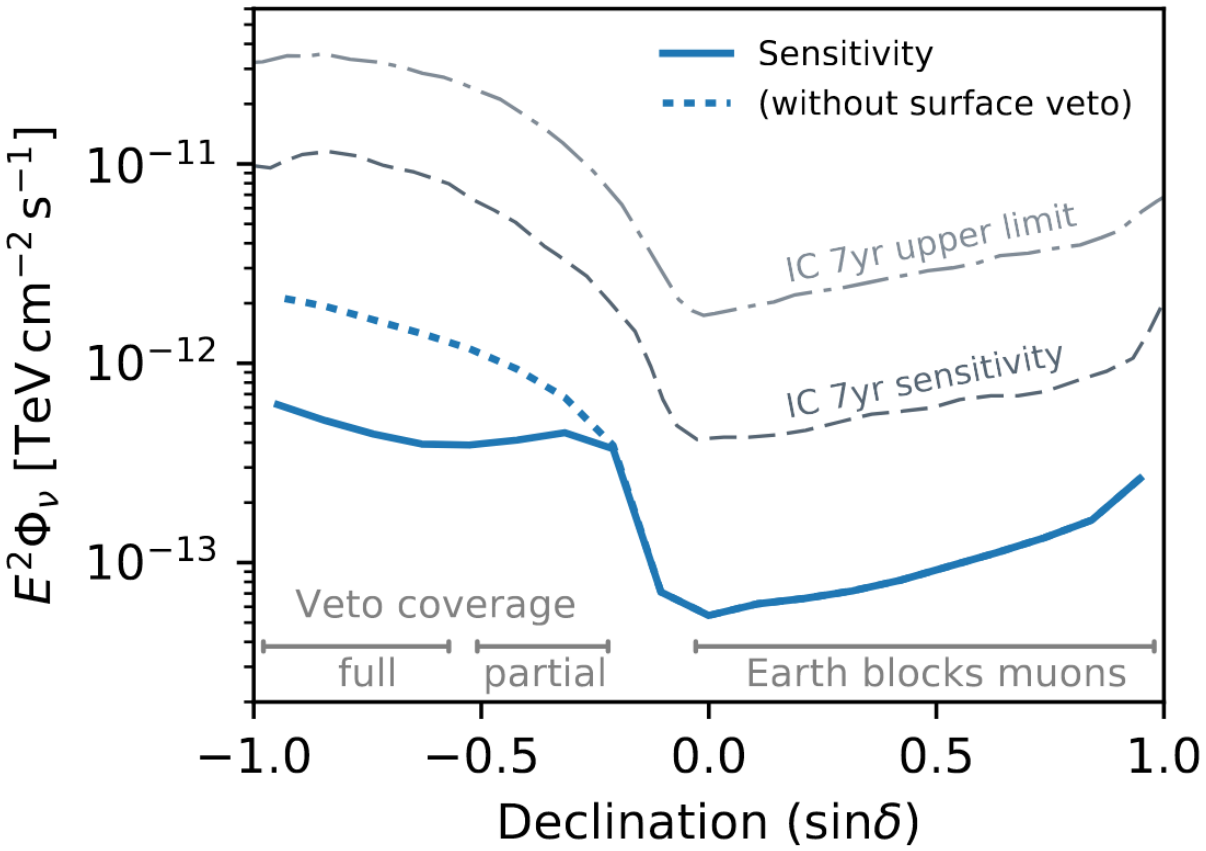

Figure 3.2: "Integrated sensitivity for an E^{-2} flux from a single source after 15 years of IceCube operation followed by 15 years of IceCube-Gen2" (van Santen 2018). Figure retrieved from van Santen (2018). The sensitivity "without surface veto" is used in the plots in Chapter 4. Note the asymmetry in the flux sensitivity between neutrinos coming from the northern and southern hemispheres.

As one can see from Figures 3.1 and 3.2, IceCube's sensitivity has an asymmetry between the northern and southern hemispheres. The KM3NeT/ARCA detector currently under construction in the Mediterranean Sea will provide better sensitivity for sources in the southern hemisphere (Muller, Heijboer, and Eeden 2023). Figure 3.3 shows the predicted neutrino sensitivity for ARCA230, which is the full configuration of the detector. Here, we follow the same procedure as for the IceCube sensitivity when including it in the SEDs in Chapter 4.

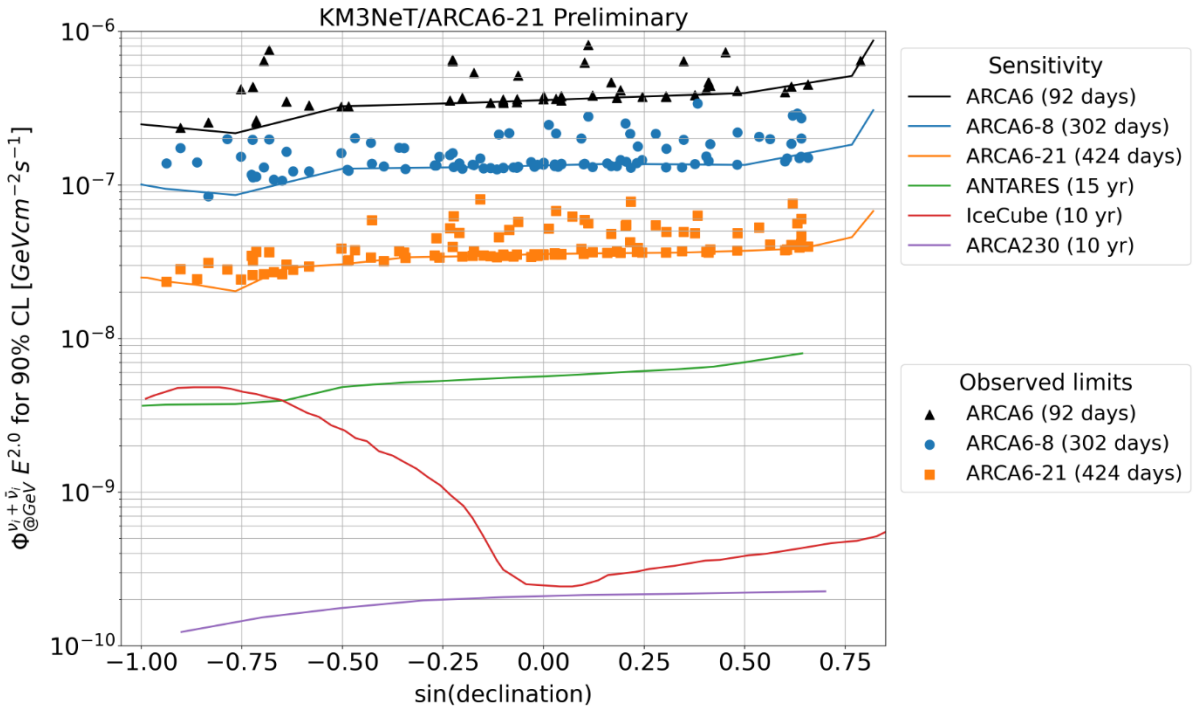

Figure 3.3: Predicted future neutrino sensitivity after 10 years of ARCA230 as a function of source declination. Figure retrieved from Muller, Heijboer, and Eeden (2023). The purple line at the bottom shows the predicted flux sensitivity of ARCA230.

4 Results and discussion

This chapter consists of a presentation and discussion of the results. The spectral energy distributions (SEDs) for the 19 blazars in the sample are compared. The relationship between neutrino flux and gamma-ray flux is discussed.

The results are summarized in 19 SEDs, found in Figures 4.3, 4.4, 4.9, 4.10, 4.14, 4.15, 4.16, 4.5, 4.17, 4.11, 4.12, 4.13, 4.19, 4.20, 4.7, 4.21, 4.6, 4.8 and 4.18. The general shape of the SED for all of the sources consists of the synchrotron radiation dominating in the radio; the thermal radiation from the torus, accretion disk and the corona contributing significantly to the flux in the infrared, optical and ultraviolet, and the X-rays respectively; the synchrotron self-Compton contributing significantly to the X-ray flux; and the external Compton dominating the gamma-rays from 1 MeV up to about 10 GeV where Klein-Nishina effects cause the spectrum to be suppressed. Additionally, synchrotron and IC radiation from secondary electrons and positrons produced in photon-photon interactions contribute significantly to the energy flux in the X-rays and gamma-rays. Along with radiation from the electrons and positrons produced in the Bethe-Heitler process, they are also the dominant source of electromagnetic radiation for TeV energies. In the PeV energies, the neutrino flux dominates. The neutrino flux also dominates up to about 10^{19} eV where there is a hard cutoff. Photons produced in π^0 decay provide a subdominant contribution for the highest energies. All of the processes mentioned in this paragraph are explained in Chapter 2.

None of the sources have large enough neutrino fluxes to be detected by IceCube in its first ten years. This was expected, since no astrophysical neutrinos detected by IceCube until now have been associated with any of these sources. Even though ARCA230 will be more sensitive to astrophysical neutrinos than IceCube, and more sensitive to sources at large negative declinations than IceCube-Gen2, none of the sources are expected to be detectable within its first 10 years. Furthermore, the plots suggest that most of the blazars in the sample will not be detectable by IceCube-Gen2 within its first 15 years. However, the sources named 0106+01, 0322+222 and 0458-02 may be detectable.

4.1 Comparison between the different blazar SEDs

Most of the SEDs show a good fit with the data points from G11. Common for all of the sources is that the external Compton (EC) component of the flux is lower in the X-rays compared to what was found in G11. Most of the sources also have a higher X-ray flux from the synchrotron self-Compton process compared to the SEDs in G11, despite having approximately equal synchrotron fluxes. If the energy density of the seed photons is the same, then the difference must lie in the electron spectrum. The main contribution to the SSC flux comes from electrons at the break energy $E = \gamma_b m_e c^2$. As seen in Table 3.2, the break energy Lorentz factor is $\gamma_b \sim 10^2$ for most of the sources. When the same electrons interact with the external photon fields in the EC process, gamma-rays with energy $E \sim 10^6$ eV are produced, according to Equation 2.27. This suggests that there is a connection between the lower EC flux and the higher SSC flux, in that they are both tied to the electrons at the break energy.

The source of this discrepancy between this model and the model of G11 is unknown. Since we do not have access to the code they used, we have to try a different approach when investigating this. The first thing one can investigate is whether the difference in how the BLR is modelled is the culprit. In this model, the BLR spectrum is completely dominated by the hydrogen Lyman alpha emission line. This is not necessarily accurate, and the way the BLR is modelled does affect the gamma-ray spectrum. In Rodrigues et al. (2023), they use a similar model as the one used here, though they also include the helium Lyman alpha line with half the luminosity of the hydrogen line. For simplicity, this was not included in this model. In G11 the BLR spectrum is modelled as a black body peaking at the hydrogen Lyman alpha line, following Ghisellini and Tavecchio (2009). In Figure 4.1, a model using the black body spectrum like in G11 is compared with one of the plots from our model.

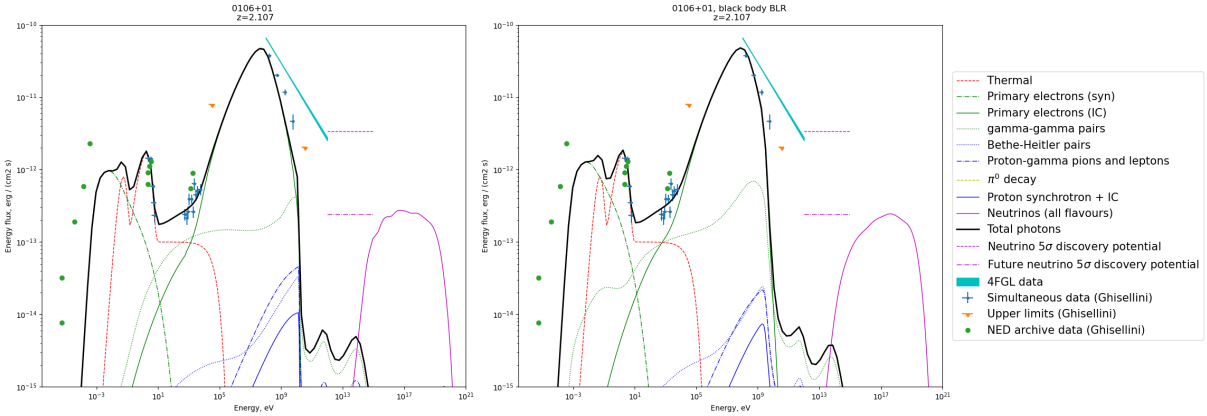

Figure 4.1: Comparison between the SEDs of 0106+01 using a black body BLR as in G11, and a Gaussian BLR centered at hydrogen Lyman alpha line as described in Chapter 3. See Figure 4.3 for details.

The difference in how the BLR is modelled only makes minor changes to the gamma-ray fit, along with making the neutrino flux smoother. The size of the neutrino flux is not significantly affected. Furthermore, the change to the EC component of the X-ray flux is negligible. Figure 4.1 is an illustrative example. The same behaviour is observed for all of the sources, but their plots are excluded here for the sake of brevity.

Another hypothesis is that there is something wrong with how AM^3 is used to calculate the energy densities. To test this hypothesis, we try to reproduce the SED of the well-studied blazar TXS 0506+056. Following Keivani et al. (2018), one finds the plot in Figure 4.2.

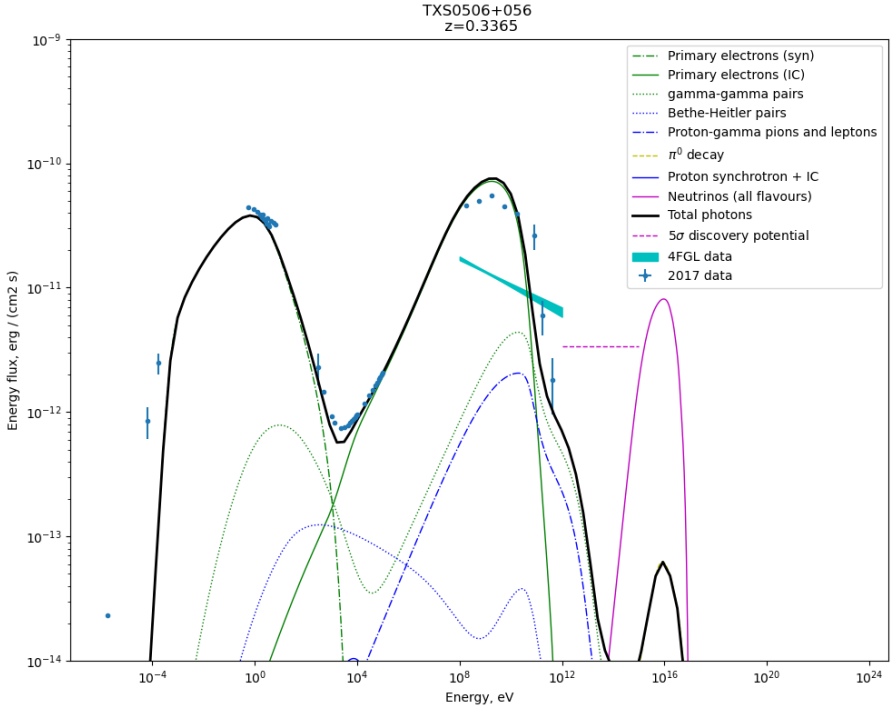

Figure 4.2: SED of TXS0506+056, using the same setup as in Figure 4.3, but using model parameters and external photon field from Keivani et al. (2018). This corresponds to Figure 4 in their paper, using the model named LMBB2b.

Figure 4.2 shows a decent fit with the data points. There is a slight undershooting of the highest energy gamma-ray data points, while the peak overshoots the data points. The overshooting is more severe compared to the 4FGL data. The neutrino flux is also about twice as large compared to that of Keivani et al. (2018). All in all, with the exception of the mentioned small discrepancies, the agreement with Keivani et al. (2018) is good. Therefore, we attribute the observed differences, of at most a factor of 2, to different conventions used by the different codes but conclude that the overall leptohadronic emission obtained with AM3 in what follows is correct.

All the individual sources in the sample are discussed below. They are grouped according to how well they fit the X-ray data, since the X-ray observations place the strictest constraints on the proton luminosity and thus also the neutrino flux.

4.1.1 Blazar SEDs with the best fit of the X-ray data

The SEDs of blazars 0106+01, 0157-4614, 0601-70, 1537+2754, 1959-4246 and 2118+188 show good agreement with the XRT data retrieved from G11. These SEDs are shown in Figures 4.3, 4.4, 4.5, 4.7, 4.6 and 4.8 respectively.

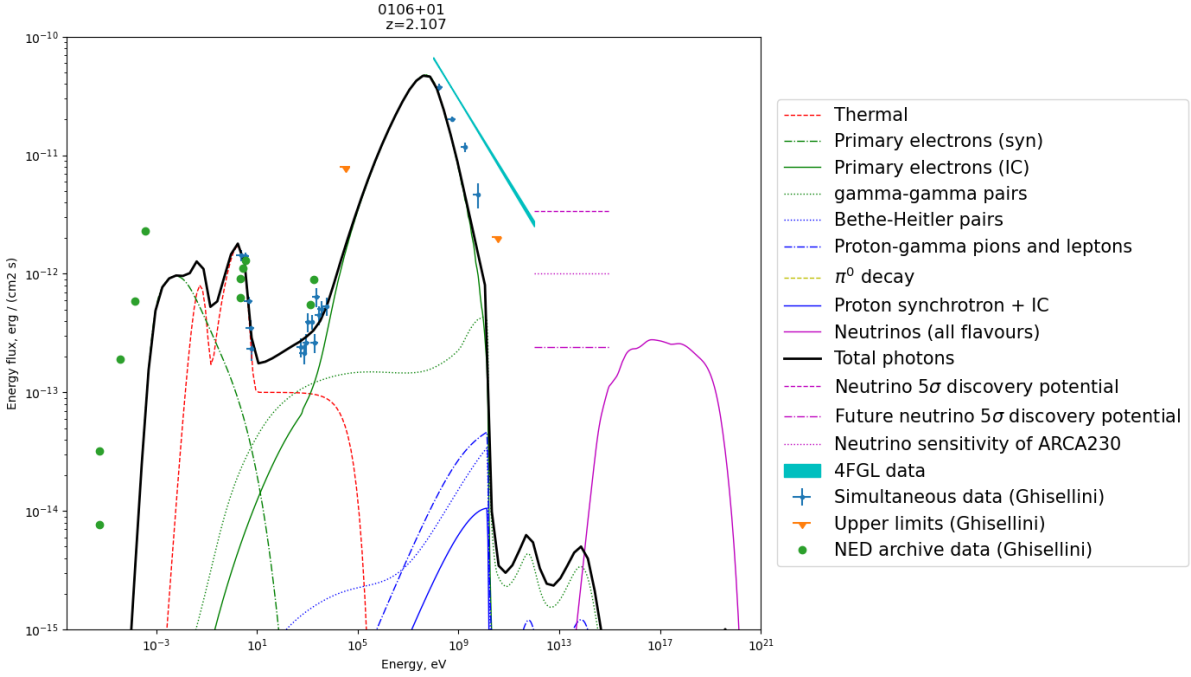

Figure 4.3: SED of blazar 0106+01 in the observer frame. Simultaneous data, upper limits and NED archive data were retrieved from G11 as described in Section 3.1. 4FGL data were retrieved from the HEASARC archive. The 4FGL data is represented by a band showing the power law fit of the 14-year gamma-ray data $\pm 1\sigma$. The neutrino 5σ discovery potential is estimated using the results by Aartsen et al. (2020) as described in Section 3.5. The IC radiation is the sum of the SSC and EC components. The thermal spectrum is the sum of radiation from the IR torus, the accretion disk, and the X-ray corona. The flux from secondary pions and leptons from the gamma-gamma, Bethe-Heitler and proton-gamma processes consist of both synchrotron and IC radiation. The neutrino flux is summed over all three neutrino flavours. Since the neutrino flux is summed over all flavours, the detection sensitivity is multiplied by 3 with respect to the sensitivity reported for ν_μ and $\bar{\nu}_\mu$ in Aartsen et al. (2020). The same goes for the future neutrino flux sensitivities by IceCube-Gen2 reported in van Santen (2018), and the future sensitivity of ARCA230 reported in Muller, Heijboer, and Eeden (2023). The estimated future neutrino sensitivity and the neutrino flux are close to intersecting at PeV energies.

Blazar 0106+01's SED slightly undershoots the gamma-ray data points from G11 for energies larger than 1 GeV. The band showing the power law fit of the 4FGL data shows an even larger gamma-ray flux than what was used in G11. This suggests that there is some variability in the gamma-ray flux of this source, since the 11-month 1LAC data show a smaller energy flux than the 14-year 4FGL data. In any case, neither the 1LAC nor the 4FGL data place any strict constraints on the proton luminosity. The strictest constraint comes from the X-ray data. A larger proton luminosity results in more gamma-gamma electron-positron pairs. As can be seen from Figure 4.3, the X-ray emissions from the gamma-gamma pairs cannot be any higher without interfering with the overall fit. The justification for the introduction of the protons is that their contribution is subdominant. If the proton luminosity is set any higher, their contribution to the X-ray flux would not be subdominant anymore. The baryon loading factor, shown in Table 3.4, for the source, is $\xi = 0.7$, meaning its proton luminosity is relatively low. However, its small declination is very favourable to observation by IceCube. As a result, its neutrino flux is close to

intersecting the line showing the predicted future flux sensitivity of IceCube-Gen2, given by Figure 3.2. The plot in Figure 4.3 thus suggests that neutrinos with PeV energies could be observable by IceCube-Gen2 within its first 15 years.

Blazar 0157-4614's SED shows a better agreement with the data points from G11 in the gamma-rays than 0106+01. The graph also intersects the 4FGL band, as can be seen in Figure 4.4. However, the neutrino flux is not high enough to be detectable by IceCube. This is mainly due to the source having a declination of $\delta \approx -46°$. As seen in Figures 3.1 and 3.2, IceCube's sensitivity to astrophysical neutrinos is the highest for sources with declination close to 0°. Similarly, blazar 0601-70 is not expected to be detectable by IceCube, despite its relatively large neutrino flux, see Figure 4.5. It slightly undershoots the gamma-ray data points, but it does intersect the 4FGL band. Its overall fit is decent. The SED of 1959-4246 slightly undershoots the gamma-ray data points for GeV energies, as can be seen in Figure 4.6. Like 0157-4614 and 0601-70 it too intersects the 4FGL band. It also has the same problem with declination as 0157-4614 and 0601-70. Despite its strong neutrino flux arising from its decent proton luminosity, it will not be observable by IceCube in the foreseeable future.

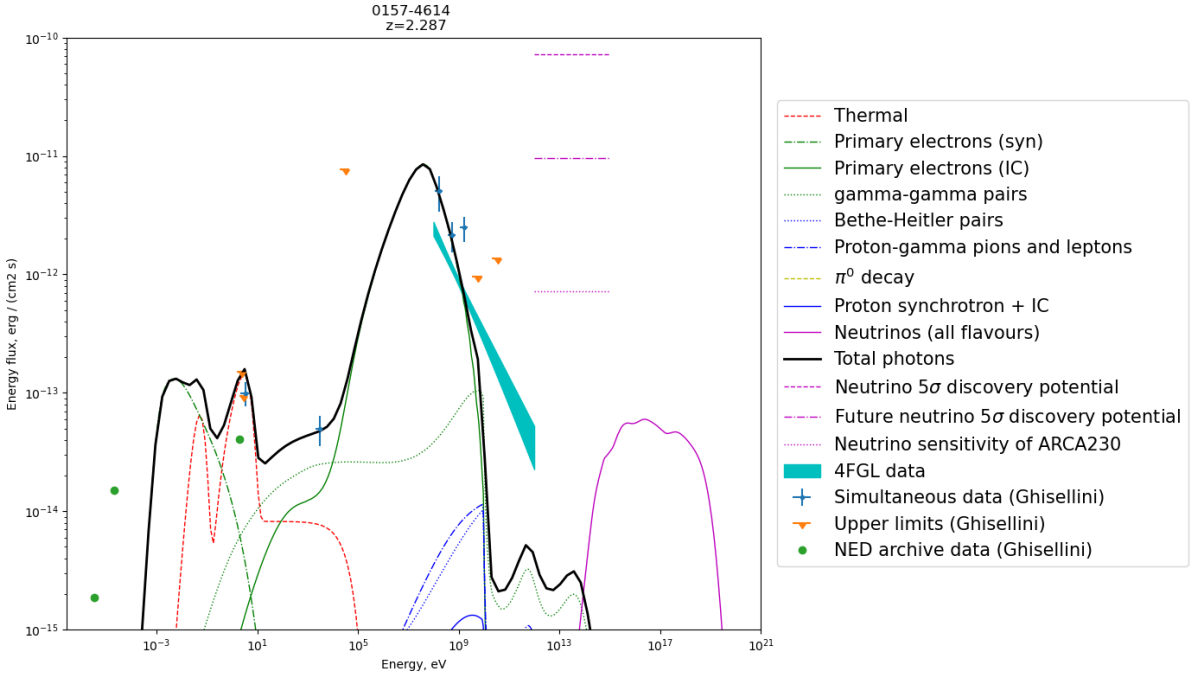

Figure 4.4: SED of blazar 0157-4614 in the observer frame. See Figure 4.3 for details.

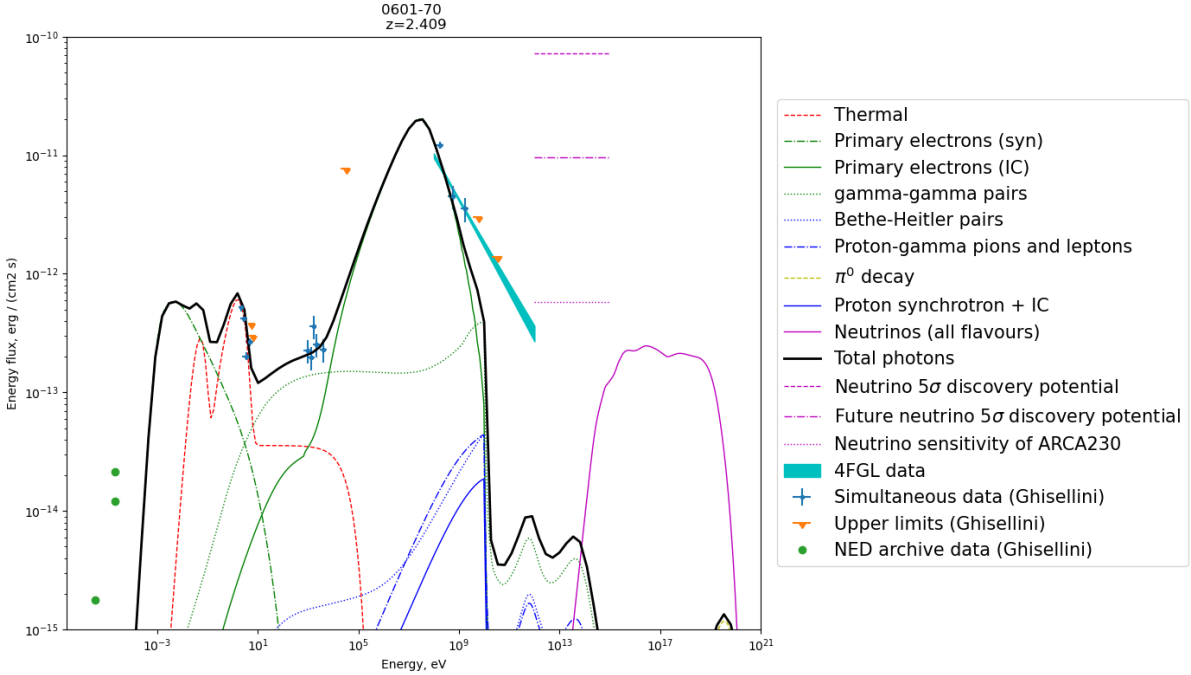

Figure 4.5: SED of blazar 0601-70 in the observer frame. See Figure 4.3 for details.

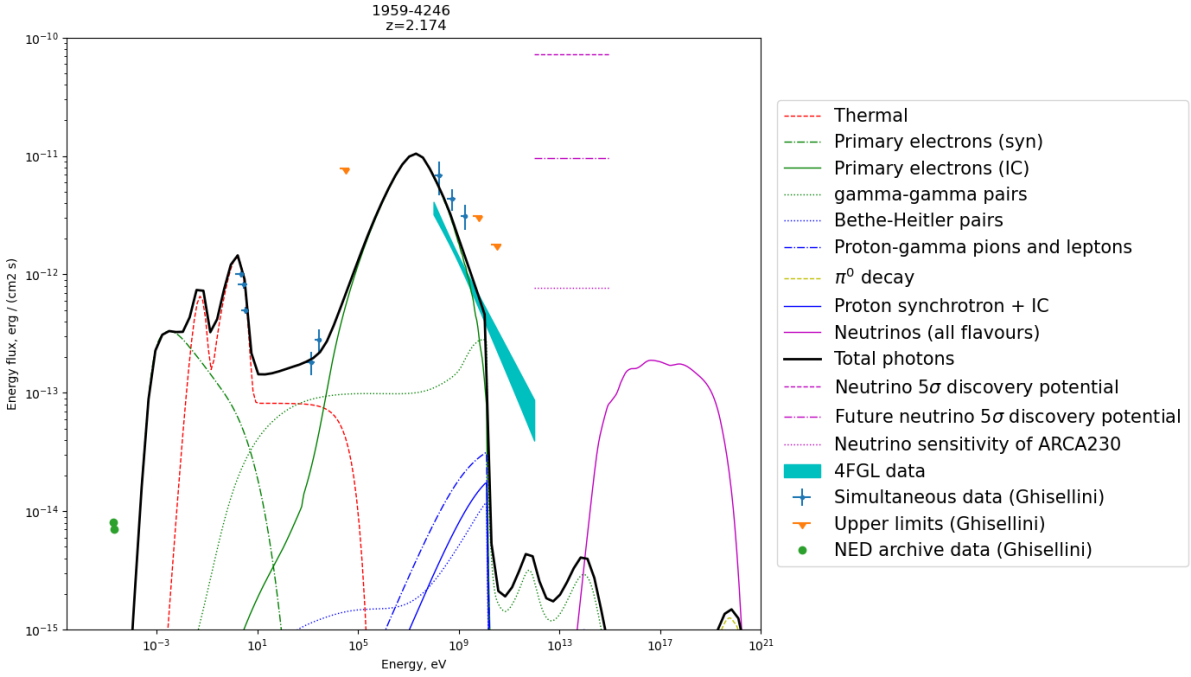

Figure 4.6: SED of blazar 1959-4246 in the observer frame. See Figure 4.3 for details.

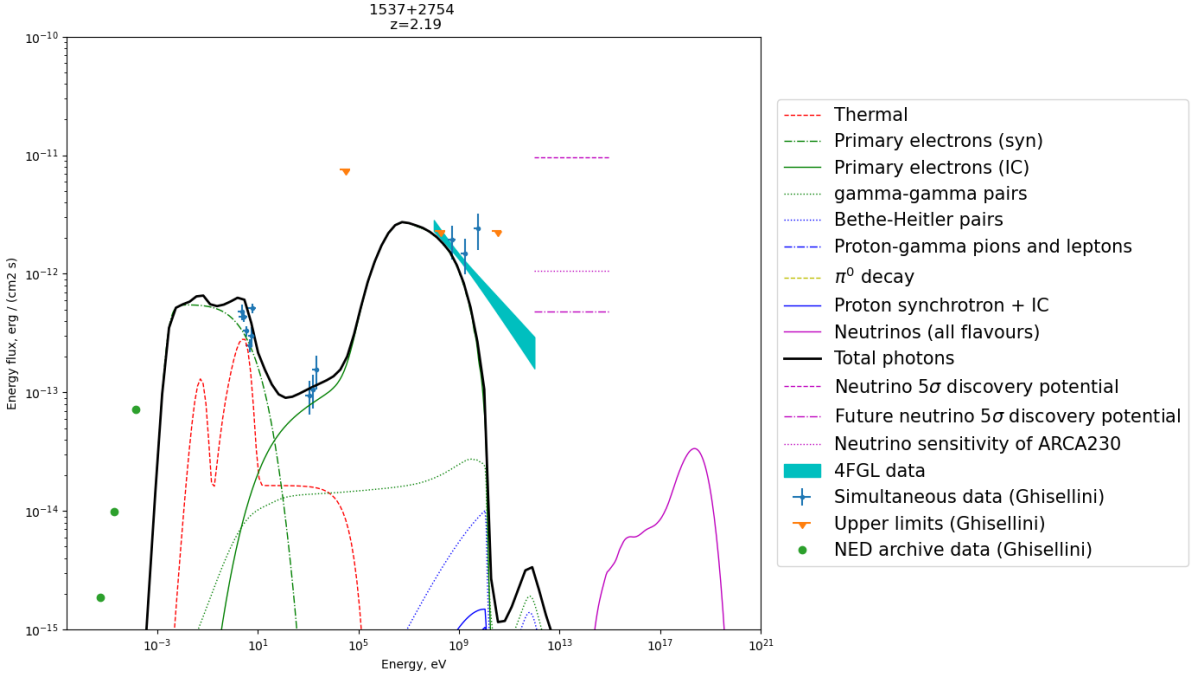

Figure 4.7: SED of blazar 1537+2754 in the observer frame. See Figure 4.3 for details.

Blazar 1537+2754 on the other hand is at a declination that is more favourable, but its neutrino flux is relatively low. This is partly due to the low proton luminosity, where $L_p = 0.7L_e$. Comparing the energy flux from the gamma-gamma pairs with the 4FGL band, one could justify a higher proton luminosity, but again the X-ray observations put constraints on it. The graph of 1537+2754's SED undershoots the data points above 1 GeV and also the 4FGL data band, see Figure 4.7.

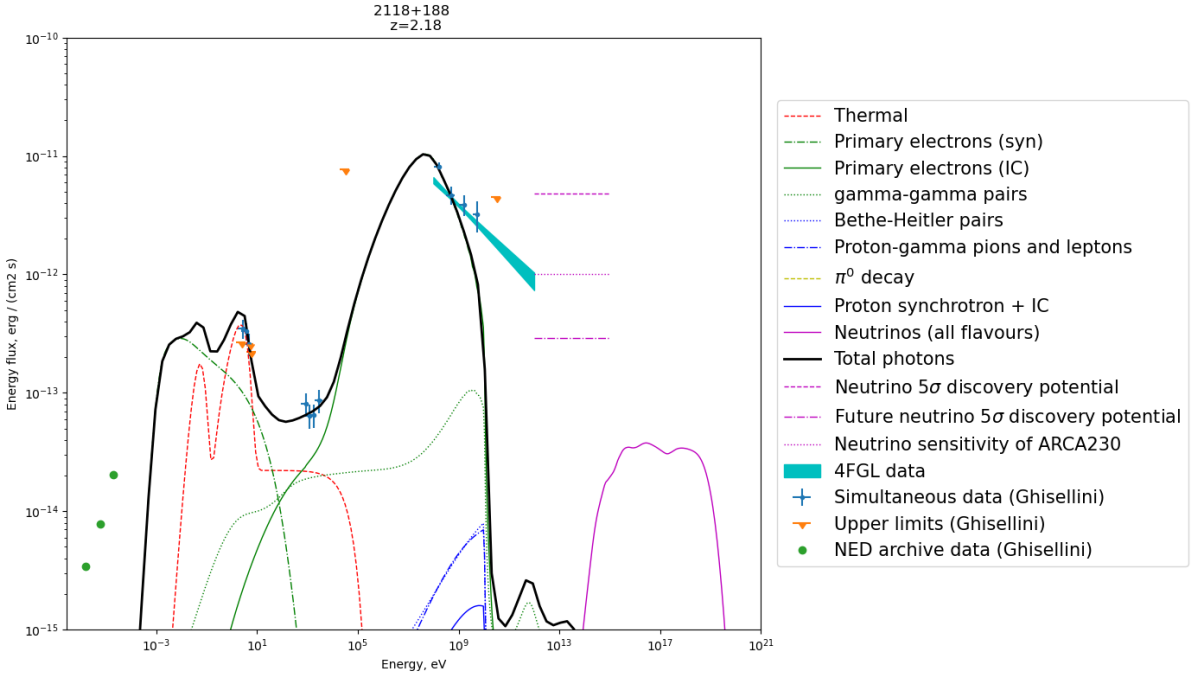

Figure 4.8: SED of blazar 2118+188 in the observer frame. See Figure 4.3 for details.

Similarly, the SED of 2118+188, seen in Figure 4.8, shows a neutrino flux too weak to be detectable, despite its favourable declination. The 4FGL data shows that the average gamma-ray flux is large. Its overall fit with the data is good, but it undershoots both the data points from G11 and the 4FGL band at GeV energies. Its proton luminosity is relatively low at $L_p = 0.9L_e$. Again it is the X-ray data that puts the strictest constraints on the proton luminosity and thus on the neutrino flux. In the end, the neutrino flux is too low to be detectable.

In summary, the SEDs of the sources discussed in this subsection all show a good fit with the X-ray data. For several of the blazar SEDs, the gamma-ray flux undershoots the data points from G11 and the 4FGL data. The high gamma-ray flux could give room for more protons, but the X-ray observations place strict constraints on it. Blazar 0106+01, seen in Figure 4.3, appears to be the most likely to produce a neutrino flux detectable by IceCube-Gen2 within its first 15 years.

4.1.2 Blazar SEDs that fit the X-ray data reasonably well

The SEDs of blazars 0242+23, 0322+222, 0907+230, 0908+416 and 1149-084, shown in Figures 4.9, 4.10, 4.11, 4.12 and 4.13 show a reasonably good fit with the X-ray data.

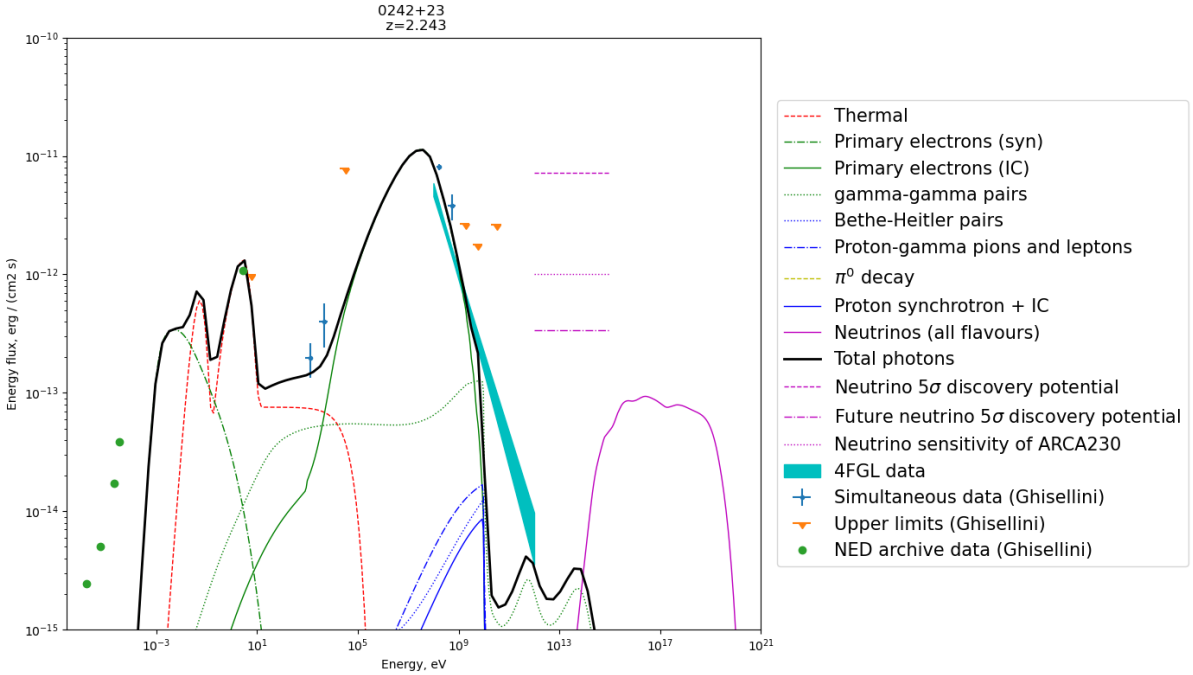

Figure 4.9: SED of blazar 0242+23 in the observer frame. See Figure 4.3 for details. The estimated future neutrino sensitivity and the neutrino flux intersect at PeV energies.

Source 0242+23 is at a favourable declination. The SED in Figure 4.9 shows an overall good fit with the data points from G11 and the 4FGL data. Differing from the sources discussed above, the strictest constraints on blazar 0242+23's proton luminosity come from the 4FGL data, not the X-ray data. Nonetheless, the source has a relatively decent baryon loading factor, seen in Table 3.4, of $\xi = 1.5$. However, due to its relatively low electron luminosity, this value ξ does not give rise to a sufficiently large proton luminosity.

This in turn makes the neutrino flux too small, so that it will not be detectable within the first 15 years of IceCube-Gen2, despite its favourable declination.

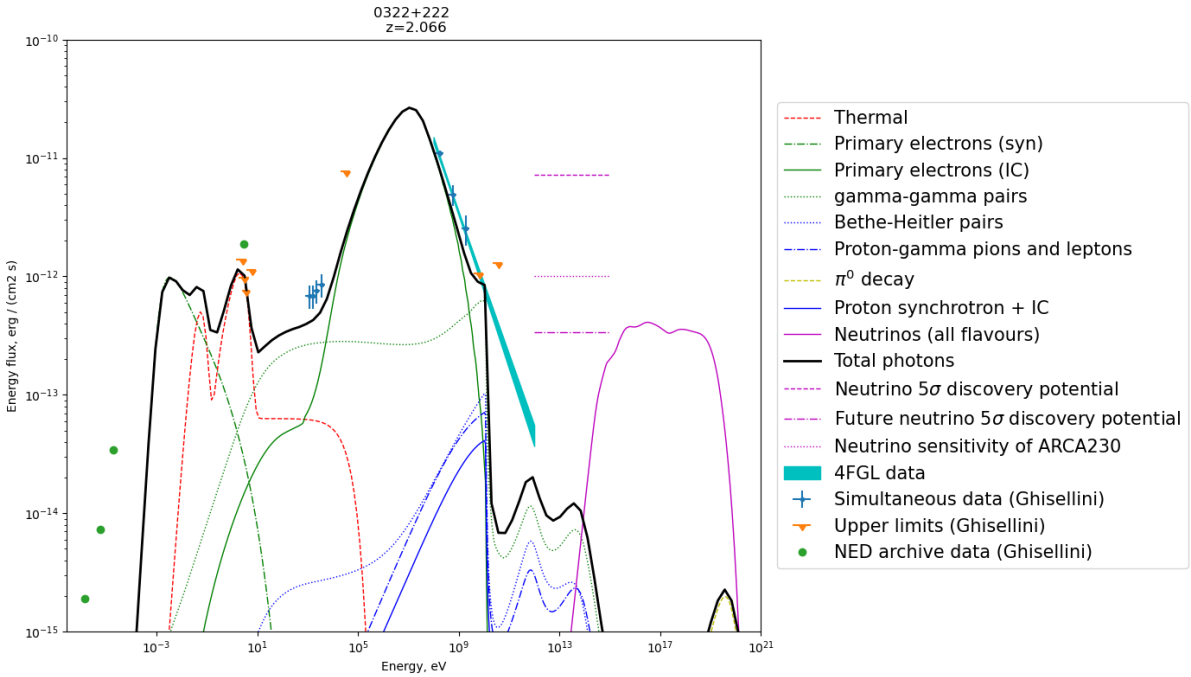

Figure 4.10: SED of blazar 0322+222 in the observer frame. See Figure 4.3 for details. The estimated future neutrino sensitivity and the neutrino flux intersect at PeV energies.

In the case of 0322+222, the fit with the X-ray data is decent in terms of spectral shape, but a little too low in terms of energy flux. Its fit with the gamma-ray data is also decent, with both the 1LAC data from G11 and the 4FGL data. The combination of a favourable declination and a decent proton luminosity results in the neutrino flux being close to intersecting with the line showing the future IceCube flux sensitivity. One could argue that the proton luminosity for this source is set relatively high when comparing the protons' contribution to the rest of the SED. However, the contribution from the gamma-gamma pairs is still comfortably below the X-ray data points. It is closer to intersecting with the 4FGL band but sits well below the gamma-ray data points from G11 too. The X-ray data from G11 show that this source has a relatively large X-ray flux, and this is what allows us to use such a large proton luminosity and get the large neutrino flux. Looking at the plot in Figure 4.10, PeV neutrinos from this blazar are expected to be detectable by IceCube-Gen2 within its first 15 years.

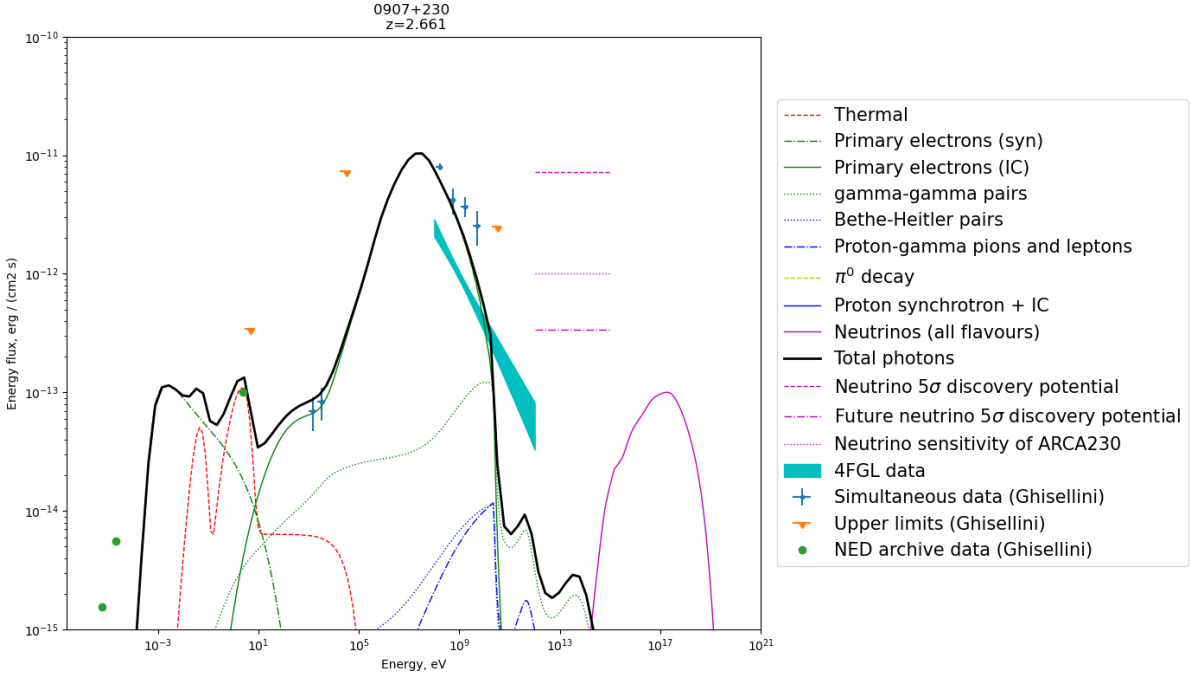

Figure 4.11: SED of blazar 0907+230 in the observer frame. See Figure 4.3 for details.

The SED of blazar 0907+230, seen in Figure 4.11, undershoots several of the data-points in the gamma-rays. Meanwhile, it overshoots the 4FGL band up until the point where Klein-Nishina effects cause suppression of the spectrum. The 4FGL band suggests a significantly lower energy flux than what was found in G11. However, the energy flux from the gamma-gamma electrons and positrons is still lower than the total energy flux implied by the 4FGL data. This in turn suggests that the estimated proton luminosity is reasonable. The declination is favourable, but the neutrino flux is not sufficiently large for the source to be detectable by IceCube-Gen2 in its first 15 years. As is the case for the other sources, the neutrino flux in the model can be increased by increasing the proton luminosity, but this is not allowed due to the low observed X-ray flux. This limits the neutrino flux so that it is not expected to be detectable, despite its favourable declination.

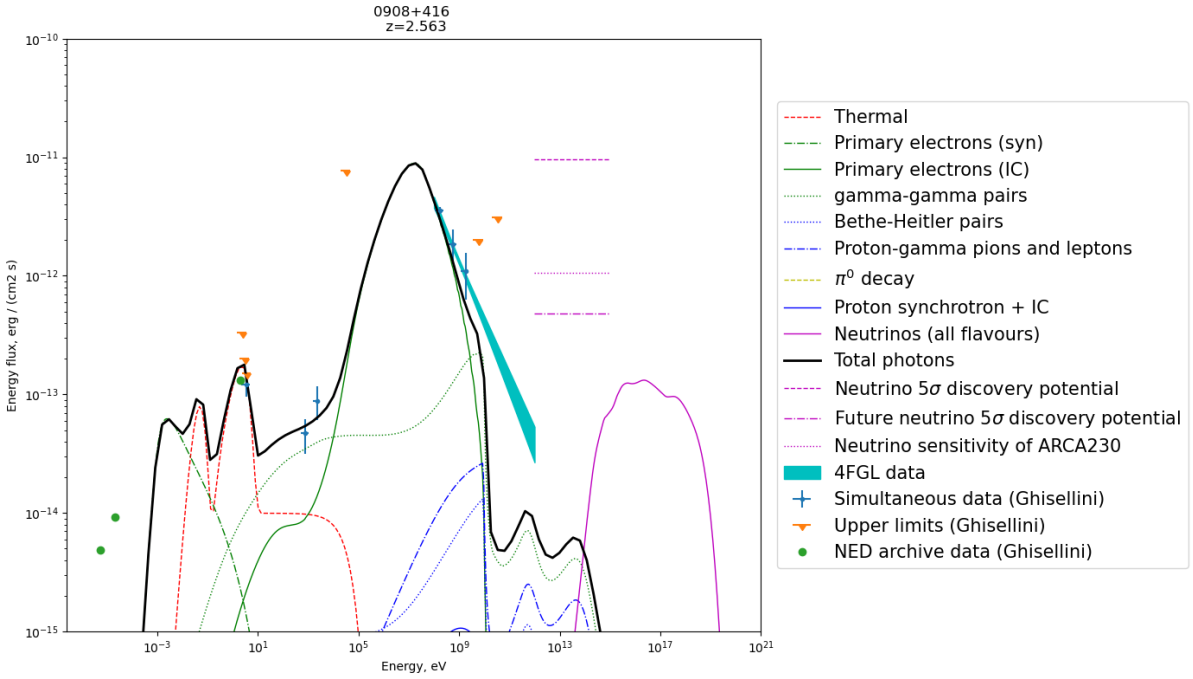

Figure 4.12: SED of blazar 0908+416 in the observer frame. See Figure 4.3 for details.

On the other hand, the SED of blazar 0908+416, seen in Figure 4.12, shows a decent fit with both the gamma-ray data from G11 and the 4FGL data. But its declination is slightly less favourable compared to blazar 0907+230, and its neutrino flux is not large enough to be detectable within the first 15 years of IceCube-Gen2. It has a baryon loading factor of $\xi = 6$, which is relatively large compared to the other sources in the sample. One could argue that the proton luminosity is set too high here when compared with the X-rays from the corona and the SSC. However, the X-rays from the gamma-gamma pairs still sit slightly below the X-ray data points from G11. The blazar does have a larger neutrino flux than 0907+230, with a significantly larger neutrino flux in energies around 1 PeV. In all, it is a more promising candidate than 0907+230, but its relatively large neutrino flux is not large enough to overcome its slightly unfavourable declination. For this source, we are pushing the limits a little with regards to how many protons we are allowed to inject, but still, it does not produce a sufficiently high neutrino flux.

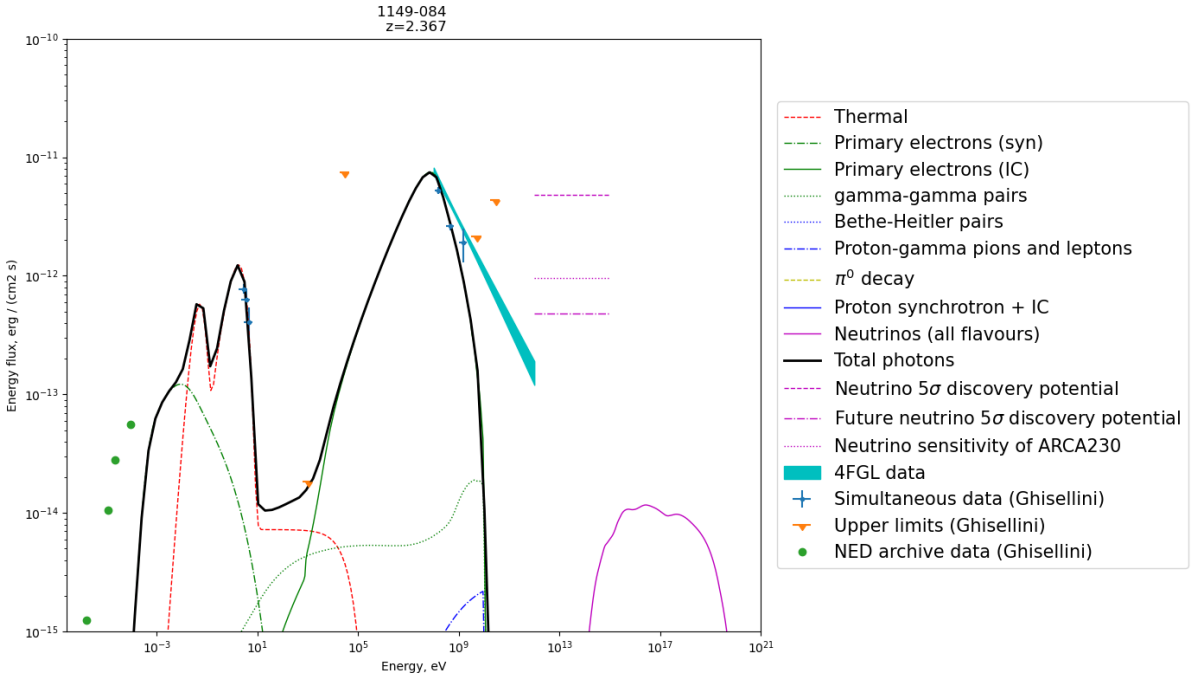

Figure 4.13: SED of blazar 1149-084 in the observer frame. See Figure 4.3 for details.

The SED of blazar 1149-084, seen in Figure 4.13, shows a decent fit with the gamma-ray data from G11. The source stands out in that it has no regular data points in the X-rays, only an upper limit in the soft X-rays. Therefore, it is grouped with the other blazars in this subsection, despite there being nothing wrong with the fit in the X-rays. It is also worth noting that unlike the other sources that have corona luminosity $L_X = 0.3L_d$, this source has $L_X = 0.03L_d$, as explained in Section 3.3.3. The declination angle is relatively small, but due to the asymmetry in flux sensitivity between the northern and southern hemispheres, its flux sensitivity is approximately equal to that of blazar 0908+416. The 4FGL data suggests some variability in its gamma-ray flux. The upper limit in the soft X-rays places a strict constraint on the proton luminosity, which is set to $L_p = 0.2L_e$. This results in a low neutrino flux, making it unlikely that it will be detectable by IceCube in the foreseeable future.

In summary, only blazar 0322+222 is expected to be detectable within the first 15 years of IceCube-Gen2. However, blazars 0242+23, 0907+230 and 0908+416 are expected to have fairly large neutrino fluxes.

4.1.3 Blazar SEDs with the worst fit of the X-ray data

The SEDs of blazars 0420+022, 0451-28, 0458-02, 0625-5438, 1343+451, 1344-1723, 1656-3302 and 2135-5006 show a less-than-optimal fit with the X-ray data from G11. These are shown in Figures 4.14, 4.15, 4.16, 4.17, 4.19, 4.20, 4.21 and 4.18 respectively.

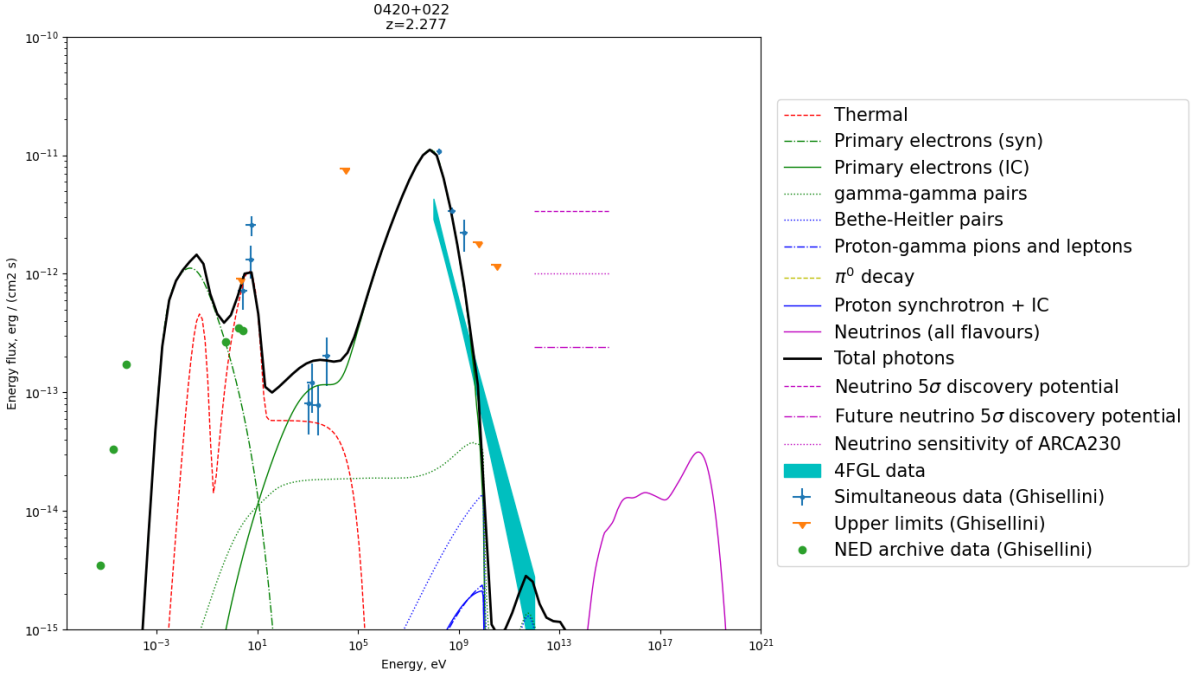

Figure 4.14: SED of blazar 0420+022 in the observer frame. See Figure 4.3 for details.

The SED of blazar 0420+022 in Figure 4.14 shows a decent fit with the gamma-ray data from G11. In the X-rays, on the other hand, a large SSC component causes significant overshooting of several of the data points. This problem can be solved by lowering the luminosity of the corona, like what was done with blazar 1149-084. But here, the corona luminosity was chosen such that the thermal spectrum is the same as in G11. This source has a very favourable declination, but due to its relatively low proton luminosity of $L_p = 0.5L_e$, the neutrino flux is much too low for it to be observable by IceCube-Gen2 in its first 15 years. The 4FGL data suggests that the average gamma-ray flux over the 14 years is slightly lower than for the 11-month survey that the data points in G11 are based on. Like with blazar 0242+23, the 4FGL data place the strictest constraints on the proton luminosity, and by extension the neutrino flux. In all, despite its favourable declination, its low neutrino luminosity makes it one of the least promising candidates in this sample.

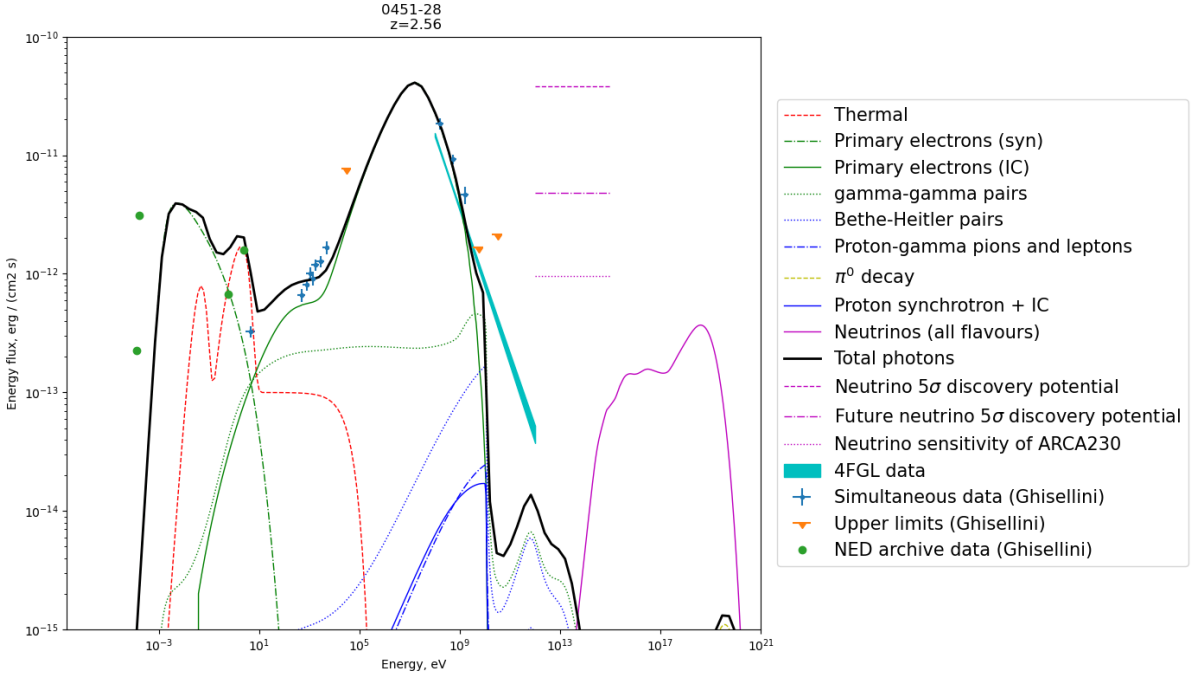

Figure 4.15: SED of blazar 0451-28 in the observer frame. See Figure 4.3 for details.

Similar to blazar 0420+022, the SED of blazar 0451-28 fits the gamma-ray data from G11 well. In addition, 0451-28 shows a better fit with the 4FGL data than 0420+022. The SED of 0451-28 is found in Figure 4.15. Its problem with fitting the X-ray data lies in the spectral index. This could motivate a change in the magnetic field or the leptonic parameters, but that is beyond the scope of this thesis. The X-ray data points suggest a relatively large X-ray flux, which in turn allows for a large proton luminosity. Relative to the electron luminosity, the proton luminosity is only $L_p = 0.5L_e$. But this source has the highest electron luminosity of the sample, with a comoving luminosity $L'_e = 2.4 \cdot 10^{44}\,\mathrm{erg\,s^{-1}}$. Therefore, the proton luminosity is still relatively large compared to the other sources in the sample. The neutrino flux seen in Figure 4.15 is decent, but not enough to make the source detectable. Its declination places the source well into the southern hemisphere, making it hard to detect. In all, blazar 0451-28 is not a favourable source of high-energy astrophysical neutrinos.

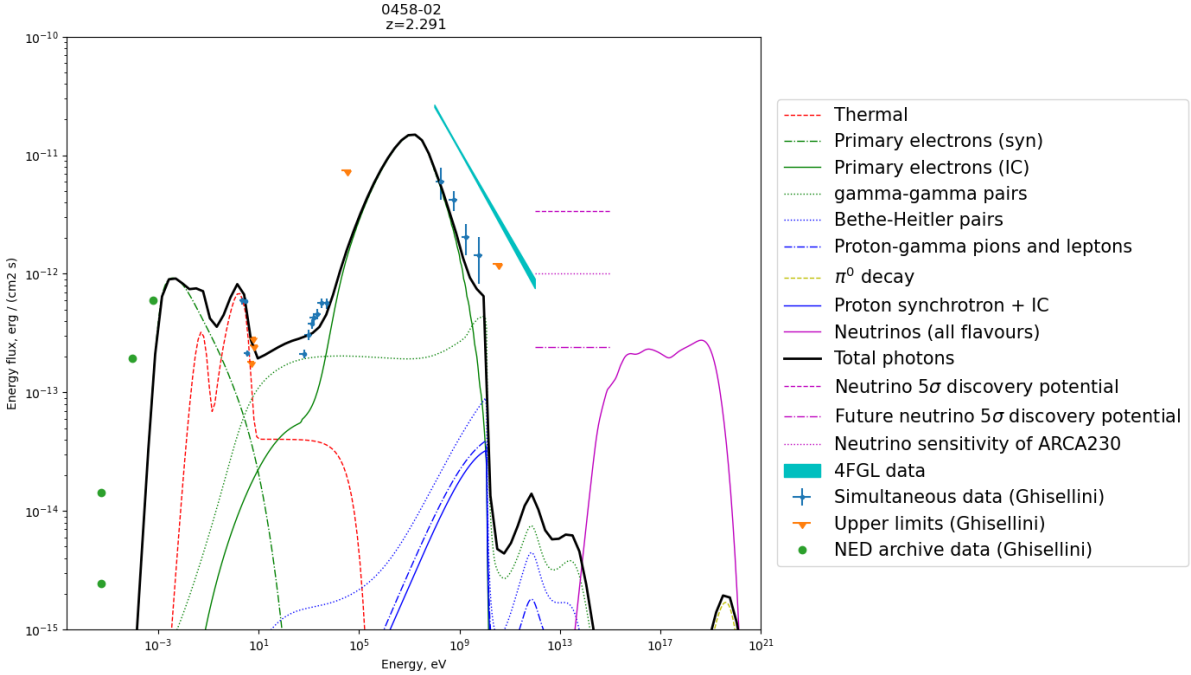

Figure 4.16: SED of blazar 0458-02 in the observer frame. See Figure 4.3 for details. The estimated future neutrino sensitivity and the neutrino flux are close to intersecting at PeV energies.

For the SED of blazar 0458-02, seen in Figure 4.16, there is a similar situation with the X-rays as with 0451-28. It also shows a decent fit with the gamma-ray data from G11, only slightly undershooting at the highest energies. The 4FGL data suggest the average gamma-ray flux is significantly larger than what was found in G11. This further suggests that this is a very powerful gamma-ray source. Additionally, its high neutrino flux and declination close to 0° makes it among the best candidates in this sample. It does show a slightly worse fit with the X-ray data than the other potential candidates, 0106+01 and 0322+222. Nonetheless, the plot does show that PeV neutrinos from this blazar may be detectable within the first 15 years of IceCube-Gen2.

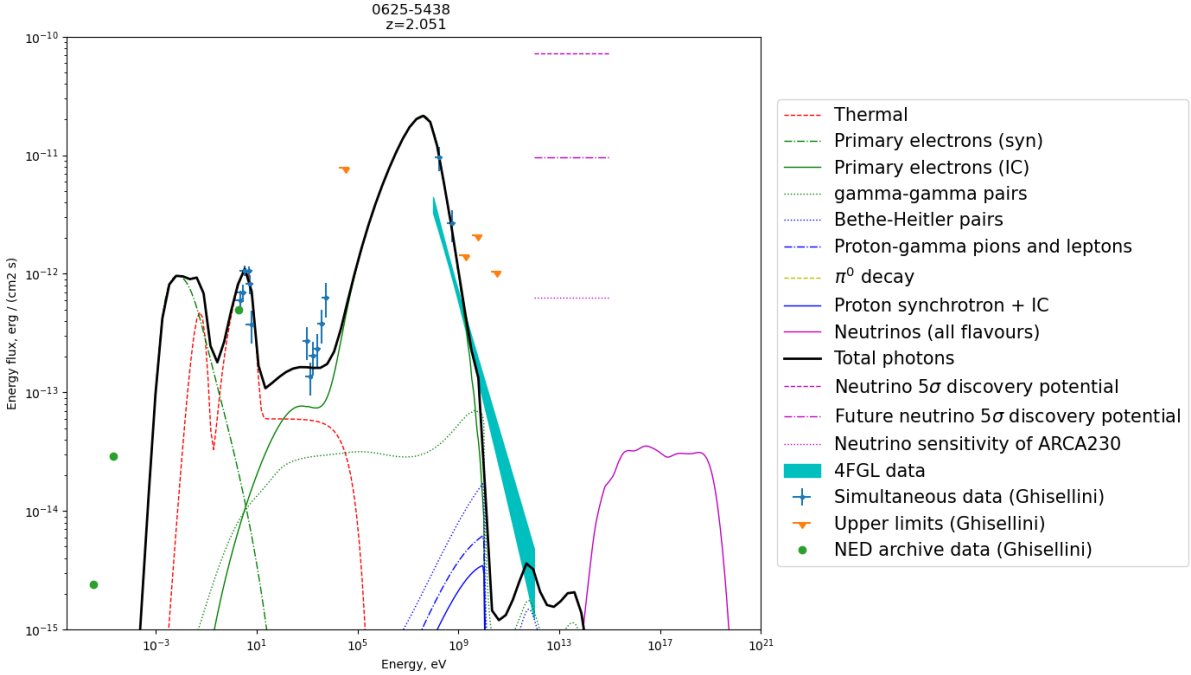

Figure 4.17: SED of blazar 0625-5438 in the observer frame. See Figure 4.3 for details.

The situation for blazar 0625-5438, on the other hand, is different. It shows a good fit with the gamma-ray data, but it has the same problems in the X-rays as 0458-02 and 0451-28, see Figure 4.17. Like with 0242+23 and 0420+022, the 4FGL data place the strictest constraints on the neutrino luminosity. The combination of a low neutrino flux and an unfavourable declination results in it not being expected to be detectable by IceCube in the foreseeable future.

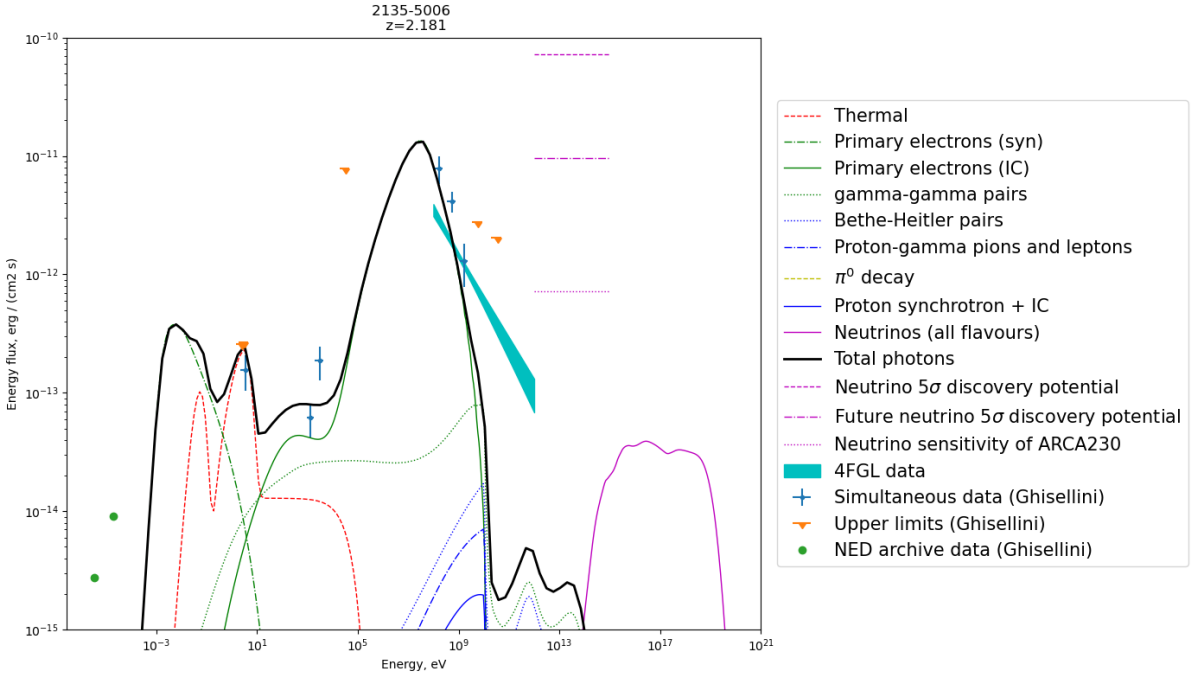

Figure 4.18: SED of blazar 2135-5006 in the observer frame. See Figure 4.3 for details.

Blazar 2135-5006's SED, seen in Figure 4.18, is in a similar situation with an unfavourable declination and a low neutrino flux. Its problem with the fit with the X-ray data is also similar. Moreover, its fit with the gamma-ray data points is decent. The 4FGL band suggests a slightly lower average flux than what was found in G11 between 100 MeV and 1 GeV. The proton luminosity cannot be set any higher without the gamma-gamma pair component starting to dominate in the X-rays. All in all, it appears to have little potential as an astrophysical neutrino source.

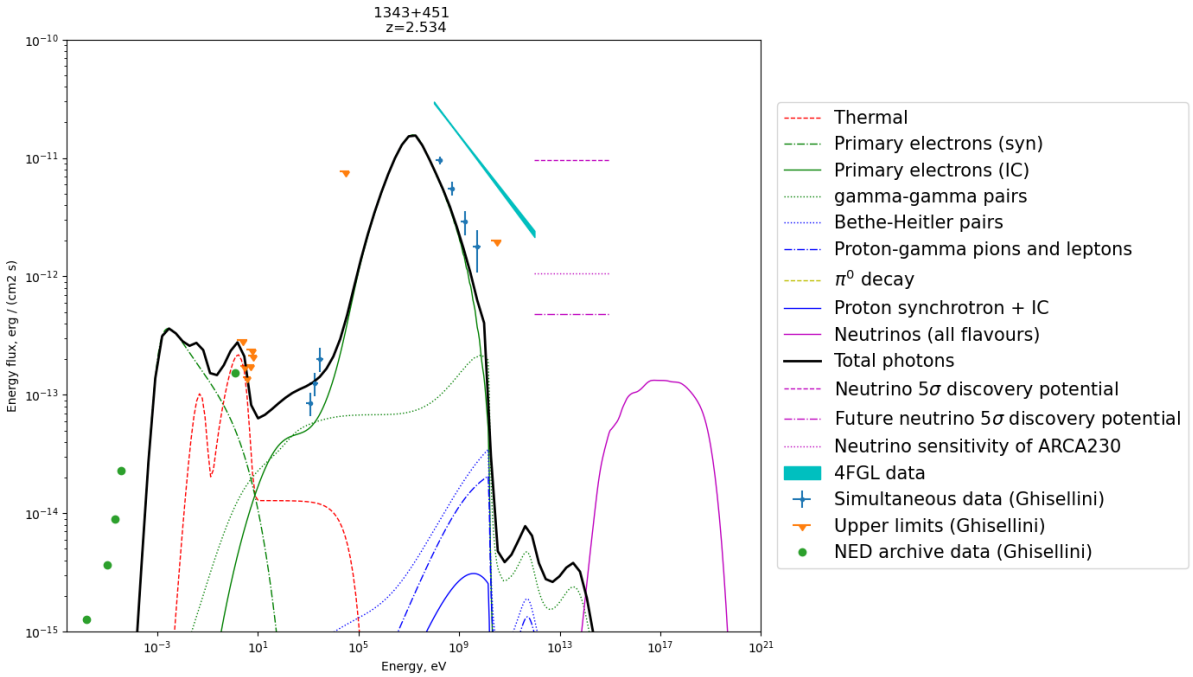

Figure 4.19: SED of blazar 1343+451 in the observer frame. See Figure 4.3 for details.

When it comes to the SED of blazar 1343+451, seen in Figure 4.19, the problem with the X-rays is the same as for 0625-5438 and others. It also undershoots all the gamma-ray data points, further motivating a change in the leptonic parameters. But as mentioned before, this is outside the scope of this thesis. The X-ray data points suggest that the X-ray flux of the source is large. Moreover, the 4FGL band shows a larger energy flux than the gamma-ray data points from G11. This suggests that the source consistently emits a large gamma-ray flux, which could allow for a large neutrino luminosity. The declination is fairly large, but given that the source is found in the northern hemisphere, the flux sensitivity of IceCube is better than for blazar 0451-28. The large X-ray and gamma-ray fluxes allow for a decent proton luminosity at $L_p = 2.2L_e$, which in turn produces a decent neutrino flux. However, the neutrino sensitivity is ultimately not large enough for it to be detectable within the first 15 years of IceCube-Gen2.

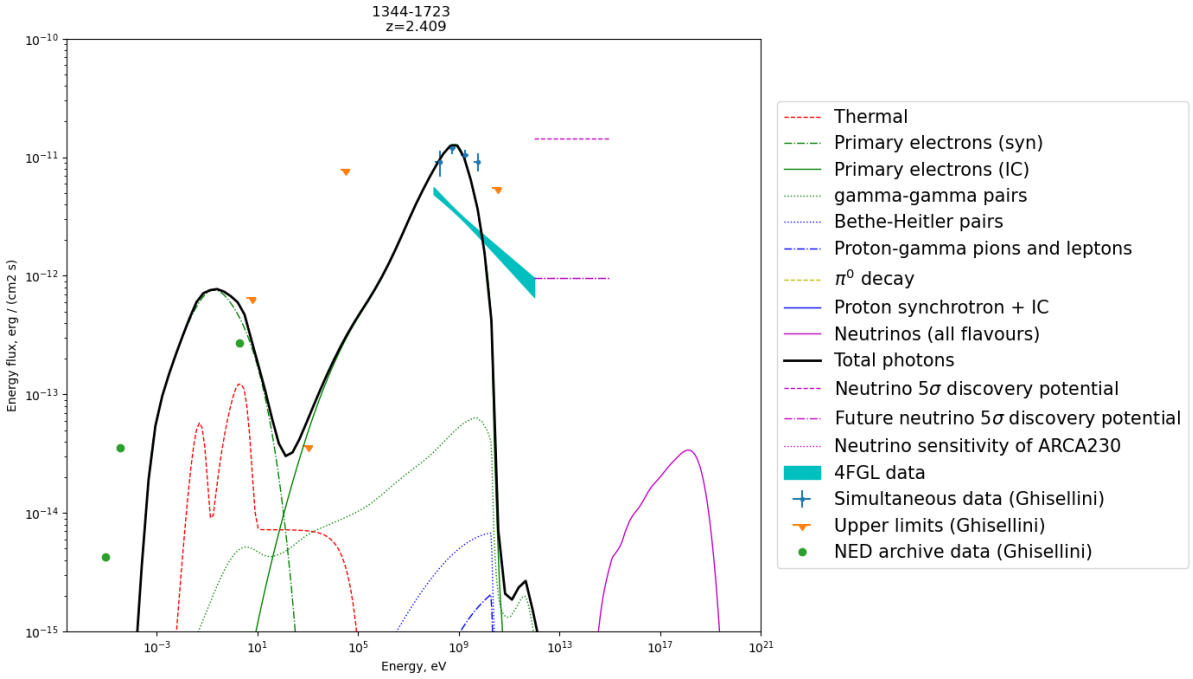

Figure 4.20: SED of blazar 1344-1723 in the observer frame. Here, the predicted neutrino sensitivities of IceCube-Gen2 and ARCA230 are overlapping. See Figure 4.3 for details.

On the other hand, the SED of blazar 1344-1723, seen in Figure 4.20, shows a better fit with the gamma-ray data points from G11 than 1343+415. The only constraint on the X-ray flux is an upper limit in the soft X-rays, which this SED overshoots. The problem is caused by a large SSC component of the energy flux. This could be solved by lowering the magnetic field strength in order to reduce the synchrotron peak. This could also give rise to a better fit with the data point in the optical. But again, this is outside the scope of the thesis. The proton luminosity is relatively low at $L_p = 0.6L_e$, and the resulting neutrino flux is not large enough to overcome the unfavourable declination. In all, it does not appear to be detectable within the first 15 years of IceCube-Gen2.

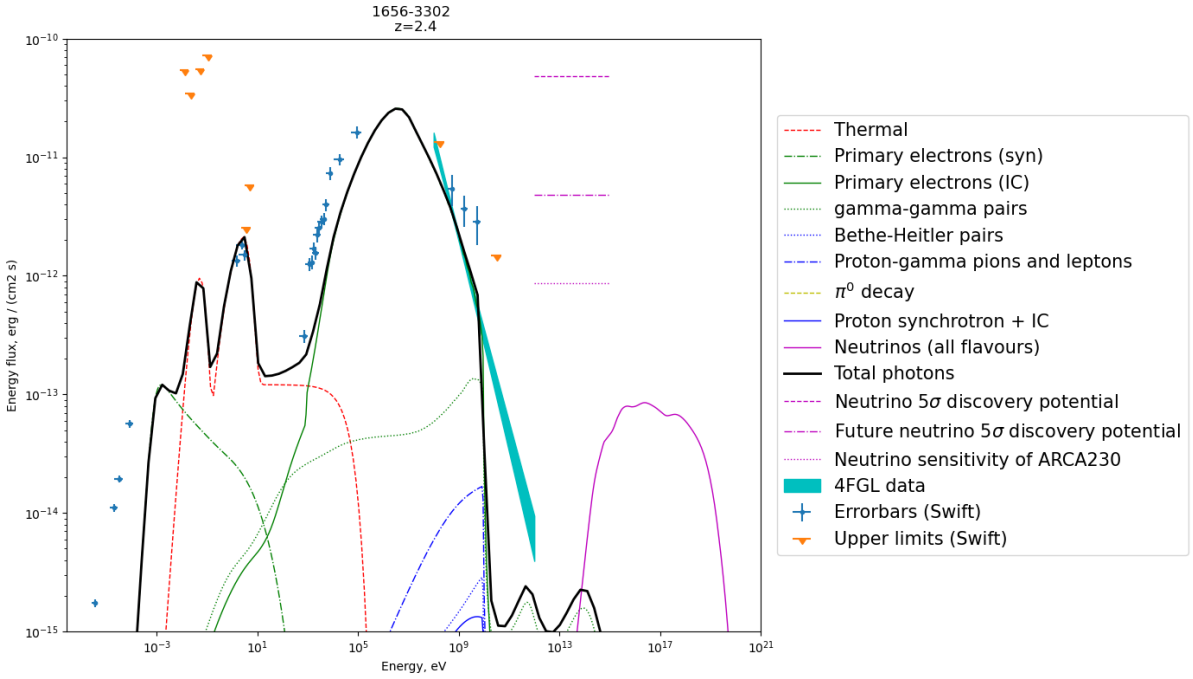

Figure 4.21: SED of blazar 1656-3302 in the observer frame. See Figure 4.3 for details.

For the SED of blazar 1656-3302, seen in Figure 4.21, there is significant undershooting of the X-ray data. To get a better fit, the spectral shape of the EC peak must be changed by changing the leptonic parameters. Again, this is outside the scope of this thesis. Additionally, the graph slightly undershoots the gamma-ray data points, but it does show a good fit with the 4FGL band. The strictest constraint on the proton luminosity comes from the 4FGL data. This leads to a relatively low baryon loading factor, shown in Table 3.4, of $\xi = 0.4$. Due to the unfavourable declination of the source, its neutrino flux is not expected to be detectable by IceCube-Gen2 in its first 15 years.

In summary, the blazar for 0458-02 is the only source among those with bad fits in the X-rays that is expected to be detectable by IceCube in the foreseeable future. The other sources are limited either by their declination, their low proton luminosity due to strict constraints on the X-ray flux or gamma-ray flux, or both. The sub-optimal fit in the X-rays suggests that the model for 0458-02 could be less accurate than that for 0106+01 and 0322+222.

4.2 Relationship between neutrino flux and photon flux

Most of the sources show a relatively flat neutrino flux centered at energy 10^{17} eV, which falls off quickly around energy 10^{19}. This observed cutoff can be explained by the maximum energy of the protons. As stated in Section 2.3.2, the neutrinos produced in pion decay carry 1/4 of the energy of its parent pion. The pions themselves carry a fraction $K_{\phi\pi}$ of the energy of the parent proton, where $K_{\phi\pi} = 0.2$ for the single-pion channel and $K_{\phi\pi} = 0.6$ for the multipion channel. The maximum Lorentz factor of the protons is around $10^9 - 10^{10}$ for all sources and is given in Table 3.3. The maximum observed

neutrino energy is then

$$E_{\nu,\,\max} = \frac{1}{4} K_{\phi\pi} \gamma_{p,\,\max} m_p c^2 \frac{\delta}{z+1} \simeq 10^{19}\,\mathrm{eV} \left(\frac{K_{\phi\pi}}{0.6}\right) \left(\frac{\gamma_{p,\,\max}}{10^{10}}\right) \left(\frac{\delta}{22}\right) \left(\frac{3}{z+1}\right), \quad (4.1)$$

where δ is the Doppler factor and z is the cosmological redshift. In general, the size of the neutrino flux follows the luminosity of the proton spectrum. As discussed in Section 4.1, it is the X-ray flux that places the strictest constraints on the proton luminosity and by extension the neutrino flux. The sizes of the neutrino flux and gamma-ray flux do not seem to be directly correlated. For example, sources 0908+416 and 1149-084 have similar gamma-ray fluxes, but the latter has a significantly lower neutrino flux. The same applies to sources 1959-4246 and 2118+188. They both have similar gamma-ray fluxes, but the latter has a lower neutrino flux. The lack of correlation is due to the gamma-ray flux being dominated by leptons. The gamma-rays emitted by the protons are subdominant. There is however a direct correlation between the observed X-ray flux and the size of the neutrino flux, but this is due to the method used to determine the proton luminosity. The proton luminosity is chosen to have the highest value without causing the total flux to overshoot the X-ray data.

In this model, there are two main sources of seed photons for the photopion process. As a result, the neutrino flux is doubly peaked, though the two peaks are not distinguishable in all of the plots. For the sources 0420+022, 0451-28 and 1537+2754, seen in Figures 4.14, 4.15 and 4.7, the two peaks of the neutrino flux are clearly distinguishable. For the Δ^+ resonance channel, the comoving energy of protons that typically interact with photons with comoving energy ϵ'_t is given by

$$\epsilon'_p \approx \frac{0.5 m_\Delta^2 c^4}{\epsilon'_t}, \quad (4.2)$$

where $m_\Delta = 1.23\,\mathrm{GeV}/c^2$ is the rest mass of the Δ baryon. To find an expression for the neutrino energy as a function of the seed photons of the photopion process, simply replace $\gamma_{p,\,\max} m_p c^2$ in Equation 4.1 with Equation 4.2 to get the following expression

$$E_\nu = \frac{1}{4} K_{\phi\pi} \frac{0.5 m_\Delta^2 c^4}{\epsilon'_t} \frac{\delta}{z+1}. \quad (4.3)$$

The photons from the BLR have energy $\epsilon'_{t,\,\mathrm{BLR}} = \Gamma \cdot 10.2\,\mathrm{eV}$ in the comoving frame of the jet. Inserting this into Equation 4.3, one finds

$$E_{\nu,\,\mathrm{BLR}} = 1.65 \cdot 10^{15}\,\mathrm{eV} \left(\frac{K_{\phi\pi}}{0.2}\right) \left(\frac{15}{\Gamma}\right) \left(\frac{10.2\,\mathrm{eV}}{\epsilon_{t,\,\mathrm{BLR}}}\right) \left(\frac{\delta}{20}\right) \left(\frac{3}{z+1}\right). \quad (4.4)$$

The IR torus has a temperature of 510 K, which means that the characteristic photon energy in the comoving frame is $\epsilon'_{t,\,\mathrm{IR}} = \Gamma k_B \cdot 510\,\mathrm{K} = \Gamma \cdot 4.39 \cdot 10^{-2}\,\mathrm{eV}$. Inserting this into Equation 4.3, one finds

$$E_{\nu,\,\mathrm{IR}} = 3.82 \cdot 10^{17}\,\mathrm{eV} \left(\frac{K_{\phi\pi}}{0.2}\right) \left(\frac{15}{\Gamma}\right) \left(\frac{4.4 \cdot 10^{-2}\,\mathrm{eV}}{\epsilon_{t,\,\mathrm{IR}}}\right) \left(\frac{\delta}{20}\right) \left(\frac{3}{z+1}\right). \quad (4.5)$$

Comparing Equations 4.4 and 4.5 with the plots, one can conclude that the first part of the neutrino flux is related to the BLR photons, while the higher energy peak is related

to the photons from the IR torus.

Name	L'_ν	L'_p	L'_e	L_d
[1]	[2]	[3]	[4]	[5]
0106+01	7.06e41	5.60e43	8.00e43	7.50e46
0157-4614	1.60e41	4.50e43	1.50e43	7.50e45
0242+23	2.70e41	3.30e43	2.20e43	6.60e46
0322+222	1.35e42	1.50e44	6.00e43	4.50e46
0420+022	6.21e40	1.00e43	2.00e43	5.25e46
0451-28	2.01e42	1.20e44	2.40e44	1.20e47
0458-02	1.64e42	1.54e44	7.00e43	3.70e46
0601-70	1.04e42	1.00e44	5.00e43	3.70e46
0625-5438	8.63e40	1.50e43	3.00e43	4.20e46
0907+230	3.13e41	1.50e44	5.00e43	8.40e45
0908+416	4.68e41	1.50e44	2.50e43	1.20e46
1149-084	3.97e40	3.00e42	1.50e43	7.20e46
1343+451	5.02e41	9.90e43	4.50e43	1.50e46
1344-1723	6.66e40	1.62e43	2.70e43	7.50e45
1537+2754	6.90e40	1.05e43	1.50e43	1.35e46
1656-3302	2.54e41	2.80e43	7.00e43	1.24e47
1959-4246	5.96e41	4.80e43	2.40e43	6.60e46
2118+188	1.09e41	1.98e43	2.20e43	1.80e46
2135-5006	1.11e41	2.87e43	2.30e43	1.05e46

Table 4.1: Total neutrino luminosity of the different sources, along with luminosities of the injected protons and electrons, and the disk luminosity. The neutrino luminosity in Column [2] is an output of the model, the rest of the columns show input parameters from Table 3.2. Col. [1]: source name; Col. [2]: luminosity of the emitted neutrinos in the comoving frame of the blob, in units of $\mathrm{erg\,s^{-1}}$; Col. [3]: luminosity of the injected protons in the comoving frame of the blob, in units of $\mathrm{erg\,s^{-1}}$; Col. [4]: luminosity of the injected electrons in the comoving frame of the blob, in units of $\mathrm{erg\,s^{-1}}$; Col. [5]: luminosity of the accretion disk in units of $\mathrm{erg\,s^{-1}}$.

Of relevance is also the neutrino luminosity, shown in Table 4.1. In Section 2.3.2, it was shown that for the single-pion channel, 5% of the proton energy is transferred to the neutrinos. Therefore, the neutrino luminosity can be at most 5% of the proton luminosity, assuming that the single-pion channel is dominant. For the multi-pion channel, 15% of the energy is transferred. Comparing Columns [2] and [3] in Table 4.1, one sees that the neutrino luminosity is around two orders of magnitude smaller than the proton luminosity, as expected.

5 Conclusion

In this thesis, it was shown that it is possible to produce SEDs that fit the data points from G11 reasonably well, using a leptohadronic model. This leptohadronic model makes predictions of the possible neutrino fluxes of the 19 blazars studied in G11. This is the first time the neutrino fluxes of these sources have been predicted using such a model. The sizes of the neutrino fluxes are directly correlated with the proton luminosity. The proton luminosity was chosen to have the maximum value it could have while the protons still provide a subdominant contribution to the X-ray and gamma-ray fluxes. Observational data in the X-rays provide the strictest constraints on the allowed proton luminosity for most of the sources, while for some the major constraint is the 4FGL data. The neutrino fluxes were compared with an estimate of the future flux sensitivity of IceCube-Gen2, following van Santen (2018).

For most of the sources, the neutrino flux was not high enough for them to be detectable within the first 15 years of IceCube-Gen2. The sources named 0106+01, 0322+222 and 0458-02 show the most potential. For the other sources, the difference between the predicted neutrino flux and the estimated flux sensitivity of IceCube-Gen2 ranges from a factor smaller than 10 for source 0242+23 to a factor larger than 10^2 for source 2135-5006. None of the sources are expected to be detectable within the first 10 years of ARCA230, with the difference between the neutrino fluxes and sensitivities ranging from a factor smaller than 10 for 0322+222 and 0601-70, to a factor around 10^2 for 1149-084. For 0106+01, 0322+222 and 0458-02, the 4FGL data suggest that these sources have a consistently large gamma-ray flux over time. In the case of blazar 0458-02, the X-ray fit is not optimal. Varying other parameters, like the magnetic field strength or the leptonic parameters, was beyond the scope of this thesis but is something one could do if one had more time. Blazar 0322+222 shows a better fit with the X-ray data than 0458-02, while 0106+01 shows an even better fit. All three show similar neutrino fluxes. Their predicted neutrino fluxes are close to intersecting the estimated IceCube-Gen2 flux sensitivity for energies larger than 1 PeV.

The conclusion is that out of the 19 blazars studied, the sources 0106+01, 0322+222 and 0458-02 may be detectable within the first 15 years of IceCube-Gen 2.

Bibliography

Aartsen, M. G. et al. (Feb. 2020). "Time-Integrated Neutrino Source Searches with 10 Years of IceCube Data". In: *Phys. Rev. Lett.* 124 (5), p. 051103. DOI: 10.1103/PhysRevLett.124.051103. URL: https://link.aps.org/doi/10.1103/PhysRevLett.124.051103.

Abdo, A. A. et al. (2010). "Fermi Large Area Telescope First Source Catalog". In: *Astrophys. J. Suppl.* 188, pp. 405–436. DOI: 10.1088/0067-0049/188/2/405. arXiv: 1002.2280 [astro-ph.HE].

Abdollahi, S. et al. (Mar. 2020). "Fermi Large Area Telescope Fourth Source Catalog". In: *The Astrophysical Journal Supplement Series* 247.1, p. 33. ISSN: 1538-4365. DOI: 10.3847/1538-4365/ab6bcb. URL: http://dx.doi.org/10.3847/1538-4365/ab6bcb.

Ahlers, Markus and Francis Halzen (2018). "Opening a New Window onto the Universe with IceCube". In: *Prog. Part. Nucl. Phys.* 102, pp. 73–88. DOI: 10.1016/j.ppnp.2018.05.001. arXiv: 1805.11112 [astro-ph.HE].

Ajello, M. et al. (Dec. 2022). "The Fourth Catalog of Active Galactic Nuclei Detected by the Fermi Large Area Telescope: Data Release 3". In: 263.2, 24, p. 24. DOI: 10.3847/1538-4365/ac9523. arXiv: 2209.12070 [astro-ph.HE].

Armitage, Philip J. (2022). *Lecture notes on accretion disk physics*. arXiv: 2201.07262 [astro-ph.HE].

Atoyan, Armen M. and Charles D. Dermer (2003). "Neutral beams from blazar jets". In: *Astrophys. J.* 586, pp. 79–96. DOI: 10.1086/346261. arXiv: astro-ph/0209231.

Ballet, J. et al. (2024). *Fermi Large Area Telescope Fourth Source Catalog Data Release 4 (4FGL-DR4)*. arXiv: 2307.12546 [astro-ph.HE].

Blandford, R. D. and R. L. Znajek (1977). "Electromagnetic extractions of energy from Kerr black holes". In: *Mon. Not. Roy. Astron. Soc.* 179, pp. 433–456. DOI: 10.1093/mnras/179.3.433.

Burtscher, Leonard et al. (2013). "A diversity of dusty AGN tori: Data release for the VLTI/MIDI AGN Large Program and first results for 23 galaxies". In: *Astron. Astrophys.* 558, A149. DOI: 10.1051/0004-6361/201321890. arXiv: 1307.2068 [astro-ph.CO].

Cerruti, M et al. (Nov. 2018). "Leptohadronic single-zone models for the electromagnetic and neutrino emission of TXS 0506+056". In: *Monthly Notices of the Royal Astronomical Society: Letters* 483.1, pp. L12–L16. ISSN: 1745-3925. DOI: 10.1093/mnrasl/sly210. eprint: https://academic.oup.com/mnrasl/article-pdf/483/1/L12/56977132/mnrasl_483_1_l12.pdf. URL: https://doi.org/10.1093/mnrasl/sly210.

Cerruti, M. et al. (Feb. 2015). "A hadronic origin for ultra-high-frequency-peaked BL Lac objects". In: *Monthly Notices of the Royal Astronomical Society* 448.1, pp. 910–927. ISSN: 0035-8711. DOI: 10.1093/mnras/stu2691. eprint: https://academic.oup.com/mnras/article-pdf/448/1/910/9379400/stu2691.pdf. URL: https://doi.org/10.1093/mnras/stu2691.

Cerruti, Matteo (2020). "Leptonic and Hadronic Radiative Processes in Supermassive-Black-Hole Jets". In: *Galaxies* 8.4, p. 72. DOI: 10.3390/galaxies8040072. arXiv: 2012.13302 [astro-ph.HE].

Dermer, Charles D. and Govind Menon (Oct. 2009). *High Energy Radiation from Black Holes: Gamma Rays, Cosmic Rays, and Neutrinos*. Princeton University Press. ISBN: 978-0-691-14408-5.

Dermer, Charles D. et al. (2009). "Gamma-Ray Studies of Blazars: Synchro-Compton Analysis of Flat Spectrum Radio Quasars". In: *Astrophys. J.* 692. [Erratum: Astrophys.J. 747, 83 (2012)], pp. 32–46. DOI: 10.1088/0004-637X/692/1/32. arXiv: 0808.3185 [astro-ph].

Einstein, Albert (1915). "Zur Allgemeinen Relativitätstheorie". In: *Sitzungsber. Preuss. Akad. Wiss. Berlin (Math. Phys.)* 1915. [Addendum: Sitzungsber.Preuss.Akad.Wiss.Berlin (Math.Phys.) 1915, 799–801 (1915)], pp. 778–786.

Finke, Justin D., Charles D. Dermer, and Markus Böttcher (Oct. 2008). "Synchrotron Self-Compton Analysis of TeV X-Ray-Selected BL Lacertae Objects". In: *The Astrophysical Journal* 686.1, pp. 181–194. ISSN: 1538-4357. DOI: 10.1086/590900. URL: http://dx.doi.org/10.1086/590900.

Gao, Shan et al. (Nov. 2018). "Modelling the coincident observation of a high-energy neutrino and a bright blazar flare". In: *Nature Astronomy* 3.1, pp. 88–92. ISSN: 2397-3366. DOI: 10.1038/s41550-018-0610-1. URL: http://dx.doi.org/10.1038/s41550-018-0610-1.

Ghisellini, G. (2013). *Radiative Processes in High Energy Astrophysics*. Springer International Publishing. ISBN: 9783319006123. DOI: 10.1007/978-3-319-00612-3. URL: http://dx.doi.org/10.1007/978-3-319-00612-3.

Ghisellini, G. and F. Tavecchio (July 2009). "Canonical high-power blazars". In: *Monthly Notices of the Royal Astronomical Society* 397.2, pp. 985–1002. ISSN: 0035-8711. DOI: 10.1111/j.1365-2966.2009.15007.x. eprint: https://academic.oup.com/mnras/article-pdf/397/2/985/2943748/mnras0397-0985.pdf. URL: https://doi.org/10.1111/j.1365-2966.2009.15007.x.

Ghisellini, G. et al. (Feb. 2011). "High-redshift Fermi blazars". In: 411.2, pp. 901–914. DOI: 10.1111/j.1365-2966.2010.17723.x. arXiv: 1009.3275 [astro-ph.CO].

Gilmore, Rudy C. et al. (2009). "Modeling gamma-ray attenuation in high redshift GeV spectra". English (US). In: *AIP Conference Proceedings* 1085. 4th International Meeting on High Energy Gamma-Ray Astronomy ; Conference date: 07-07-2008 Through 11-07-2008, pp. 577–580. ISSN: 0094-243X. DOI: 10.1063/1.3076738.

Hemmer, Per Christian (2005). *Kvantemekanikk*. Fagbokforlaget. ISBN: 9788251920285.

Jauch, J. M. and F. Rohrlich (1976). *The theory of photons and electrons. The relativistic quantum field theory of charged particles with spin one-half*. 2nd ed. Texts and Monographs in Physics. Berlin: Springer. ISBN: 978-3-642-80951-4. DOI: 10.1007/978-3-642-80951-4.

Keivani, A. et al. (Sept. 2018). "A Multimessenger Picture of the Flaring Blazar TXS 0506+056: Implications for High-energy Neutrino Emission and Cosmic-Ray Acceleration". In: 864.1, 84, p. 84. DOI: 10.3847/1538-4357/aad59a. arXiv: 1807.04537 [astro-ph.HE].

Kelner, S. R. and F. A. Aharonian (Aug. 2008). "Energy spectra of gamma rays, electrons, and neutrinos produced at interactions of relativistic protons with low energy radiation". In: *Physical Review D* 78.3. ISSN: 1550-2368. DOI: 10.1103/physrevd.78.034013. URL: http://dx.doi.org/10.1103/PhysRevD.78.034013.

Kerr, Roy P. (Sept. 1963). "Gravitational Field of a Spinning Mass as an Example of Algebraically Special Metrics". In: 11.5, pp. 237–238. DOI: 10.1103/PhysRevLett.11.237.

Klinger, Marc et al. (2023). *AM^3: An Open-Source Tool for Time-Dependent Lepto-Hadronic Modeling of Astrophysical Sources*. arXiv: 2312.13371 [astro-ph.HE].

Lynden-Bell, D. (Aug. 1969). "Galactic Nuclei as Collapsed Old Quasars". In: 223.5207, pp. 690–694. DOI: 10.1038/223690a0.

Mannheim, K. (1993). "Gamma-rays and neutrinos from a powerful cosmic accelerator". In: *Phys. Rev. D* 48, pp. 2408–2414. DOI: 10.1103/PhysRevD.48.2408. arXiv: astro-ph/9306005.

Mucke, A. et al. (2000). "SOPHIA: Monte Carlo simulations of photohadronic processes in astrophysics". In: *Comput. Phys. Commun.* 124, pp. 290–314. DOI: 10.1016/S0010-4655(99)00446-4. arXiv: astro-ph/9903478.

Muller, Rasa, Aart Heijboer, and Thijs van Eeden (2023). "Search for cosmic neutrino point sources and extended sources with 6-21 lines of KM3NeT/ARCA". In: *PoS* ICRC2023, p. 1018. DOI: 10.22323/1.444.1018.

Murase, Kohta, Foteini Oikonomou, and Maria Petropoulou (Sept. 2018). "Blazar Flares as an Origin of High-energy Cosmic Neutrinos?" In: *The Astrophysical Journal* 865.2, p. 124. ISSN: 1538-4357. DOI: 10.3847/1538-4357/aada00. URL: http://dx.doi.org/10.3847/1538-4357/aada00.

Nellen, Lukas, Karl Mannheim, and Peter L. Biermann (1993). "Neutrino production through hadronic cascades in AGN accretion disks". In: *Phys. Rev. D* 47, pp. 5270–5274. DOI: 10.1103/PhysRevD.47.5270. arXiv: hep-ph/9211257.

Oikonomou, Foteini et al. (2019). "High energy neutrino flux from individual blazar flares". In: *Mon. Not. Roy. Astron. Soc.* 489.3, pp. 4347–4366. DOI: 10.1093/mnras/stz2246. arXiv: 1906.05302 [astro-ph.HE].

Padovani, P. et al. (Aug. 2017). "Active galactic nuclei: what's in a name?" In: *The Astronomy and Astrophysics Review* 25.1. ISSN: 1432-0754. DOI: 10.1007/s00159-017-0102-9. URL: http://dx.doi.org/10.1007/s00159-017-0102-9.

Petropoulou, M. and A. Mastichiadis (Dec. 2014). "Bethe–Heitler emission in BL Lacs: filling the gap between X-rays and γ-rays". In: *Monthly Notices of the Royal Astronomical Society* 447.1, pp. 36–48. ISSN: 0035-8711. DOI: 10.1093/mnras/stu2364. URL: http://dx.doi.org/10.1093/mnras/stu2364.

Resconi, Elisa et al. (2017). "Connecting blazars with ultrahigh-energy cosmic rays and astrophysical neutrinos". In: *Mon. Not. Roy. Astron. Soc.* 468.1, pp. 597–606. DOI: 10.1093/mnras/stx498. arXiv: 1611.06022 [astro-ph.HE].

Righi, C, F Tavecchio, and S Inoue (Dec. 2018). "Neutrino emission from BL Lac objects: the role of radiatively inefficient accretion flows". In: *Monthly Notices of the Royal Astronomical Society: Letters* 483.1, pp. L127–L131. ISSN: 1745-3933. DOI: 10.1093/mnrasl/sly231. URL: http://dx.doi.org/10.1093/mnrasl/sly231.

Rodrigues, Xavier et al. (2023). *Leptohadronic Multimessenger Modeling of 324 Gamma-Ray Blazars*. arXiv: 2307.13024 [astro-ph.HE].

Salpeter, E. E. (Aug. 1964). "Accretion of Interstellar Matter by Massive Objects." In: 140, pp. 796–800. DOI: 10.1086/147973.

Schmidt, M. (Mar. 1963). "3C 273 : A Star-Like Object with Large Red-Shift". In: 197.4872, p. 1040. DOI: 10.1038/1971040a0.

Schwarzschild, Karl (1916). "On the gravitational field of a mass point according to Einstein's theory". In: *Sitzungsber. Preuss. Akad. Wiss. Berlin (Math. Phys.)* 1916, pp. 189–196. arXiv: physics/9905030.

Shakura, N. I. and R. A. Sunyaev (June 1976). "A theory of the instability of disk accretion on to black holes and the variability of binary X-ray sources, galactic nuclei and quasars." In: 175, pp. 613–632. DOI: 10.1093/mnras/175.3.613.

Tavecchio, F. and G. Ghisellini (2008). "The spectrum of the Broad Line Region and the high-energy emission of powerful blazars". In: *Mon. Not. Roy. Astron. Soc.* 386, p. 945. DOI: 10.1111/j.1365-2966.2008.13072.x. arXiv: 0802.0871 [astro-ph].

— (2015). "High-energy cosmic neutrinos from spine-sheath BL Lac jets". In: *Mon. Not. Roy. Astron. Soc.* 451.2, pp. 1502–1510. DOI: 10.1093/mnras/stv1023. arXiv: 1411.2783 [astro-ph.HE].

Tavecchio, Maraschi, and Ghisellini (1998). "Constraints on the physical parameters of TeV blazars". In: *Astrophys. J.* 509, p. 608. DOI: 10.1086/306526. arXiv: astro-ph/9809051.

Troitsky, Sergey V. (2021). "Constraints on models of the origin of high-energy astrophysical neutrinos". In: *Usp. Fiz. Nauk* 191.12, pp. 1333–1360. DOI: 10.3367/UFNe.2021.09.039062. arXiv: 2112.09611 [astro-ph.HE].

Urry, C. Megan and P. Padovani (1995). "Unified schemes for radio-loud active galactic nuclei". In: *Publ. Astron. Soc. Pac.* 107, p. 803. DOI: 10.1086/133630. arXiv: astro-ph/9506063.

van Santen, Jakob (2018). "IceCube-Gen2: the next-generation neutrino observatory for the South Pole". In: *PoS* ICRC2017, p. 991. DOI: 10.22323/1.301.0991.

Vanden Berk, Daniel E. et al. (2001). "Composite Quasar Spectra from the Sloan Digital Sky Survey". In: *Astron. J.* 122, pp. 549–564. DOI: 10.1086/321167. arXiv: astro-ph/0105231.

Zech, A., M. Cerruti, and D. Mazin (May 2017). "Expected signatures from hadronic emission processes in the TeV spectra of BL Lacertae objects". In: *Astronomy amp; Astrophysics* 602, A25. ISSN: 1432-0746. DOI: 10.1051/0004-6361/201629997. URL: http://dx.doi.org/10.1051/0004-6361/201629997.

Zhang, B. Theodore et al. (Jan. 2020). "A Neutral Beam Model for High-energy Neutrino Emission from the Blazar TXS 0506+056". In: *The Astrophysical Journal* 889.2, p. 118. DOI: 10.3847/1538-4357/ab659a. URL: https://dx.doi.org/10.3847/1538-4357/ab659a.

A Cooled electron spectra

Plots for all of the sources showing the injected electron spectra along with the electron spectra after the simulation has run for a time $t = 3 \cdot t_{\text{cross}} = 3 \cdot R_b/c$ are found in Figures A.1, A.2, A.3, A.4 and A.5.

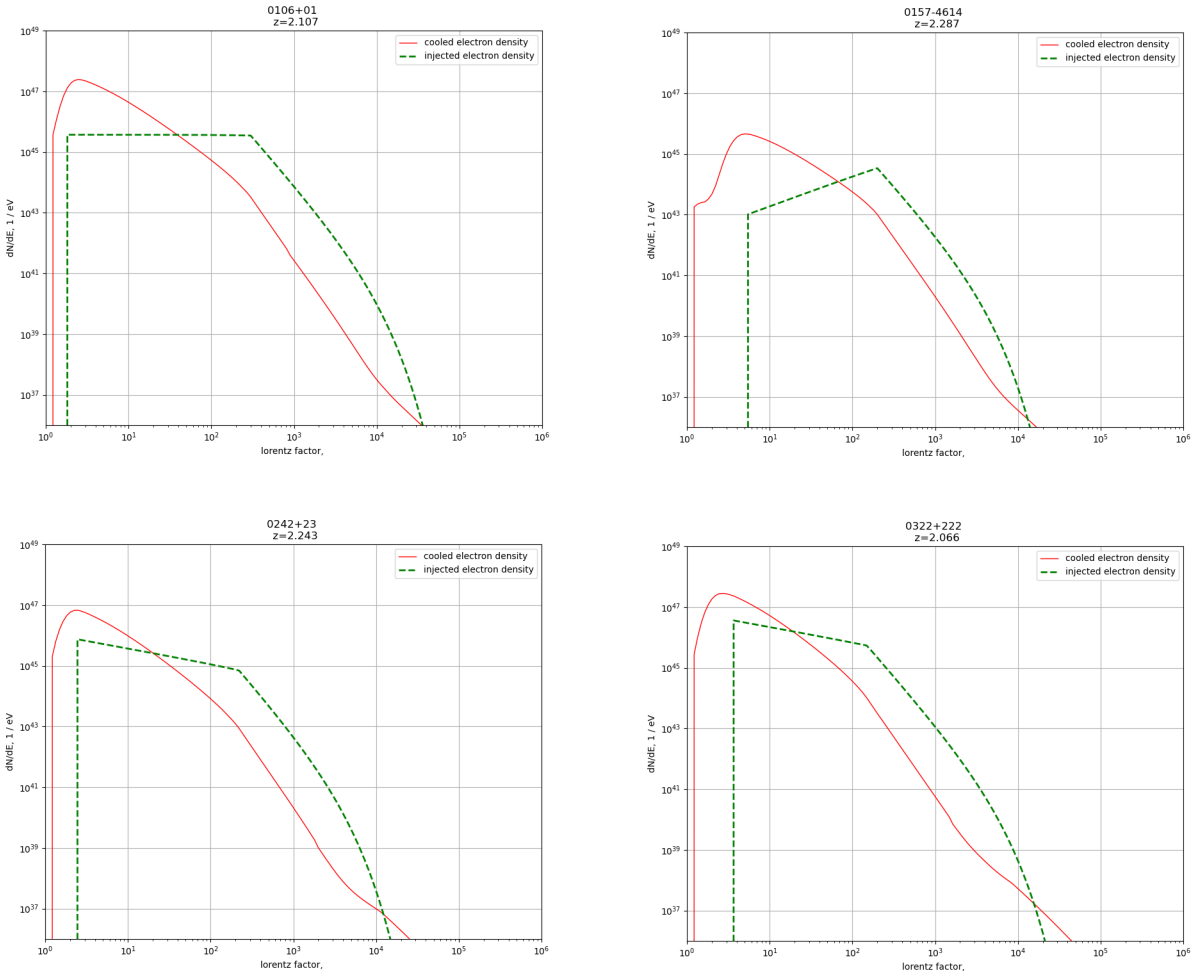

Figure A.1: Electron spectra for blazars 0106+01, 0157-4614, 0242+23 and 0322+222. Injected spectrum and electron spectrum after three light crossing times as a function of Lorentz factor.

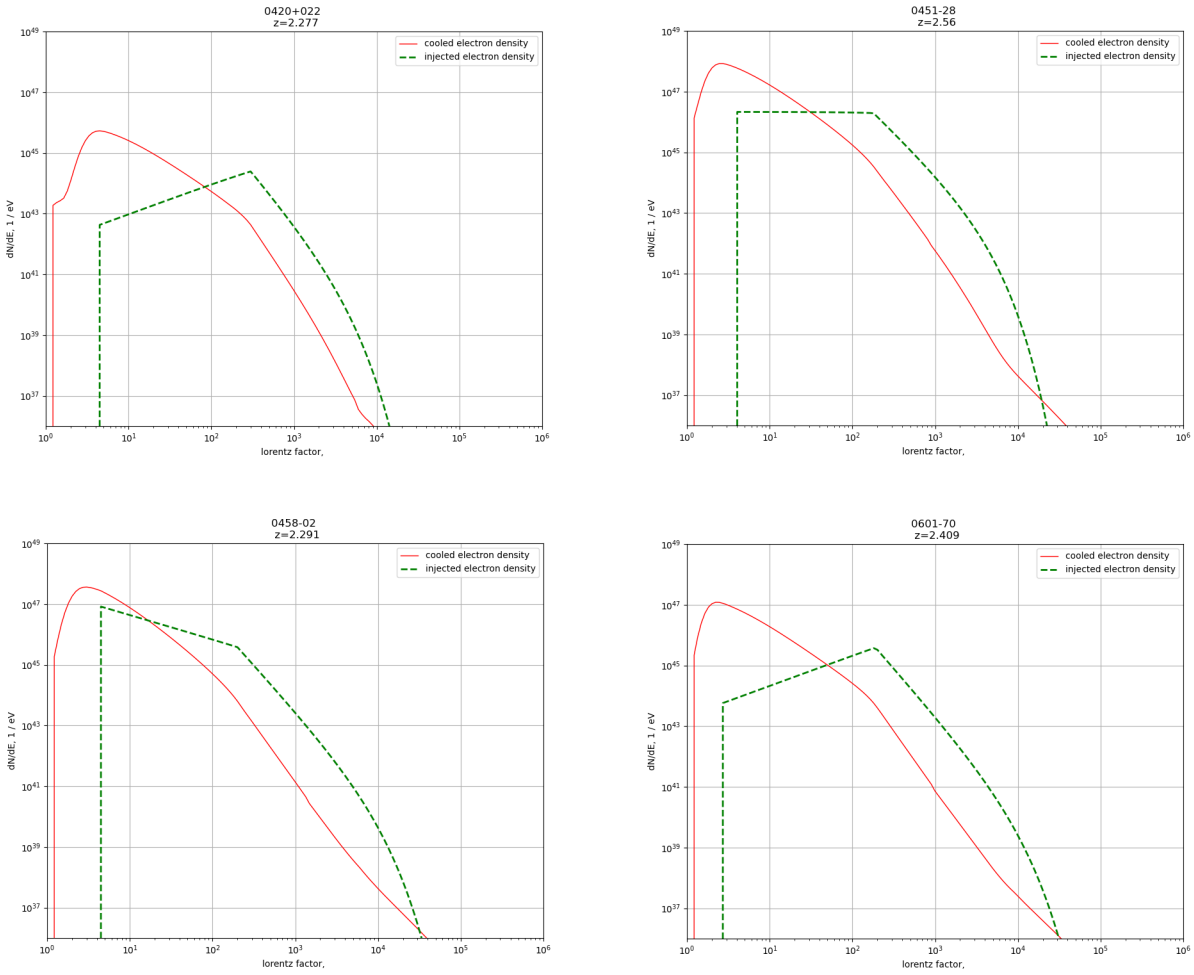

Figure A.2: Electron spectra for blazars 0420+022, 0451-28, 0458-02 and 0601-70. See Figure A.1 for details.

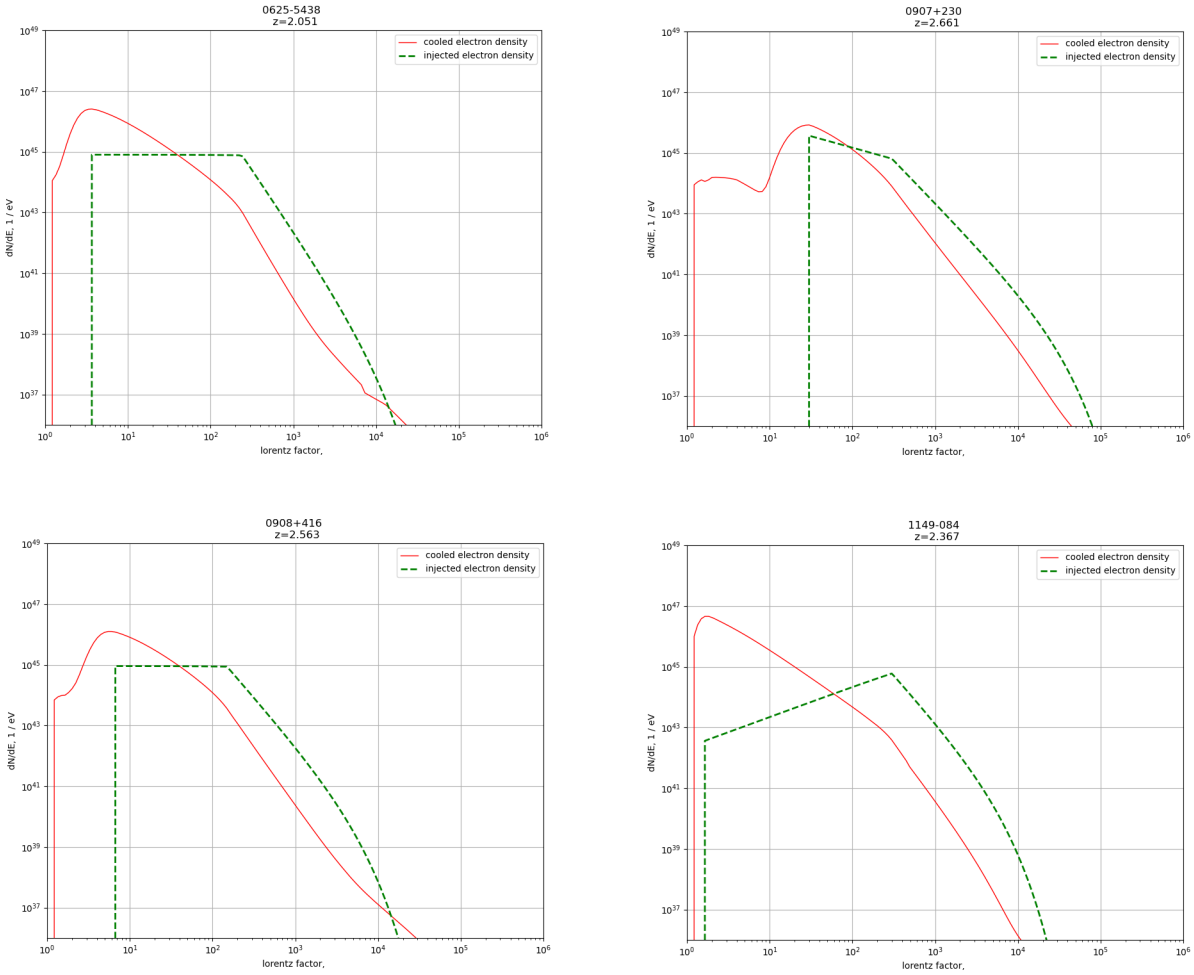

Figure A.3: Electron spectra for blazars 0625-5438, 0907+230, 0908+416 and 1149-084. See Figure A.1 for details.

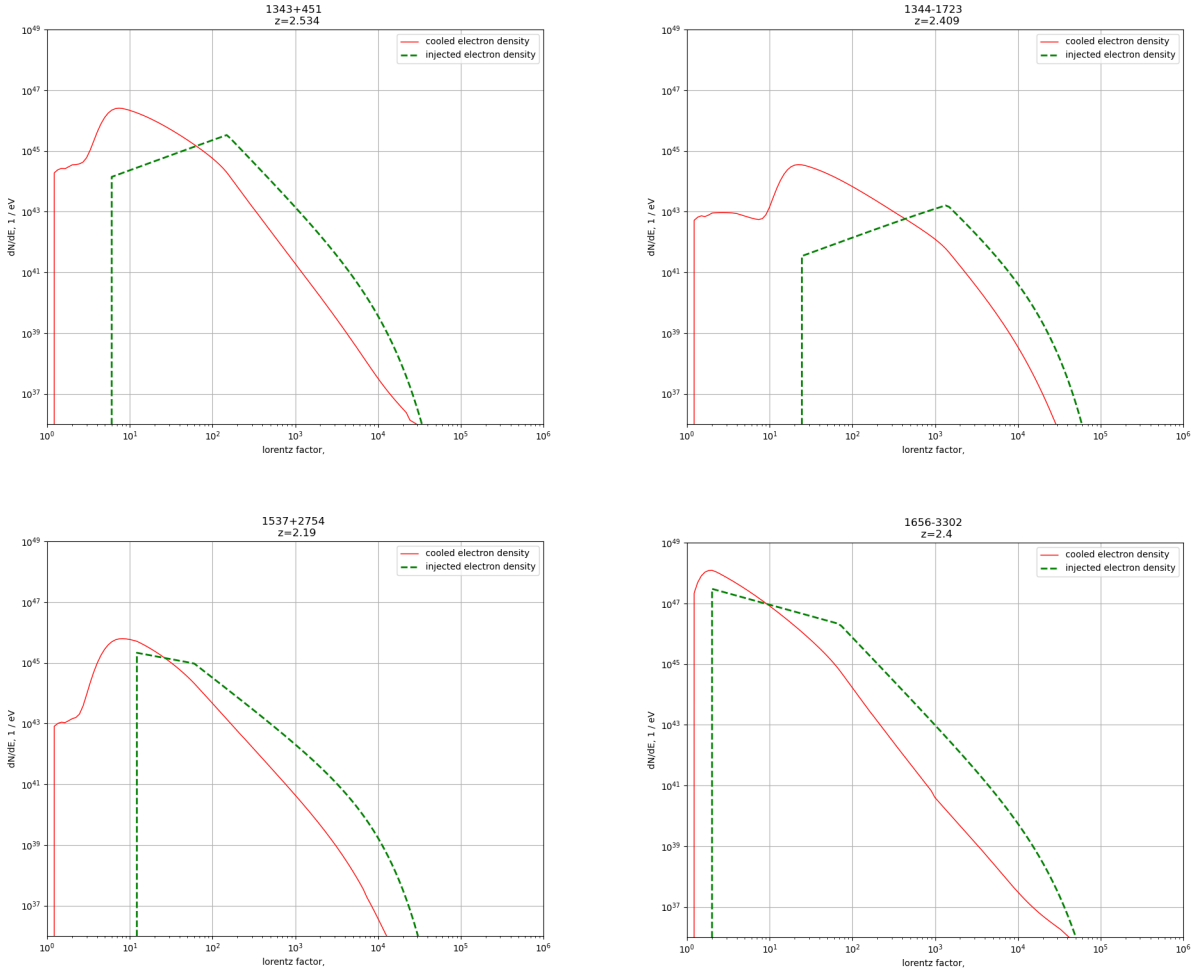

Figure A.4: Electron spectra for blazars 1343+451, 1344-1723, 1537+2754 and 1656-3302. See Figure A.1 for details.

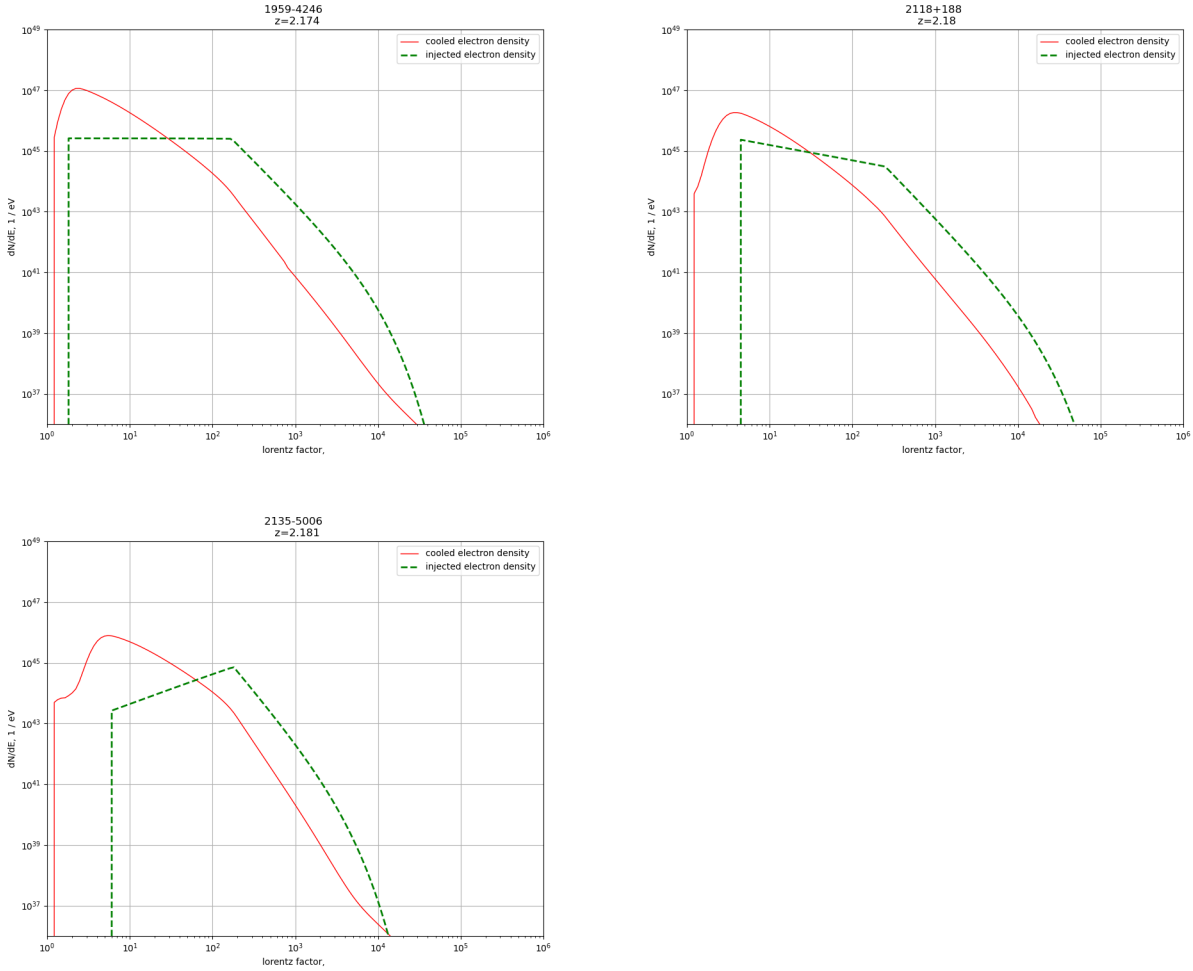

Figure A.5: Electron spectra for blazars 1959-4246, 2118+188 and 2135-5006. See Figure A.1 for details.

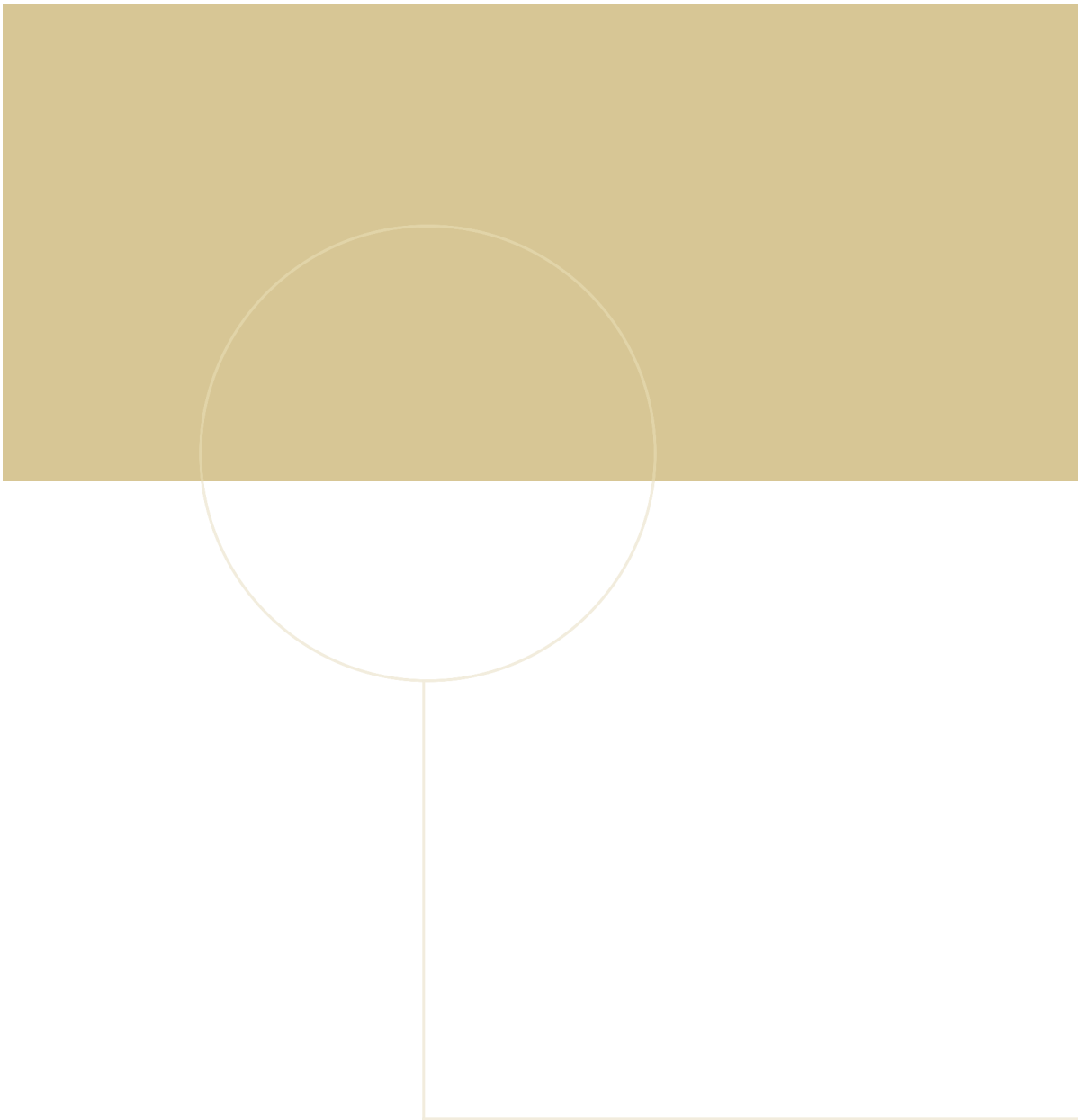

NTNU

Norwegian University of
Science and Technology